UNIVERSITÀ DEGLI STUDI DI NAPOLI FEDERICO II

Department of Structures for Engineering and Architecture

PH.D. PROGRAM IN

STRUCTURAL, GEOTECHNICAL ENGINEERING AND SEISMIC RISK

COORDINATOR : PROF. LUCIANO ROSATI

XXXI CYCLE

MARIANO SUPINO

PH.D. THESIS

A PROBABILISTIC APPROACH FOR THE ESTIMATION OF EARTHQUAKE SOURCE PARAMETERS FROM SPECTRAL INVERSION

TUTOR : PROF. GAETANO FESTA

A probabilistic approach for the estimation of earthquake source parameters from spectral inversion

A Nando.

A chi ricerca

Dici :
per noi va male.
Il buio cresce.
Le forze scemano.
Dopo che si è lavorato tanti anni
noi siamo ora
in una condizione più difficile
di quando si era appena cominciato.

E il nemico ci sta innanzi
più potente che mai.
Sembra gli siano cresciute le forze.
Ha preso una apparenza invincibile.
E noi abbiamo commesso degli errori,
non si può negarlo.
Siamo sempre di meno.
Le nostre parole sono confuse.
Una parte delle nostre parole
le ha stravolte il nemico fino a renderle
irriconoscibili.

Che cosa è errato ora, falso, di quel che abbiamo detto ?
Qualcosa, tutto ?
Su chi contiamo ancora ?
Siamo dei sopravvissuti,
respinti via dalla corrente ?
Resteremo indietro, senza
comprendere più nessuno
e da nessuno compresi ?

O dobbiamo contare
sulla buona sorte?

Questo tu chiedi. Non aspettarti
nessuna risposta
oltre la tua.

Bertolt Brecht | *A chi esita*

Table of contents

Abstract

The characterization of the mechanisms of earthquake generation and propagation is a major challenge in understanding the Earth engine. Although the seismic rupture non-linearly combines several space and time scales, some macroscopic parameters can provide insights in its evolution, such as the earthquake size and the stress drop released during a seismic event. However, the estimation of these parameters is very uncertain (Cotton et al., 2013), owing to uncertainties in data and models and to the strong coupling between source effects and wave propagation up to the observation sites.

The objective of this thesis is the characterization of the seismic source parameters using the amplitude spectrum of the displacement records and assuming that the earthquake behaves as a circular crack (Keilis-Borok, 1959). Several methods for the characterization of the source using a spectral analysis have been proposed in literature. Systematic comparison between different methodologies highlighted the dependence of the results on the fitting model, due to the high correlation between the parameters, especially comparing EGF and TGF based techniques (Ide et al. 2003; Oye et al., 2005). A probabilistic approach can allow to investigate such a correlation, defining a probability density function (PDF) in the parameter space and allowing for a consistent estimate of the uncertainties. Using the probabilistic framework developed by Tarantola (2005), and specifically the notion of conjunction of states of information, I developed a probabilistic approach to retrieve the source parameters seismic moment (through the low-frequency spectral level), the corner frequency (that is a proxy of the rupture length) and the high-frequency decay parameter. Information on the source of an earthquake requires the modeling of the wave propagation too; I choose to use in this

work a theoretical Green's function, adding one parameter to invert related to the propagation (a frequency-independent Q-factor) beyond the three source parameter that I want to retrieve.

I model the observations with an operator, defined on these four parameters, which is non-linear; thus, a global exploration of the model space is required in order to find the best solution to describe the data.

Additionally, the joint a-posteriori probability density function (PDF) is computed around the best model, to extract the correlation matrix of the parameters. This allows to obtain estimates and uncertainties from the PDF, that are taking into account the correlations.

The global exploration relies on the building of a Markov chain in the parameter space and on the combination of a deterministic minimization with a random exploration of the space (Basin-Hopping method, Wales and Doye, 1997; Wales, 2003).

The main advantages of this new methodology are the following :

- A fully probabilistic approach associated with a global exploration method can provide a robust information about the "best-fit" model, with correct estimation of uncertainties and parameter correlation.
- The shape of the estimated PDF can assess the quality of the solutions, allowing to rule out noisy data and thus enabling the use of the method for automatic processing of large datasets.

I performed three applications of the method. In Chapter 4, I analyzed the Central Italy 2016-2017 sequence, characterizing the source of all the earthquakes with magnitude $M_L \geq 4.0$ (56 events); in Chapter 5 I characterized the source of more than 10000 LFEs occurred in the Nankai region (Japan) during the period 2012-2016; in Chapter 6 I analyzed the micro-seismicity ($M_j = 0.0 - 4.5$, 1061 events) occurred from 2016 to 2017 in the Northern Ibaraki region (Japan).

1. Introduction

1.1. Preamble

The characterization of the mechanisms of earthquake generation and propagation is a major challenge in understanding the Earth engine. On the one hand it allows to shine a light on the physics of the faulting process over different space and time scales, on the other hand it has a strong societal impact, mitigating the seismic risk over short to medium time scales (days to years). The major issue in understanding the physics of earthquake rupture is the correct characterization of the energy budget associated with different mechanisms which take place during the earthquake nucleation, unstable propagation, short wavelength radiation and arrest. Although the seismic rupture non-linearly combines several space and time scales, some macroscopic parameters can provide insights in its evolution, such as the earthquake size and the stress drop released during a seismic event. However, the estimation of these parameters is very uncertain (Cotton et al., 2013), owing to uncertainties in data and models and to the strong coupling between source effects and wave propagation up to the observation sites. Indeed, actual estimates of stress drop do not allow to distinguish if this parameter is universal or it scales with the earthquake size (e.g. Sholtz 1994, Shaw 2009, Cocco et al. 2016).

Different kinematic and dynamic source models have been proposed to infer the stress drop from observations, such as a circular rupture (Brune, 1970; Sato and Hirasawa, 1973; Madariaga, 1976) or a one-dimensional rupture (Haskell, 1964).

The objective of this thesis is the characterization of the seismic source parameters, such as the earthquake size and the stress drop, using the amplitude spectrum of the displacement records and assuming that the earthquake behaves as a circular crack (Keilis-Borok, 1959).

Several methods for the characterization of the source using a spectral analysis have been proposed in literature. They are mainly based on a spectral fitting and in most cases they make use of theoretical Green functions (TGFs) with a frequency-independent attenuation factor (Abercrombie, 1995). Prieto et al. (2007) proposed to perform a jackknife analysis (Quenouille, 1949; Tukey, 1958) to evaluate the confidence intervals of the source parameters, with the use of both TGFs and empirical Green functions (EGFs). Zollo et al. (2014) proposed a multi-step, iterative approach with the objective of reducing the correlation among the parameters.

Systematic comparison between different methodologies highlighted the dependence of the results on the fitting model, due to the high correlation between the parameters, especially comparing EGF and TGF based techniques (Ide et al. 2003; Oye et al., 2005).

A probabilistic approach can allow to investigate such a correlation, defining a probability density function (PDF) in the parameter space and allowing for a consistent estimate of the uncertainties. This approach is becoming more and more applied to inverse methods for the geophysics. Specifically to earthquake source characterization, probabilistic source inversion techniques are applied to earthquake location (Lomax et al., 2000) kinematic source characterization (Song and Somerville, 2010) and kinematic source inversion (Minson et al, 2013; Piatanesi et al., 2007; Stahler and Sigloch, 2014).

Independently of the strategy used to solve the inverse problem, the search for a best solution involves the use of an optimization technique which should

account for the non-linearity of the problem, owing to both source and propagation. Local minimization techniques, based on linearization, can be adopted; several numerical methods (Levenberg, 1944; Marquardt, 1963; Fletcher, 1987; Nocedal and Wright, 2006) mostly based on the Gauss-Newton method or on the gradient-descent method (Cauchy, 1847) have proved their efficacy, even with physical constraints, such as the non-negativity of the solution, although they do not guarantee to reach the global minimum of the cost function. The possibility of having identified a local, not a global minimum must be always carefully taken into account.
Different global techniques have been developed, based on a deterministic approach, such as the cutting-plane (Gomori, 1960, 1963; Balas et al., 1993) and the branch and bound method (Land and Doig, 1960), or based on a stochastic approach, such as the Monte Carlo methods (Turing, 1950; Kahn and Harris, 1951), the Simulated Annealing method (Kirkpatrick et al., 1983) and the Genetic Algorithms (Goldberg, 1989).
In this work, we will use a mixed optimization method, the Basin-Hopping technique (Wales and Doye, 1997; Wales, 2003), that combines the overall global search with local minimization at each step, to accelerate the search for the minimum.

1.2. Objectives

Using the probabilistic framework developed by Tarantola (2005), and specifically the notion of conjunction of states of information, I developed a probabilistic approach to retrieve the source parameters (the earthquake size and the stress drop) and to characterize the decay of the amplitude spectrum with frequency, assuming a circular rupture model (Brune, 1970).
As discussed previously, information on the source of an earthquake requires the modeling of the wave propagation too. A possibility is represented by the

use of EGFs that allow to remove the propagation effect from the observations. However, also in this case robustness of the results is not guaranteed; while limitation of massive application of this technique to a generic dataset is introduced by the necessity to dispose of appropriate couples of events one of which has to play the role of the EGF. For these reasons, we choose to use in this work the TGFs, adding one parameter to invert related to the propagation (a frequency-independent Q-factor) beyond the three source parameter that we want to retrieve.

I model the observations with an operator, defined on these four parameters, which is non-linear; thus, a global exploration of the model space is required in order to find the best solution to describe the data.

Additionally, the joint a-posteriori probability density function (PDF) is computed around the best model, to extract the correlation matrix of the parameters. This allows to obtain estimates and uncertainties from the PDF, that are taking into account the correlations.

The global exploration relies on the building of a Markov chain in the parameter space and on the combination of a deterministic minimization with a random exploration of the space (Basin-Hopping method, Wales and Doye, 1997; Wales, 2003).

The main advantages of this new methodology are the following:

- A fully probabilistic approach associated with a global exploration method can provide a robust information about the “best-fit” model, with correct estimation of uncertainties and parameter correlation.
- The shape of the estimated PDF can assess the quality of the solutions, allowing to rule out noisy data and thus enabling the use of the method for automatic processing of large datasets.

1.3. Summary

The thesis is organized in 9 chapters, including the introduction and the conclusions.

Chapter 2 defines the analytical framework whereby the seismic source and the wave propagation can be properly described. It specifically describes the source and propagation models used in the work.

Chapter 3 describes the probabilistic method proposed to perform the source parameters inversion. I define first the inverse problem, thus the probabilistic framework used to solve the problem, discussing the assumptions of the method. Then I explain how the solution is retrieved, from the Basin-Hopping global exploration technique to the joint PDF. Finally, synthetic tests are performed to validate the method .

Chapters 4, 5, 6 are three applications of the method. In Chapter 4, I analyzed the Central Italy 2016-2017 sequence, characterizing the source of all the earthquakes with magnitude $M_L \geq 4.0$ (56 events); in Chapter 5 I characterized the source of more than 40000 LFEs occurred in the Nankai region (Japan) during the period 2012-2016; in Chapter 6 I analyzed the micro-seismicity ($M_j = 0.0 - 4.5$, 1061 events) occurred from 2016 to 2017 in the Northern Ibaraki region (Japan).

Chapter 7 describes the software implementation (SPAR, Source PARameter estimator) of the method.

Chapter 8, is the published version of the manuscript "*Performance of Earthquake Early Warning Systems during the 2016–2017 M_W 5–6.5 Central Italy Sequence*" published on Seismological Research Letters (Festa et al., 2018), that I co-authored. This paper analyzes the performance of network-based and stand-alone (on-site) early warning systems during the 2016–2017 Central Italy sequence. For this study, I provided and organized

the dataset on which the test was performed, and the information about the source parameters of the events needed to analyze the performances and contributed to the statistical analysis on which the performances are based. Chapters 3 and 4 are object of a manuscript submitted to the Geophysical Journal International (https://arxiv.org/abs/1811.06049); Chapter 5 and chapter 6 are object of two manuscripts in preparation.

2. Source models and observations

The study of the earthquakes is generally performed by analyzing the response of the Earth in terms of ground motion due to natural or artificial sources. For the aim, it is necessary to define the analytical framework, whereby the seismic source and the wave propagation can be described through an equation of motion of the rock particles, whose solution is the displacement at a general point in the propagation medium, as the effect of the passage of the seismic waves.

The seismic source represents a dynamic process that generates seismic waves. This process can be external to the solid Earth, such as ocean waves and atmospheric explosions, or can occur in the subsoil. In the latter case, we can distinguish between faulting sources, which involve shear motion across a surface inside the Earth, and volume sources, such as human-made underground explosions (an underground nuclear test, for instance) or, rarely, natural explosive or implosive sources.

In this work, we focus our attention on the most important natural seismic sources, the faulting sources. We will discuss the simplest model of seismic source, the point source, and then we will introduce the finite source model we are going to use, the circular fault model. This model remains simple, because it accounts for finiteness of the source through a small number of parameters. More complex source models have also been developed, using both kinematic and dynamic approaches. However, for most events analyzed in this study we do not have the resolution to look at the fine details of a complex rupture.

The last part of the chapter is reserved to the data we are going to analyze: the seismograms.

A seismogram records the source effects combined with the effects of propagation, since the energy released in the source region turns into seismic waves and heat.
Accelerometric and velocimetric records are usually provided by seismic networks; using both data, it is possible to obtain an information about the displacement in a broad frequency domain: this allows to increase the resolution on the displacement spectrum, that is the data we want to model.

2.1. Green functions

2.1.1. Elastic Green function

The displacement of a particle, $\mathbf{u}(\mathbf{x}_0, t)$, is defined as the difference between the position of a particle $\mathbf{x}(t)$ at time t and the position $\mathbf{x}_0(t_0)$ at the reference time t_0 .

The Newton's second law of motion for a material volume V of the continuum, with surface S , is :

$$\frac{\partial}{\partial t}\int_V \rho \dot{\mathbf{u}} dV = \int_V \mathbf{f} dV + \int_S \mathbf{T} dS \qquad (2.1)$$

where ρ is the material density, $\mathbf{f}$ are the body forces per volume unit, namely the non-contact forces acting on the particle inside V , and $\mathbf{T}(\mathbf{n})$ is the traction, that is the contact force per unit area acting on a point of the surface S identified by the normal $\mathbf{n}$.

We define the stress tensor

$$\sigma_{kl} \equiv T_l(\hat{e}_k) \qquad (2.2)$$

where the *kl*-th component is the contact force per unit area acting in the *l*-th direction on the surface perpendicular to the *k*-th direction (Figure 2.1).
It follows that

$$T_i = \sigma_{ji} n_j \tag{2.3}$$

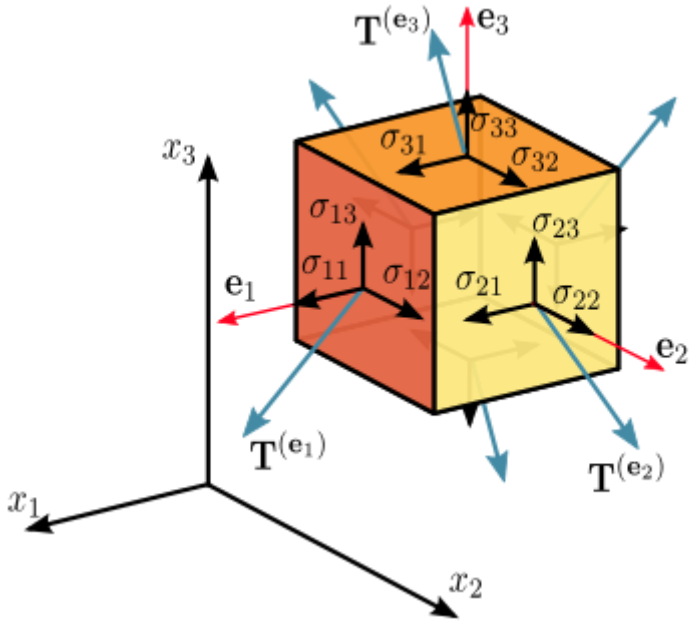

Figure 2.1 The stress tensor

It is possible to prove that the stress tensor is symmetric:

$$\sigma_{kl} = \sigma_{lk} \tag{2.4}$$

Due to this symmetry, the equation of motion (2.1) becomes :

$$\rho \ddot{u}_i = f_i + \sigma_{ij,j} \tag{2.5}$$

where $\sigma_{ij,j} \equiv \dfrac{\partial \sigma_{ij}}{\partial x_j}$.

For an isotropic, linearly elastic medium the stress tensor is related to the displacement by the constitutive relationship :

$$\sigma_{ij} = \lambda \delta_{ij} \nabla \cdot \mathbf{u} + \mu \left(\frac{\partial u_i}{\partial x_j} + \frac{\partial u_j}{\partial x_i} \right) \tag{2.6}$$

where λ and μ are the Lamé constants. For a homogeneous medium, the combination (2.5) and (2.6) leads to the following elastodynamic wave equation :

$$\rho \frac{\partial^2}{\partial t^2}\mathbf{u}(\mathbf{x},t) = (\lambda + 2\mu)\nabla(\nabla \cdot \mathbf{u}(\mathbf{x},t)) - \mu(\nabla \wedge \nabla \wedge \mathbf{u}(\mathbf{x},t)) + \mathbf{f}(\mathbf{x},t) \qquad (2.7)$$

If we consider a directional point force – the source – located at a point $\mathbf{x}_0$, we can write the force density as:

$$\mathbf{f}(\mathbf{x},t) = \hat{\mathbf{f}} \cdot s(t) \cdot \delta(\mathbf{x} - \mathbf{x}_0) \qquad (2.8)$$

where $s(t)$ is called source time function. We are assuming that the force has a time varying amplitude at a fixed point $\mathbf{x}_0$, with a fixed direction $\hat{\mathbf{f}}$; in seismology, separation between the geometry of the source and its time variation is a very common assumption; in this simple case, the geometry is represented by the term $\hat{\mathbf{f}} \cdot \delta(\mathbf{x} - \mathbf{x}_0)$.

The solution of the equation (2.7), when considering (2.8), is by definition the Green function of the homogeneous elastic isotropic medium that we are considering. Using the Fourier transform :

$$\tilde{u}(x,\omega) = \int_{-\infty}^{\infty} u(x,t) e^{-i\omega t} dt \qquad (2.9)$$

and choosing homogeneous initial conditions:

$$\mathbf{u}(\mathbf{x},0) = \dot{\mathbf{u}}(\mathbf{x},0) = 0 \qquad (2.10)$$

the solution in the frequency domain is (Achenbach, 1975) :

$$\begin{aligned}\tilde{\mathbf{u}}(R,\omega) = {} & \frac{1}{4\pi\rho}\left[\mathbf{f} \cdot \nabla\nabla\left(\frac{1}{R}\right)\right]\frac{\tilde{s}(\omega)}{\omega^2}\left[-\left(1 + \frac{i\omega R}{\alpha}\right)e^{-i\omega R/\alpha} + \left(1 + \frac{i\omega R}{\beta}\right)e^{-i\omega R/\beta}\right] \\ & + \frac{1}{4\pi\rho\alpha^2}\frac{1}{R}\left[\left(\mathbf{f} \cdot \nabla R\right)\nabla R\right]\tilde{s}(\omega)e^{-i\omega R/\alpha} \\ & + \frac{1}{4\pi\rho\beta^2}\frac{1}{R}\left[\mathbf{f} - \left(\mathbf{f} \cdot \nabla R\right)\nabla R\right]\tilde{s}(\omega)e^{-i\omega R/\beta}\end{aligned} \qquad (2.11)$$

where $\alpha = \sqrt{\frac{\lambda + 2\mu}{\rho}}$ is the P-wave velocity, $\beta = \sqrt{\frac{\mu}{\rho}}$ is the S-wave velocity, and $R = \|\mathbf{x} - \mathbf{x}_0\|$ the source receiver distance.

Using the inverse Fourier transform :

$$u(x,t) = \frac{1}{2\pi} \int_{-\infty}^{\infty} \tilde{u}(x,\omega) e^{i\omega t} dt \tag{2.12}$$

we obtain the solution in the time domain :

$$\begin{aligned} \mathbf{u}(R,t) = {} & \frac{1}{4\pi\rho} \left[\mathbf{f} \cdot \nabla\nabla \left(\frac{1}{R} \right) \right] \int_{R/\alpha}^{\min(t,R/\beta)} \tau s(t-\tau) d\tau + \\ & + \frac{1}{4\pi\rho\alpha^2} \frac{1}{R} \left[(\mathbf{f} \cdot \nabla R) \nabla R \right] s\left(t - \frac{R}{\alpha} \right) + \\ & + \frac{1}{4\pi\rho\beta^2} \frac{1}{R} \left[\mathbf{f} - (\mathbf{f} \cdot \nabla R) \nabla R \right] s\left(t - \frac{R}{\beta} \right) \end{aligned} \tag{2.13}$$

This is the representation for the displacement $\mathbf{u}$ at a general point in space and time, for a point source force localized in space.

2.1.2. Far field and near field waves

From (2.11) we observe that the behavior of the Green function depends on the two quantities $\frac{\omega R}{\alpha}$ and $\frac{\omega R}{\beta}$. By definition $\alpha > \beta$, so we can define a unique condition:

$$\frac{\omega R}{\alpha} \gg 1 \tag{2.14}$$

for which the first term of (2.11) and (2.13) is negligible with respect to the last two terms. This is called the far field condition; if we consider the wavelength $\lambda = \frac{2\pi\alpha}{\omega}$, the latter becomes:

$$\frac{R}{\lambda} \gg 1 \tag{2.15}$$

The far field condition depends both on the distance between the source and the observer and on the wavelength of the radiation.

In this work, we will assume that the observed data verify the far field condition for the whole explored frequency band. Again, this is an assumption usually verified in seismology when the observations are at a few wavelengths of distance from the source.

In the time domain, the far field representation can be rearranged as follows:

$$\begin{aligned}
\mathbf{u}_{FF}(R,t) &= \mathbf{u}^{P}_{FF}(R,t) + \mathbf{u}^{S}_{FF}(R,t) \\
\mathbf{u}^{P}_{FF}(R,t) &= \frac{1}{4\pi\rho\alpha^2}\frac{1}{R}\mathfrak{R}^{P}_{FF}s\left(t-\frac{R}{\alpha}\right) \\
\mathbf{u}^{S}_{FF}(R,t) &= \frac{1}{4\pi\rho\beta^2}\frac{1}{R}\mathfrak{R}^{S}_{FF}s\left(t-\frac{R}{\beta}\right)
\end{aligned} \tag{2.16}$$

$\mathfrak{R}^{P}_{FF}$ and $\mathfrak{R}^{S}_{FF}$ are called radiation patterns for P and S waves respectively, and are defined as follows :

$$\begin{aligned}
\mathfrak{R}^{P}_{FF} &= f_R\hat{\mathbf{e}}_R \\
\mathfrak{R}^{S}_{FF} &= \mathbf{f}_T
\end{aligned} \tag{2.17}$$

with $\mathbf{e}_R \equiv \mathbf{x}-\mathbf{x}_0$, $f_R \equiv \mathbf{f}\cdot\mathbf{e}_R$ the radial component of the point force and $\mathbf{f}_T \equiv \mathbf{f} - f_R\mathbf{e}_R$ the transverse component.

Having fixed the origin of the spherical reference frame in the source, the first term indicates a wave that propagates along the radial component of the point force, with velocity α ; it is called P-wave, and is a compressional wave : the direction of the particle motion is the direction of wave propagation (longitudinal wave).

The second term indicates a wave that propagates still along the radial direction, but it generates motions in the orthogonal direction; this wave propagates with velocity β ; it is called S-wave, and is a shear wave: the direction of the particle motion is orthogonal to the direction of wave propagation (transversal wave).

Both P- and S-waves decay as a function of the source-receiver distance as $\frac{1}{R}$. We define the geometrical spreading

$$A^c(\mathbf{x},\mathbf{x}_0) \equiv \frac{1}{\|\mathbf{x}-\mathbf{x}_0\|} \tag{2.18}$$

and the travel-time

$$T^c(\mathbf{x},\mathbf{x}_0) \equiv \frac{\|\mathbf{x}-\mathbf{x}_0\|}{v_c} \tag{2.19}$$

which is the time required to the selected phase c, P- or S- wave, with velocity v_c, to travel from the source at $\mathbf{x}_0$ to the receiver at $\mathbf{x}$.

When the condition (2.15) does not hold, the first term of (2.11) and (2.13) must be considered. This term is referred to as near field term and decays faster than $\frac{1}{R}$: at larger distances from the source it decays as $\frac{1}{R^2}$.

If we consider a more complex propagation medium, a 1D horizontally layered medium, the Green function is still characterized by near field and far field terms. The travel-time T^c is still related to the wave propagation velocity, which now is a velocity field, $v_c(z)$; it must satisfy the Eikonal equation :

$$\left|\nabla T^c\right|^2 = \frac{1}{v_c^2} \tag{2.20}$$

The ray path followed by the wave-front during the propagation is determined by the Fermat principle, which states that the ray path from $\mathbf{x}_0$ to $\mathbf{x}$ is the one for which the travel-time

$$\int_{\mathbf{x}_0}^{\mathbf{x}} \frac{|d\mathbf{x}|}{v_c(z)} \tag{2.21}$$

is stationary.

In this case, the geometrical spreading will depend on the length of the ray path.

2.1.3. Anelastic attenuation

When a wave propagates through a real medium, wave amplitudes attenuate as a result of the internal friction of the material; real propagation media are anelastic, and anelastic attenuation must be taken into account in the Green functions used to model the propagation from the source of an earthquake to the receiver.

The effect of the internal friction can be described by an anelastic attenuation factor (quality factor), Q , defined as follows :

$$\frac{1}{Q(f)} \equiv -\frac{\Delta E}{2\pi E} \tag{2.22}$$

where ΔE is the energy lost due to non- elasticity, and E is the peak deformation energy of the medium at a given frequency.

Observations show that in most of the cases the quality factor is frequency independent. Under this hypothesis, from the definition (2.22) is possible to obtain the corresponding Green function in the frequency domain, under the far field approximation :

$$\tilde{G}(Q^c; f) = K^c A^c(\mathbf{x}, \mathbf{x}_0) e^{-\frac{T^c(\mathbf{x},\mathbf{x}_0)}{Q^c}\pi f} \tag{2.23}$$

where Q^c depends on the selected phase c of the seismic wave, and K^c is a constant, depending on the source-receiver geometrical configuration and on the elastic properties of the medium; for a 1D horizontally layered medium :

$$K^c = \frac{\Re^c_{FF} F_S}{4\pi\rho(\mathbf{x}_0)^{1/2}\rho(\mathbf{x})^{1/2} v_c(\mathbf{x}_0)^{5/2} v_c(\mathbf{x})^{1/2}} \tag{2.24}$$

$\Re^c_{FF}$ is the radiation pattern, depending on the phase c , F_S is the free-surface correction coefficient, ρ is the density and v_c is the wave velocity.

The representation (2.23) has a criticality in the time domain: a pulse propagating from the origin $\mathbf{x}=\mathbf{0}$ starting at time $t=0$ will show an amplitude different from zero at $\mathbf{x}=\mathbf{0}$ even before $t=0$. Since the violation of the elementary notion of causality is not acceptable, a material dispersion in an attenuating medium must be introduced, in order to use a frequency independent Q in the time domain.

The standard linear solid (SLS) model (Zener, 1948) is a way of representing both attenuation and dispersion; a combination of these models reproduces the approximately constant Q behavior which is usually reported for the frequency range of observation in solids (Knopoff, 1964).

2.2. Point source : The double couple solution

From a kinematic point a view, a faulting source consists in a dislocation over a region of finite size, S : the relative motion of the two surfaces of the fault is called slip, D.

Since faulting sources are localized in a volume inside the Earth, they must satisfy the following conditions :

$$\begin{aligned} \sum \mathbf{f} &= \mathbf{0} \\ \sum \mathbf{f} \wedge \mathbf{r} &= \mathbf{0} \end{aligned} \tag{2.25}$$

The Green function from the directional force (2.8) does not satisfy these conditions. The simplest model that satisfies (2.25) consists in a double couple of forces (Figure 2.2), centered on the point source $\mathbf{x}_0$ and having equal moment – assuming $\mathbf{x}_0$ as reference point – in magnitude and opposite moment in direction.

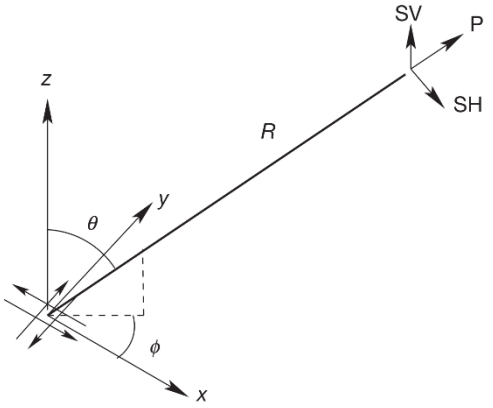

Figure 2.2 Double couple source model. The hypocenter is in the origin of the reference system; R, θ, ϕ are the spherical coordinates. Figure from Madariaga, Treatise on Geophysics (2015).

Each force of the couple is of the type (2.8). One of the couples has the direction of the slip, the other is orthogonal to the surface hosting the rupture.

For each couple, the total displacement $\mathbf{u}(\mathbf{x},t)$ is the difference between the solution (2.13) evaluated for $\mathbf{f}(\mathbf{x},t)$ applied at $\mathbf{x}_0 + \delta$ and for $\mathbf{f}(\mathbf{x},t)$ applied at $\mathbf{x}_0$, with δ arm of the couple.

Considering the limit for $\delta \to 0$, and consequently $|\mathbf{f}| \to \infty$ such that the product $\delta \cdot |\mathbf{f}| \equiv M_0$ - magnitude of the moment of one of the couples – remains finite, it is possible to obtain the displacement due to a point dislocation :

$$\begin{aligned}\mathbf{u}(\mathbf{x},t) = {} & \frac{1}{4\pi\rho}\Re_{NF}\frac{1}{R^4}\int_{R/\alpha}^{R/\beta}\tau M_0(t-\tau)\,d\tau + \\ & + \frac{1}{4\pi\rho v_P^2}\Re_{IF}^P\frac{1}{R^2}M_0\left(t-\frac{R}{\alpha}\right) + \frac{1}{4\pi\rho v_S^2}\Re_{IF}^S\frac{1}{R^2}M_0\left(t-\frac{R}{\beta}\right) + \\ & + \frac{1}{4\pi\rho v_P^3}\Re_{FF}^P\frac{1}{R}\dot{M}_0\left(t-\frac{R}{\alpha}\right) + \frac{1}{4\pi\rho v_S^3}\Re_{FF}^S\frac{1}{R}\dot{M}_0\left(t-\frac{R}{\beta}\right)\end{aligned} \qquad (2.26)$$

The moment M_0 is called seismic moment; it is related to the source kinematic properties as follows :

$$M_0(t) = \mu \bar{D}(t) S \tag{2.27}$$

where μ is the shear modulus and $\bar{D}$ is the average slip on the fault.

The radiation patterns of the far field, $\Re_{FF}^{P}$ and $\Re_{FF}^{S}$ (Aki and Richards, 1980), are represented in Figure 2.3; it is remarkable that, for almost all the earthquakes, the observed radiation pattern are in agreement with these diagrams.

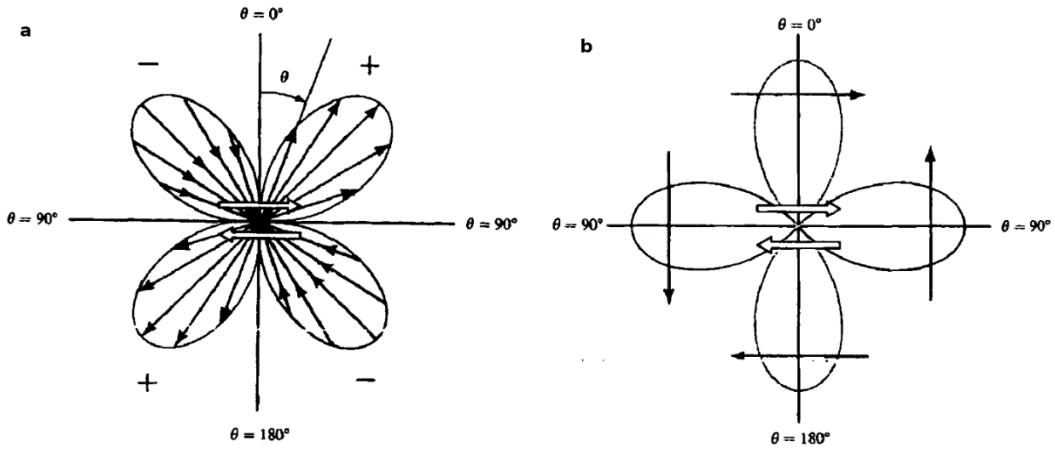

Figure 2.3 Radiation patterns of the P term (a) and S term (b) of the far field displacement. The central pair of arrows shows the shear dislocation; the arrows imposed on each lobe show the direction of particle displacement. Figure from Aki and Richards, Quantitative Seismology (1980).

In addition to the near field and far field terms, there are two new terms called intermediate field terms, with radiation patterns $\Re_{IF}$; they are negligible in the far field approximation, but often they must be considered in the near field. As for the Green function (2.16), in the far field the waves still decay as $\frac{1}{R}$.

2.3. Seismic radiation in the spectral domain

It is usually observed that the complexity of the seismic radiation affects less the far field displacement spectra, which share these common features for most real earthquakes :

- At low frequencies the amplitude spectrum is a plateau
- A decay with a coherent slope is observed, starting from the end of the plateau

The physical interpretation of these features is very simple, but can be very helpful for understanding the seismic radiation:

- The plateau is observed in the frequency domain for which the source is seen as a point. In that domain, interaction among different points of the source cannot be seen due to wavelength resolution, and the source acts as a point with a unique behavior; we call this flat level of the spectrum Ω_0 , and mathematically it can be written as the limit :

$$\lim_{\omega \to 0} \tilde{u}(\omega) = \int_{-\infty}^{\infty} u(t)dt \equiv \Omega_0 \qquad (2.28)$$

  As we will see in the following section, Ω_0 is related to the total moment released by an earthquake, M_0 .

- Beyond a certain frequency, namely the corner frequency f_c , the observer has the resolution to distinguish the interactions from different points of the source; this effect is a coherent, destructive, interference that can be modeled by a power-law.

  The observed corner frequency must be therefore related to the dimension of the source. Again, in the following section we will see different models that connect f_c to the source size.

The simplest representation for this kind of spectrum is the following :

$$\tilde{u}(f) = \frac{\Omega_0}{1 + \left(\frac{f}{f_c} \right)^{\gamma}} \tag{2.29}$$

where γ is the power law exponent, and $f = \frac{\omega}{2\pi}$ is the frequency.

This behavior can be obtained using the double-couple solution described in the previous section 2.2, by appropriating selecting the source function $M_0(t)$. As an example, if we consider a source function having the shape of a triangle, the representation of the far field displacement spectrum coming from (2.26) will be of the type (2.29) : the corner frequency f_c will be inversely proportional to the width of the triangle, the seismic moment M_0 will be proportional to the area of the triangle, and the spectrum will decay with $\gamma = 2$.

Nevertheless, the double-couple model is not able to associate to this time scale a characteristic length related to the earthquake phenomenon, because of its definition of point dislocation; our interest, instead, lies in the estimation of the size of the earthquake rupture .

We therefore complexify the point source model, including some additional physical ingredients of the rupture. From a dynamic point of view, a seismic source enucleates when, due to the stress conditions along the two surfaces of a fault, a change in the frictional state of the system happens, moving from static to dynamic friction. The resulting stress drop, $\Delta\sigma$, causes the relative motion of the two surfaces that we call slip, D.

Observations show that as the seismic moment increases, the corner frequency decreases. Thus, the larger the moment release, the larger the duration and the earthquake size. In order to estimate this dimension, we will use an extended source model, the circular fault model, described in the following section.

This will allow us to obtain information about the kinematic and dynamic parameters that are required to describe the seismic source.

2.4. The circular fault model

The simplest model of a static circular crack is obtained under the assumption of a constant stress drop $\Delta\sigma$; in this case the slip is (Keilis-Borok, 1959) :

$$D(a) = \frac{24}{7\pi}\frac{\Delta\sigma}{\mu}\sqrt{r^2 - a^2} \tag{2.30}$$

where r is the radius of the crack and a is the distance from the center of the crack. This result represents one of the most important properties of the circular crack, and it is widely used in seismology : the slip on the fault is proportional to the radius of the crack, and the constant of proportionality is driven by the stress drop.

Using (2.30) to compute the seismic moment (2.27), we obtain :

$$M_0 = \frac{16}{7}\Delta\sigma \cdot r^3 \tag{2.31}$$

In this case, the seismic moment scales like the third power of the rupture size, and the constant of proportionality is independent of the size of the earthquake (Aki, 1967), under the assumption of a scale independent stress drop.

It is widely observed for different sets of earthquakes (Abercrombie, 1995; Ide and Beroza, 2001; Ide et al., 2003) that the seismic moment scales like the inverse third power of the corner frequency f_c :

$$M_0 \propto \frac{1}{f_c^3} \tag{2.32}$$

We will now introduce two circular fault models, the Brune's model and the Madariaga's model, that relate the radius of the fault to the inverse of the

corner frequency; therefore, they provide a solid connection among the observed scaling law (2.32) and the expected one (2.31).

2.4.1. Brune's model

In 1970, Brune proposed a circular crack model for seismic source characterized by a pure shear stress pulse σ applied instantaneously to the fault. No dynamic propagation effects are allowed. The stress pulse generates a pure shear stress wave propagating perpendicular to the dislocation surface:

$$\sigma(x,t) = \sigma H\left(t - \frac{x}{\beta}\right) \tag{2.33}$$

Where H is the Heaviside function, x is the distance from the fault plane and β is the shear wave velocity.

This corresponds to the following source time function:

$$s(t) = M_0 4\pi^2 f_c^2 \left(t - \frac{x}{\beta}\right) \cdot e^{-2\pi f_c \cdot \left(t - \frac{x}{\beta}\right)} H\left(t - \frac{x}{\beta}\right) \tag{2.34}$$

In the far field domain, the spectral amplitude of this causal function gives a representation in the frequency domain of the type (2.29) :

$$\tilde{s}(f) = \frac{M_0}{1 + \left(\frac{f}{f_c}\right)^2} \tag{2.35}$$

The flat level of the spectrum is equal to the seismic moment and the exponent of the high-frequency decay is equal to 2.Using the static solution of Keilis-Borok (1959), it follows that the relation among the corner frequency f_c and the radius of the fault r is :

$$f_c = 0.3724 \cdot \frac{\beta}{r} \tag{2.36}$$

For a circular crack, the static strain energy change ΔW is :

$$\Delta W \equiv \frac{1}{2}\int_S \Delta\sigma D dS \tag{2.37}$$

From the Brune's model, the energy radiated as S-waves, E_S, is a percentage of the total available strain energy :

$$E_S = 0.44 \cdot \Delta W \tag{2.38}$$

The result (2.36) insures the equivalence between the scaling laws (2.32) and (2.31).

In this work, we will use a generalized Brune's model which provides a displacement spectrum where the power law exponent is not fixed to 2, but it is a free parameter of the model :

$$\tilde{s}(f) = \frac{M_0}{1+\left(\frac{f}{f_c}\right)^{\gamma}} \tag{2.39}$$

This choice is motivated by the observed far field displacement spectra, which in several cases show a decay with a power law exponent different from 2.

It is worth to note that there is a physical bound for the minimum value of γ. Requiring the finiteness of the seismic energy, E_S , it follows that $\gamma \geq 1.5$:

Since we have

$$E_S \propto \int_0^{\infty} (2\pi f)^2 \left|\tilde{s}(f)\right|^2 df \tag{2.40}$$

From (2.39) it follows :

$$E_S \propto \int_0^{\infty} f^2 \left[\frac{M_0}{1+(f/f_c)^{\gamma}}\right]^2 df \tag{2.41}$$

A singularity may arise when considering the upper limit of the integration :

$$\lim_{f\to\infty} f^2\left[\frac{M_0}{1+\left(f/f_c\right)^{\gamma}}\right]^2 \approx \frac{f^2}{f^{2\gamma}} = \frac{1}{f^{2\gamma-2}} \tag{2.42}$$

and, consequently, the convergence of (2.41) must be evaluated requiring :

$$\frac{1}{f^{2\gamma-2}} < \frac{1}{f} \tag{2.43}$$

It is satisfied if :

$$\gamma > \frac{3}{2} \tag{2.44}$$

□ .

In one of the performed applications of the method (Chapter 6), we tested these two different models and we proved that the generalized Brune's model is able to better describe the observed data.

2.4.2.Madariaga's model

In 1976 Maradiaga proposed a quasi-dynamic circular crack model, namely a circular crack that starts from a point and grows with a constant rupture speed until it stops on the border of the fault, due to unbreakable barriers.
The spectral representation provided by this model is of the same type (2.29) of the Brune's representation. Nevertheless, the interpretation of the parameter f_c is different :

$$f_c = 0.21\cdot\frac{\beta}{r} \tag{2.45}$$

This estimation comes from the assumption of a rupture speed $v_R = 0.9\beta$, averaging the expected directivity effect on corner frequency; unlike the Brune's model, f_c here is therefore related to the rupture duration.

The choice between the Brune's or Maradiaga's model does not affect the shape of the expected displacement spectrum; therefore, it does not change the estimates of the model parameters. It only affects the estimate of the

source radius, and therefore of the stress drop obtained from (2.31). Specifically, the Madariaga stress drop is about 5.5 times larger than the Brune one.

2.5. Displacement or velocity measurements

Observations in Seismology are constituted by the ground motion records; seismic networks usually provide records from 3-components accelerometers and/or velocimeters.

As we have seen, the complexity of the seismic radiation is generally reduced moving from the acceleration to the displacement, because the lower the frequency content, the simpler the waveforms. For this reason, we will estimate source parameters using ground motion displacement spectra.

Since the displacement is a low frequency quantity, it is more sensitive to the seismic moment, than the velocity or the acceleration, but less sensitive to the higher-frequency parameters, such as the corner frequency or the high-frequency decay γ. If we compute the velocity spectrum from the displacement spectrum (2.29) using the Fourier transform properties :

$$\tilde{\dot{u}}(f) = i2\pi f \cdot \tilde{u}(f) \tag{2.46}$$

we can note that this spectrum has a peak at the corner frequency f_c . Therefore, one could estimate this fundamental parameter from an instantaneous measurement on the velocity spectrum. Nevertheless, usually velocity spectra from recorded earthquakes are characterized by a broadened peak, polluted by oscillations and secondary peaks.

For this reason, in this work we choose to estimate the source parameters using an integral measurement over the displacement spectrum, building a probabilistic framework to obtain a robust estimation of the uncertainties that affect the parameters' measurement.

3. The method : source parameters inversion

3.1. The inverse problem

In this chapter we discuss how to characterize the source of an earthquake modeling the observed ground motion.

As we have seen in Chapter 2, in linear elasticity, the displacement produced by a point source and recorded at a given receiver is the convolution of the source time function by the Green's propagator. Thus, the displacement spectral amplitude in the frequency domain $\tilde{u}(f)$ can be factorized as $\tilde{u}(f) = \tilde{S}(f)\tilde{G}(f)$, where f is the frequency, $\tilde{S}(f)$ is the modulus of the Fourier transform of the source time function and $\tilde{G}(f)$ the modulus of the Fourier transform of the Green propagator. We separately model the far field P- and S-waves. For the source contribution, we consider the generalized Brune's model introduced in Section 2.4.1 :

$$\tilde{S}(M_0, f_c, \gamma; f) = \frac{M_0}{1+\left(\frac{f}{f_c}\right)^{\gamma}} \tag{3.1}$$

with $\tilde{S}$ depending on three parameters: the seismic moment M_0, the corner frequency f_c and the high frequency spectral decay factor γ.

For the propagation contribution, we consider the Green function introduced in Section 2.1.3 :

$$\tilde{G}(Q^c; f) = K^c A^c(\mathbf{x}, \mathbf{x}_0) e^{-\pi f \cdot T^c(\mathbf{x}, \mathbf{x}_0) Q^c} \tag{3.2}$$

In the above formula, K^c is a constant, depending on the source-receiver geometrical configuration and the elastic properties of the medium crossed by the waves, $A^c(\mathbf{x}, \mathbf{x}_0)$ and $T^c(\mathbf{x}, \mathbf{x}_0)$ are the geometrical spreading and the

travel-time related to the selected wave from the source at $\mathbf{x}_0$ to the receiver at $\mathbf{x}$, respectively, Q^c is a frequency independent attenuation quality factor and $Q'^c = \frac{1}{Q^c}$ is the reciprocal of the quality factor.

For a 1D layered model, under the far field approximation (2.15), the analytical representation of the constant K^c is (Aki and Richards, 1980)

$$K^c = \frac{R^c_{FF} F_S}{4\pi\rho(\mathbf{x}_0)^{1/2}\rho(\mathbf{x})^{1/2}c(\mathbf{x}_0)^{5/2}c(\mathbf{x})^{1/2}} \tag{3.3}$$

Here R^c_{FF} is the radiation pattern contribution, depending on the phase *c* (P- or S-wave), F_S is the free-surface correction coefficient, ρ is the density and *c* the wave velocity. In the applications of this thesis, ρ and c values depend on the adopted velocity model, while we use averaged values for the radiation pattern (Boore and Boatwright, 1984). The geometrical spreading describes how the amplitude decays as a function of the distance from the source; both the geometrical spreading and the travel time can be computed using the ray theory. They reduce to $A^c(\mathbf{x},\mathbf{x}_0) = \frac{1}{\|\mathbf{x}-\mathbf{x}_0\|}$ and $T^c(\mathbf{x},\mathbf{x}_0) = \frac{\|\mathbf{x}-\mathbf{x}_0\|}{c}$ for a homogeneous medium, and the geometrical spreading is independent of the phase.

In our modelling, we assume K^c, $A^c(\mathbf{x},\mathbf{x}_0)$ and $T^c(\mathbf{x},\mathbf{x}_0)$ known; they are computed either in a homogeneous or in a 1D horizontally layered medium. Uncertainties in these terms contribute to the increase of the epistemic uncertainties on the source parameters and Q'^c estimations. Both the geometrical spreading and the constant K^c are scale factors for the seismic moment. They depend on the relative location of the source and the receiver and on the velocity structure crossed by the waves. However, because of the logarithmic scale of the seismic moment, their uncertainties poorly affect the

estimation of the event magnitude. The travel-time appears in formula (3.2) through the product $Q^{\prime c}\,T^c(\mathbf{r},\mathbf{r}_0)$, where the $Q^{\prime c}$ factor is retrieved from the inversion of the displacement spectra. Uncertainty on $T^c(\mathbf{r},\mathbf{r}_0)$ only affects the final estimate of $Q^{\prime c}$ and can be completely absorbed in the inversion of the quality factor.

What is unknown in the propagation contribution is, definitely, the quality factor; for this reason, the set of parameters that we want to estimate through the inverse problem will be composed by the three source parameters and, in addition, one propagation parameter : $(\log M_0,\, f_c, \gamma, Q^{\prime c})$.

Because of the exponential nature of the seismic moment, we define the forward operator as the logarithm of the displacement spectral amplitude:

$$\log \tilde{u} = \log M_0 - \log\left[1+\left(\frac{f}{f_c}\right)^{\gamma}\right] + \log \xi - \pi f T^c(\mathbf{r},\mathbf{r}_0) Q^{\prime c} \log e \qquad (3.4)$$

where $\xi = K^c A^c(\mathbf{r},\mathbf{r}_0)$; $\log\tilde{u}(\log M_0,\, f_c, \gamma, Q^{\prime c})$ depends on four unknown parameters that will be inverted analyzing the spectra obtained from seismic records. For sake of simplicity, we summarize the set of parameters to be estimated through the vector $\mathbf{m} = (\log M_0,\, f_c, \gamma, Q^{\prime c})$ and we indicate with **M** the model space, the subdomain of R^h, $h = 4$, which individuates the range of variability of the model parameters.

Although the equation (3.1) provides a continuous mapping between the parameter space and the theoretical amplitude spectrum, the displacement spectra obtained from observations are sampled at a discrete, finite set of points. Let us indicate with $\mathbf{d}_{obs} = \{\log \tilde{u}_{obs}(f_k), k = 0,1,..,n\}$ the logarithm of the discrete Fourier amplitude spectrum computed from the observed displacement; the vector $\mathbf{d}_{obs}$ belongs to the data space **D**. In the above relationship, $f_k = k f_{\min} = \frac{k}{T}$, where T is the window length of the selected

signal in time, $f_{\min} = \frac{1}{T}$ the minimum frequency in the spectrum, n is half of the number of samples in the time domain, and $f_n = nf_{\min} = \frac{1}{2\Delta t}$ the Nyquist frequency, where Δt is the time step of the recorded signal. It is worth to note that when using the FFT for spectral computation, the signal is padded to zero to satisfy the condition that n is a power of two. To compare theoretical and observed spectra, we then compute the theoretical prediction at the same discrete set of frequencies. Let us indicate with

$$\mathbf{g}(\mathbf{m}) = \left\{ \log \tilde{u}(\mathbf{m}; f_k), k = 0,..,n \right\} \tag{3.5}$$

the discrete forward operator. The solution of the inverse problem is indeed the set of parameters $\mathbf{m}^*$, such as $\mathbf{g}(\mathbf{m}^*)$ approaches $\mathbf{d}$ at best.

3.2. Probabilistic framework for the inverse problem

We introduce a probabilistic framework for the resolution of the inverse problem (Tarantola, 2005).

The definition of probability is based on the Kolmogorov axioms (Kolmogorov, 1933). Let's consider a finite-dimensional manifold $\aleph$; any subset of the manifold, $\Im \subseteq \aleph$, is called an *event*; the probability over $\aleph$ is a function that associates to any event $\Im$ a number $P(\Im)$ satisfying these 3 properties (axioms) :

$$\begin{aligned} & P(\Im) \in \mathbb{R}^+ \cup 0 \quad , \forall \Im \subseteq \aleph \\ & P(\aleph) = 1 \\ & P(\Im + \Im') = P(\Im) + P(\Im') \quad \textit{if } \Im \cap \Im' = \varnothing \quad , \forall \Im, \Im' \subseteq \aleph \end{aligned} \tag{3.6}$$

$P(\Im)$ is called *probability* of the event $\Im$; the function $P(\cdot)$ is called *probability distribution*.

If a coordinate system $\mathbf{x} = (x_1, ..., x_n)$ is defined over $\aleph$, it is possible to prove that a function $f(\mathbf{x})$ always exists such that (Radon-Nikodym theorem[1]) :

$$P(\Im) = \int_{\Im} f(\mathbf{x}) d\mathbf{x} \quad , \forall \Im \subseteq \aleph$$
$$with \quad \int_{\Im} d\mathbf{x} = \underbrace{\int dx_1 \cdots \int dx_n}_{over\ \Im} \tag{3.7}$$

$f(\mathbf{x})$ is called *probability density function* (PDF), and it represents $P(\cdot)$ with respect to the introduced coordinate system.

The solution of the general inverse problem obtained by Tarantola (2005) is based on the notion of *conjunction of states of information*. We will now introduce the *states of information* needed to obtain the solution, and we will define the operation *conjunction*. Each state of information is a probability density.

The *homogeneous probability density* $\mu(\mathbf{x})$ is defined as follows :

$$\mu(\mathbf{x}) = \frac{v(\mathbf{x})}{V} \tag{3.8}$$

where $v(\mathbf{x})$ is the volume density over the manifold $\aleph$ with respect to the coordinates $\mathbf{x}$ and $V = \int_{\aleph} v(\mathbf{x}) d\mathbf{x}$ is the volume of $\aleph$, that we assume to be finite.

$\mu(\mathbf{x})$ is able to associate to each event $\Im$ a probability

$$M(\Im) = \int_{\Im} \mu(\mathbf{x}) d\mathbf{x} \tag{3.9}$$

, the *homogeneous probability*, which is proportional to the volume of the event. In Bayesian inference theory, $\mu(\mathbf{x})$ is usually referred to as noninformative probability density.

[1] The theorem has been proved by Radon in 1913 for the special case $\aleph = \Re^n$; it has been generalized by Nikodym in 1930.

In this work we will use two simple manifolds, the model space $\mathbf{M}$ and the data space $\mathbf{D}$; these domains are cartesian spaces, and the homogeneous probability density is a constant. In general, this is not always the case; as a simple example we can consider the manifold $\aleph$ being the surface of a 2-D sphere: if (θ,ϕ) is a system of spherical coordinates, the homogeneous probability density is

$$\mu(\theta,\phi)=\frac{\sin\theta}{4\pi} \tag{3.10}$$

After defining the probability and homogeneous probability distributions, we are allowed to define the conjunction operation.

If P_1 and P_2 are two probability distributions and M is the homogeneous probability distribution over the manifold $\aleph$, the conjunction among P_1 and P_2 , $P_1 \wedge P_2$, is an operation that satisfies the following properties :

$$\begin{aligned} &P_1(\Im)=0 \quad or \quad P_2(\Im)=0 \quad \Rightarrow \quad (P_1 \wedge P_2)(\Im)=0 \quad \forall \Im \subseteq \aleph \\ &P_1 \wedge P_2 = P_2 \wedge P_1 \\ &P \wedge M = P \quad \forall P \end{aligned} \tag{3.11}$$

It is possible to prove that, if $f_1(\mathbf{x})$, $f_2(\mathbf{x})$ and $\mu(\mathbf{x})$ are the probability densities of P_1 , P_2 and M, respectively, the following definition of conjunction :

$$(f_1 \wedge f_2)(\mathbf{x}) \equiv \frac{1}{\nu}\frac{f_1(\mathbf{x})\,f_2(\mathbf{x})}{\mu(\mathbf{x})} \tag{3.12}$$

with ν normalization constant, always satisfies (3.11).

The conjunction is an associative operation :

$$\frac{(f_1 \wedge f_2 \wedge \ldots \wedge f_k)}{\mu(\mathbf{x})} = \frac{1}{\nu}\frac{f_1(\mathbf{x})}{\mu(\mathbf{x})}\frac{f_2(\mathbf{x})}{\mu(\mathbf{x})}\cdots\frac{f_k(\mathbf{x})}{\mu(\mathbf{x})} \tag{3.13}$$

The last elements that we need to introduce are the a-priori probability density functions over the model and data spaces, and the PDF that describes the connection – i.e. the physical theory – among the model parameters $\mathbf{m}$

and the observations $\mathbf{d}$. For this reason, from now on, we will specifically refer to the model and data spaces, $\mathbf{M}$ and $\mathbf{D}$, and not anymore to a generic manifold $\aleph$.

The a-priori probability density over the model space $\mathbf{M}$, $\rho_M(\mathbf{m})$, represents the information that is available for the model parameters independently of the observations.

The a-priori probability density over the data space $\mathbf{D}$, $\rho_D(\mathbf{d})$, represents the results of the measurement operation. If a *perfect* measure were possible observing $\mathbf{d}_{obs}$, the corresponding PDF would be :

$$\rho_D(\mathbf{d}) = \delta(\mathbf{d} - \mathbf{d}_{obs}) \tag{3.14}$$

where δ is the Dirac delta function. In measurements affected by uncertainties the a-priori PDF in the data space has a more complex representation.

Finally, we indicate with $\Theta(\mathbf{d},\mathbf{m})$ the joint probability density function over the cartesian product $\mathbf{D}\times\mathbf{M}$, that represents the information about the model prediction and its uncertainties. It is therefore connected to the physical theory we are using to model the observations : it has to be a function of the forward operator.

If having no theoretical uncertainties were possible – namely having an exact theory – the corresponding PDF would be :

$$\Theta(\mathbf{d},\mathbf{m}) = \delta(\mathbf{g}(\mathbf{m}) - \mathbf{d})\mu_M(\mathbf{m}) \tag{3.15}$$

If for each model $\mathbf{m}$ we associate a probability density for $\mathbf{d}$, $\theta(\mathbf{d}|\mathbf{m})$, we have :

$$\Theta(\mathbf{d},\mathbf{m}) = \theta(\mathbf{d}|\mathbf{m})\mu_M(\mathbf{m}) \tag{3.16}$$

These two different representations are visualized in Figure 3.1.

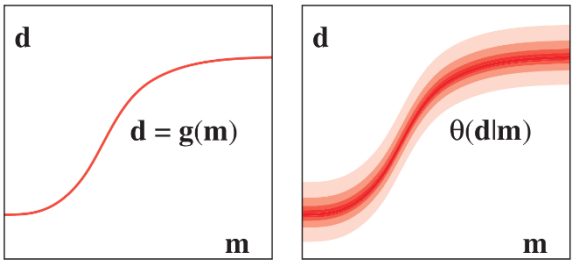

Figure 3.1 Modelization uncertainties. On the left, uncertainties in the forward modelization can be neglected (3.15); on the right, for each model $\mathbf{m}$ there is a probability density representing the uncertainties (3.16). Figure from Tarantola, Inverse Problem Theory (2005).

The a-priori information on the model space is, by definition, independent of the information on the data space; we can therefore obtain the joint a-priori PDF over $\mathbf{D}\times\mathbf{M}$ by multiplication :

$$\rho(\mathbf{d},\mathbf{m}) = \rho_D(\mathbf{d})\rho_M(\mathbf{m}) \tag{3.17}$$

Tarantola (2005) proposes to obtain the a-posteriori information combining the two states of information $\rho(\mathbf{d},\mathbf{m})$ and $\Theta(\mathbf{d},\mathbf{m})$; their combination is obtained through the conjunction (3.12) :

$$\sigma(\mathbf{d},\mathbf{m}) = k\frac{\rho(\mathbf{d},\mathbf{m})\cdot\Theta(\mathbf{d},\mathbf{m})}{\mu(\mathbf{d},\mathbf{m})} \tag{3.18}$$

with k normalization constant; $\sigma(\mathbf{d},\mathbf{m})$ represents the a-posteriori PDF in the $\mathbf{D}\times\mathbf{M}$ space.

The solution of the general inverse problem within this probabilistic framework is given by the a-posteriori PDF in the model space $\sigma_M(\mathbf{m})$; it is obtained from (3.18) by integration :

$$\sigma_M(\mathbf{m}) = \int_{\mathbf{D}} \sigma(\mathbf{d},\mathbf{m})d\mathbf{d} \tag{3.19}$$

3.2.1. The assumptions

The methodology we are proposing is based on the solution (3.19). It is evaluated assuming that both modelization and data uncertainties are

normally distributed. Using (3.16), modelization uncertainties are represented by the following PDF :

$$\theta(\mathbf{d}\,|\,\mathbf{m}) = \left((2\pi)^n \det \mathbf{C}_m\right)^{-1/2} \exp\left[-\frac{1}{2}(\mathbf{g}(\mathbf{m})-\mathbf{d})^T \mathbf{C}_m^{-1}(\mathbf{g}(\mathbf{m})-\mathbf{d})\right] \quad (3.20)$$

while data uncertainties, for an observation $\mathbf{d}_{obs}$, are represented by the a-priori PDF :

$$\rho_D(\mathbf{d}) = \left((2\pi)^n \det \mathbf{C}_d\right)^{-1/2} \exp\left[-\frac{1}{2}(\mathbf{d}-\mathbf{d}_{obs})^T \mathbf{C}_d^{-1}(\mathbf{d}-\mathbf{d}_{obs})\right] \quad (3.21)$$

with $\mathbf{C}_m$ the covariance matrix related to modelization uncertainties and $\mathbf{C}_d$ the covariance matrix related to measurement uncertainties.

Furthermore, we assume that there is no a-priori information in the model space :

$$\rho_M(\mathbf{m}) = \mu_M(\mathbf{m}) \quad (3.22)$$

Finally, since the data and model spaces are cartesian spaces, the homogeneous probability densities $\mu_M(\mathbf{m})$, $\mu_D(\mathbf{d})$ and consequently $\mu(\mathbf{d},\mathbf{m})$ are constant.

Under these hypotheses, the a-posteriori PDF (3.18) writes :

$$\sigma(\mathbf{d},\mathbf{m}) = k' \rho_D(\mathbf{d})\theta(\mathbf{d}\,|\,\mathbf{m}) \quad (3.23)$$

and the explicit solution for the inverse problem becomes :

$$\begin{aligned}
&\sigma_M(\mathbf{m}) = k' \int_{\mathbf{D}} \rho_D(\mathbf{d})\theta(\mathbf{d}\,|\,\mathbf{m})d\mathbf{d} = \\
&k'' \int_{\mathbf{D}} \left\{ \exp\left[-\frac{1}{2}(\mathbf{d}-\mathbf{d}_{obs})^T \mathbf{C}_d^{-1}(\mathbf{d}-\mathbf{d}_{obs})\right] \cdot \right. \\
&\left. \exp\left[-\frac{1}{2}(\mathbf{g}(\mathbf{m})-\mathbf{d})^T \mathbf{C}_m^{-1}(\mathbf{g}(\mathbf{m})-\mathbf{d})\right] \right\} d\mathbf{d} = \\
&k'' \exp\left[-\frac{1}{2}(\mathbf{g}(\mathbf{m})-\mathbf{d}_{obs})^T \left(\mathbf{C}_d^{-1}+\mathbf{C}_m^{-1}\right)(\mathbf{g}(\mathbf{m})-\mathbf{d}_{obs})\right]
\end{aligned} \quad (3.24)$$

Here $k^{'}, k^{''}$ are normalization constants; under Gaussian assumption, observation and modelization uncertainties are combined by adding the inverses of the covariance matrices.

We can rearrange (3.24) as follows :

$$\sigma_M(\mathbf{m}) = K\left((2\pi)^n \det \mathbf{C}_D\right)^{-1/2} \exp\left(-S(\mathbf{m}, \mathbf{d}_{obs})\right) \tag{3.25}$$

Where $\mathbf{C}_D \equiv \mathbf{C}_d + \mathbf{C}_m$ and

$$S(\mathbf{m}, \mathbf{d}_{obs}) \equiv \frac{1}{2}\left(\mathbf{g}(\mathbf{m}) - \mathbf{d}_{obs}\right)^T \mathbf{C}_D^{-1}(\mathbf{g}(\mathbf{m}) - \mathbf{d}_{obs}) \tag{3.26}$$

is the cost function and K is a normalization constant.

Usually, the function

$$L(\mathbf{m}, \mathbf{d}_{obs}) = \left((2\pi)^n \det \mathbf{C}_D\right)^{-1/2} \exp\left(-S(\mathbf{m}, \mathbf{d}_{obs})\right) \tag{3.27}$$

is referred to as likelihood function.

Within this approach the best model $\mathbf{m}^*$ is the value that maximizes the PDF $\sigma_M(\mathbf{m})$; however, we can also integrate $\sigma_M(\mathbf{m})$ to infer statistical indicators, such as the mean value of the distribution, the standard deviation and the correlation coefficients.

We assume that the covariance matrix is diagonal and it has the form $\mathbf{C}_D = \mathbf{1} \cdot MSE$, where $MSE = \sum_{i=1}^{n} \frac{\left[(d_{obs})_i - g_i(\mathbf{m}^*)\right]^2}{n-1}$. Under this assumption maximization of the likelihood function also corresponds to the minimization of the L^2 distance between data and predictions, $S'(\mathbf{m}, \mathbf{d}_{obs}) = \left(\mathbf{g}(\mathbf{m}) - \mathbf{d}_{obs}\right)^T (\mathbf{g}(\mathbf{m}) - \mathbf{d}_{obs})$, which does not depend on the *MSE* and can be computed independently of the knowledge of the solution $\mathbf{m}^*$**.** In the following application on real data we found *a-posteriori* that the MSE is in the range 0.01-0.03. The data uncertainties are associated to the S/N ratio. For S/N ratio > 10 on average in the selected frequency range, thus, the

contribution of the noise to the *MSE* is at least one order of magnitude smaller. Thus, the *MSE* is dominated within this range of S/N values by the modelization uncertainties and is retrieved to be independent of the specific S/N value.

3.3. Solution of the inverse problem

The solution of the inverse problem is computed in two steps: we first compute the minimum of the cost function $S'(\mathbf{m}, \mathbf{d}_{obs})$, using the Basin-Hopping technique, as described in the next section, then we evaluate the *MSE*, which is used for the estimation of the *a-posteriori* PDF $\sigma_M(\mathbf{m})$. Finally, the estimation of the uncertainties requires the integration of $\sigma_M(\mathbf{m})$.

If the forward operator $\mathbf{g}(\mathbf{m})$ is linear, $S(\mathbf{m}, \mathbf{d}_{obs})$ is quadratic and $\sigma_M(\mathbf{m})$ is normal (Gauss, 1809); the more nonlinear $\mathbf{g}(\mathbf{m})$, the farther $\sigma_M(\mathbf{m})$ from a Gaussian PDF. However, though strongly non-linear, the forward operator $\mathbf{g}(\mathbf{m})$ can be linearized in the vicinity of the best model, in a subdomain $\mathbf{M}^*$ centered around $\mathbf{m}^*$. We define $\mathbf{M}^*$ as the hypercube $\mathbf{M}^* = I_{m_1} \times .. \times I_{m_h}$, where I_{m_i} is a 1D interval containing the value m_i^*. If the value of $\sigma_M(\mathbf{m})$ is enough small outside $\mathbf{M}^*$, to not significantly contribute to the marginal PDFs related to the single parameters, we can extract the mean and the variance for each parameter, and the correlation coefficients for all couples of parameters, limiting the exploration to the domain $\mathbf{M}^*$.

Let us define the marginal PDF for the parameter m_i as $\hat{\sigma}_M(m_i) = \int_{\mathbf{M}_i^*} \sigma_M(\mathbf{m}) d\mathbf{m}$, and the marginal PDF for the couple (m_i, m_j) as $\breve{\sigma}_M(m_i, m_j) = \int_{\mathbf{M}_{ij}^*} \sigma_M(\mathbf{m}) d\mathbf{m}$,

where $\mathbf{M}_i^* = I_{m_1} \times .. \times I_{m_i-1} \times I_{m_i+1} \times .. \times I_{m_h}$ is the hypercube built accounting for all the parameters except m_i and $\mathbf{M}_{ij}^*$ the hypercube built excluding the parameters m_i and m_j.

Mean value, variance and correlation are finally computed as:

$$\begin{aligned} \mu_i &= \int_{\mathbf{M}^* \setminus \mathbf{M}_i^*} m_i \cdot \hat{\sigma}_M(m_i) dm_i \\ \sigma_i^2 &= \int_{\mathbf{M}^* \setminus \mathbf{M}_i^*} (m_i - \mu_i)^2 \cdot \hat{\sigma}_M(m_i) dm_i \\ \mathrm{cov}_{i,j} &= \int_{\mathbf{M}^* \setminus \mathbf{M}_{ij}^*} (m_i - \mu_i)(m_j - \mu_j) \cdot \breve{\sigma}_M(m_i, m_j) dm_i dm_j \end{aligned} \tag{3.28}$$

3.4. The Basin-Hopping algorithm for the search of the global minimum

The search for the minimum of the cost function $S'(\mathbf{m}, \mathbf{d}_{obs})$ is performed through the global optimization technique of the Basin-Hopping (BH) (Wales and Doye, 1997; Wales, 2003). The BH algorithm uses a random sampling of the model space, based on a Markov chain with a transition probability given by the Metropolis criterion.

Here we shortly summarize the searching strategy of the technique. If after j iterations the exploration has reached the point $\mathbf{m}_j$, at the (j+1)-th iteration a random perturbation of the coordinates is performed, moving the model in the point $\mathbf{m}_{j+1}^{(0)}$; this latter is considered as the starting point for a local minimization, which brings the exploration in the point $\mathbf{m}_{j+1}$. The minimization is performed using the Broyden–Fletcher–Goldfarb–Shanno (BFGS) algorithm (Fletcher, 1987). The point $\mathbf{m}_{j+1}$ is then compared with $\mathbf{m}_j$. If the cost function at the end of the (j+1)-th iteration is smaller than the

cost function at the end of the *j*-th iteration, i.e. $S'(\mathbf{m}_{j+1}, \mathbf{d}_{obs}) < S'(\mathbf{m}_j, \mathbf{d}_{obs})$, the transition from $\mathbf{m}_j$ to $\mathbf{m}_{j+1}$ is accepted, else it is accepted with a probability $P_{trans}(\mathbf{m}_j, \mathbf{m}_{j+1})$ given by the Metropolis criterion : $P_{trans} = \exp\left(-\frac{S'(\mathbf{m}_{j+1}, \mathbf{d}_{obs}) - S'(\mathbf{m}_j, \mathbf{d}_{obs})}{T} \right)$, where the temperature T of the Metropolis scheme is fixed all along the exploration.

It is worth to note that the solution at the end of each iteration $\mathbf{m}_j$ comes from a local minimization process, speeding up the search for the final solution, while maintaining a constant temperature facilitates the hopping out of cost function basins which contain local minima.

The method is based on sole three parameters, allowing for simple tuning. The first one is related to the initial modulus of the random perturbation. The perturbation is assumed to be the same fraction β of the range of variability for all the parameters. If the exploration of the parameter m_i is constrained in the domain $(m_{i,\min}, m_{i,\max})$, the size of the initial perturbation is thus $\Delta m_{i,0} = \beta\left(m_{i,\max} - m_{i,\min} \right)$. It is worth to note that the magnitude of the perturbation dynamically changes during the exploration. It is based on the fraction of the transitions a_r from the point $\mathbf{m}_j$ to $\mathbf{m}_{j+1}$, evaluated every 50 iterations; if $a_r > 0.5$, β is increased dividing the previous value by 0.9; if $a_r < 0.5$, β is decreased multiplying it by 0.9. This condition allows to explore farther and farther regions when the solution does not move from the same location in the model space for many iterations.

The second parameter is the temperature *T* of the Metropolis criterion, which is chosen by balancing the ability to converge toward the final solution and the possibility to escape from a local minimum. Its magnitude order should be comparable with the average difference between the local minima, and

thus it requires preliminary investigation. Finally, the exploration stops when the maximum number of iterations n_{iter} is reached.

The tuning of the BH parameters is problem dependent. From synthetic tests on theoretical spectra (Section 3.7), we obtained convergence to the global minimum with $\beta = 0.1,\ n_{iter} = 10000$ and T of the order of the unity.

We tested the BH technique with two standard test functions; the Ackley function :

$$ack(x,y) = -20\exp\left[-0.2\sqrt{\frac{1}{2}\left(x^2+y^2\right)}\right] - \exp\left[\frac{1}{2}\left(\cos 2\pi x + \cos 2\pi y\right)\right] + 20 + e \tag{3.29}$$

and the three-hump camel function :

$$cam(x,y) = 2x^2 - 1.05x^4 + \frac{x^6}{6} + xy + y^2 \tag{3.30}$$

Both functions have a global minimum in $(0,0)$.

The Ackley function mainly tests the ability of the global optimization technique to avoid a very-large number of local minima. In the example of Figure 3.2 we see that starting the exploration from the point $(20,20)$, far away from the global minimum, the BH technique was able to converge to the global minimum within 10000 iterations.

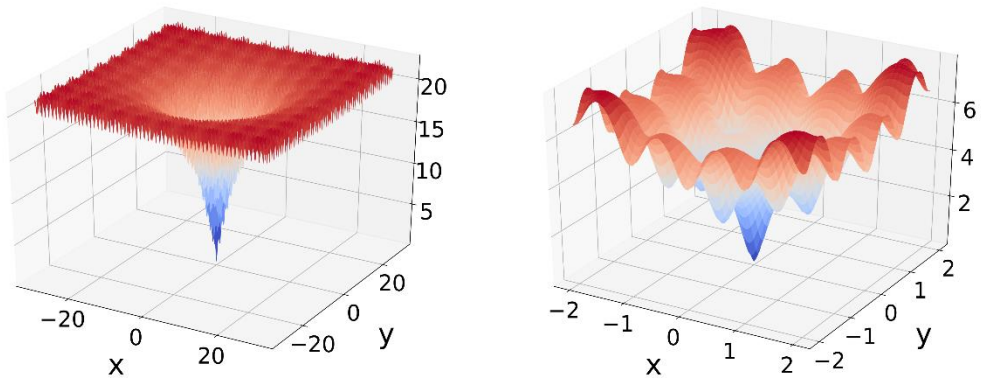

Figure 3.2 Ackley function. BH converges to the global minimum (0,0) starting from (20,20) within 10000 iterations.

The three-hump camel function is characterized by two minimum valleys in $\pm(1.5,1.5)$ where the value of the function is very close to the global minimum. Again in the example of Figure 3.3, starting the point $(20,20)$, the BH method was able to converge to the global minimum within 1000 iterations.

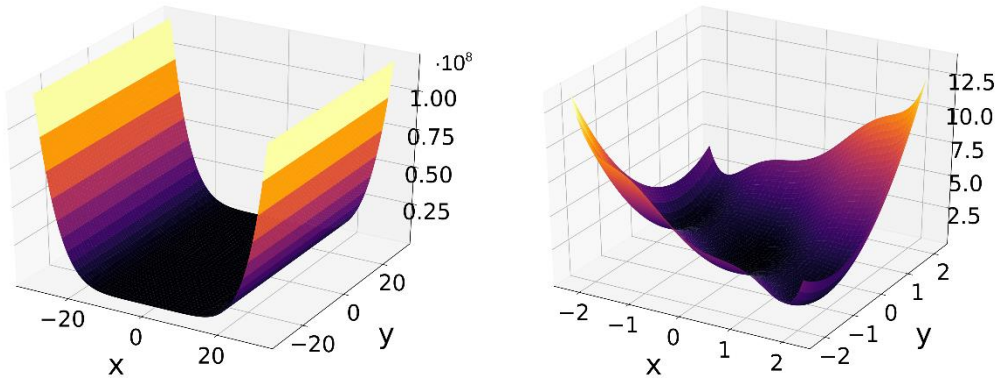

Figure 3.3 Three-hump camel function. BH converges to the global minimum (0,0) starting from (20,20) within 1000 iterations.

3.5. Parameters estimation : uncertainty and quality of the solution

The use of the joint PDF allows not only to seek for the best solution, but also to compute the uncertainties related to the best model, via integration of $\sigma_M(\mathbf{m})$. We cannot use the parameter space exploration from the BH technique, because it does not rely on a Monte Carlo sampling and thus, convergence of integrals is not guaranteed when increasing the iteration number. On the other hand, a complete description of $\sigma_M(\mathbf{m})$ in the whole parameter space is computationally expensive and, in many cases, unnecessary, since this function very often rapidly decreases to zero when

moving away from the maximum. For this reason, we limit the computation of the joint PDF in the hypercube $\mathbf{M}^*$ centered in the best fit model $\mathbf{m}^*$. For the definition of the hypercube we explore the 1D conditional distributions

$$\tilde{\sigma}_{M_i}(m_i) = \sigma_M(m_1^*,..,m_i,..,m_h^*) \quad i \in \{1,...,h\} \tag{3.31}$$

where all parameters are fixed to the value that they have in the global maximum of the PDF while the parameter m_i can vary. We then define the interval $I_i^* = [m_{i\text{down}}, m_{i\text{up}}]$, containing the value m_i^*, such that $\tilde{\sigma}_{M_i}(m_{i\text{down}}) \approx \tilde{\sigma}_{M_i}(m_{i\text{up}}) \approx 0.05\tilde{\sigma}_{M_i}(m_i^*)$. In the case in which the conditional PDF can be described by a Gaussian function, the interval I_i^* is symmetric around m_i^* and its length is four times the standard deviation of the Gaussian function. Since the marginal PDF has usually a larger standard deviation than the conditional PDF because of the correlations among parameters, we consider the enlarged interval $I_i = [\bar{m}_{i\text{down}}, \bar{m}_{i\text{up}}]$. $\bar{m}_{i\text{down}} = \max\left[m_{i\min}, (1-\lambda)m_i^* + \lambda m_{i\text{down}}\right]$ being $\lambda = 2.5$ the scaling factor between the marginal and the conditional PDF standard deviations; analogously $\bar{m}_{i\text{up}} = \min\left[m_{i\max}, (1-\lambda)m_i^* + \lambda m_{i\text{up}}\right]$. Finally, the domain $\mathbf{M}^*$ is obtained by tensorization : $\mathbf{M}^* = I_1 \times .. \times I_h$.

We can finally check *a-posteriori* the assumption of Gaussian uncertainties, evaluating the quality of the retrieved marginal PDFs $\hat{\sigma}_M(m_i)$ in terms of similarity with a normal distribution. As similarity criterion, we adopt the normalized cross-correlation function:

$$cc(\tau) = \int_{\mathbf{M}_i^*} \hat{\sigma}_M(m_i)\sigma_{\exp}(m_i + \tau)dm_i \tag{3.32}$$

where $\sigma_{\exp}(m_i) \equiv N(m_i; \mu_i, \sigma_i^2)$ is the expected, normal distribution having median μ_i and variance σ_i^2. We selected a quality threshold θ_σ; if the zero-

lag correlation $cc(0) \geq \vartheta_\sigma$, the solution is accepted. In our analysis we chose $\theta_\sigma = 0.95$.

3.6. Dataset features and final results expression

In the previous sections, we described how to retrieve source parameters from the inversion of a single spectrum. However, an earthquake is recorded at several stations, usually on the three components of a seismic instrument. For a single station, we invert for one spectrum for the P wave, obtained from the vertical component, and one spectrum for the S wave, obtained as the geometrical mean of the two spectra, computed on the horizontal components (Fletcher et al., 1984). When combining information from diverse stations we should be aware that each station provides a different image of the earthquake source, depending on the directivity, the radiation pattern and propagation effects. For that reason, we cannot consider each spectrum as a repeated measure of the same source parameters. After obtaining an estimation of the source parameter $(\mu_i)_k$ with uncertainty $(\sigma_i)_k$ from the inversion of a single spectrum at the *k*-th station, the final estimation of this parameter is given by the weighted mean

$$\bar{\mu}_i = \frac{\sum_{k=1}^{K} (\mu_i)_k (w_i)_k}{\sum_{k=1}^{K} (w_i)_k} \tag{3.33}$$

and the weighted uncertainty is given by

$$\bar{\sigma}_i = \sqrt{\frac{1}{\sum_{k=1}^{K} (w_i)_k}} \tag{3.34}$$

where $(w_i)_k = \frac{1}{(\sigma_i^2)_k}$ and K is the total number of stations contributing to the mean.

3.7. Synthetic tests

3.7.1. Large signal to noise ratio

As a first example we want to show the reliability of the method on a signal poorly affected by the noise. This example will also enable us to understand how the uncertainties are computed and what are the intrinsic correlations between couples of parameters. For the aim, we assume an exact knowledge of geometrical spreading, elastic properties and travel time of the wave (we assume ξ and $T^c(\mathbf{r},\mathbf{r}_0)$ known in (3.4)). We consider a theoretical Brune spectrum with the following parameters : $\log M_0 = 10$, $f_c = 10\,\text{Hz}$, $\gamma = 2$ and $Q = 100$. We then pollute the signal with noise, having a signal to noise ratio $R_{S/N}$ = 100. First, $R_{S/N}$ is defined in the time domain. Here the displacement u is the sum of the signal $s(t)$ and the noise $n(t)$: $u(t) = s(t) + n(t)$. The displacement amplitude spectrum can be written (see Appendix A) as $\log(\tilde{u}) \approx \log(\tilde{s}) + \frac{\tilde{n}}{\tilde{s}}\cos(\varphi_S - \varphi_N)$, where $\tilde{s}$ and $\tilde{n}$ are the amplitude spectra, ϕ_S and ϕ_N the phase spectra of the signal and the noise, respectively, and they are all a function of the frequency. The ratio $\frac{\tilde{n}}{\tilde{s}}$ scales as $\frac{1}{R_{S/N}}$ and at low frequencies, for a flat noise spectrum the ratio $\frac{\tilde{n}}{\tilde{s}} \sim \frac{1}{R_{S/N}}$. However, the noise spectrum is usually not flat in the displacement, but it decreases as a function of the frequency, as well as the source spectrum does, eventually with

different slopes. In addition, the noise spectrum is not uncoherent, but it presents peaks and holes related to ambient and site effects.

In these tests we impose the following perturbation on the Brune spectrum $\tilde{u}_{Brune}$ to account for the noise effect in the displacement:

$$\log \tilde{u} = \log \tilde{u}_{Brune} + \frac{1}{R_{S/N}} \sin\left(\cdot \frac{2\pi f}{f_N} \right) \cdot (1+\eta) \qquad (3.35)$$

The noise has a coherent contribution having a sinusoidal shape with amplitude equal to the reciprocal of the signal to noise ratio, modulated by a random contribution. Here we have $f_N = 1$ Hz and η a random variable over the interval $[-0.5, 0.5]$. The spectrum has been inverted in the frequency band [0.1 - 100] Hz.

Within this high value of the signal to noise ratio, the solution almost perfectly fits the initial spectrum (Figure 3.4, left panel).

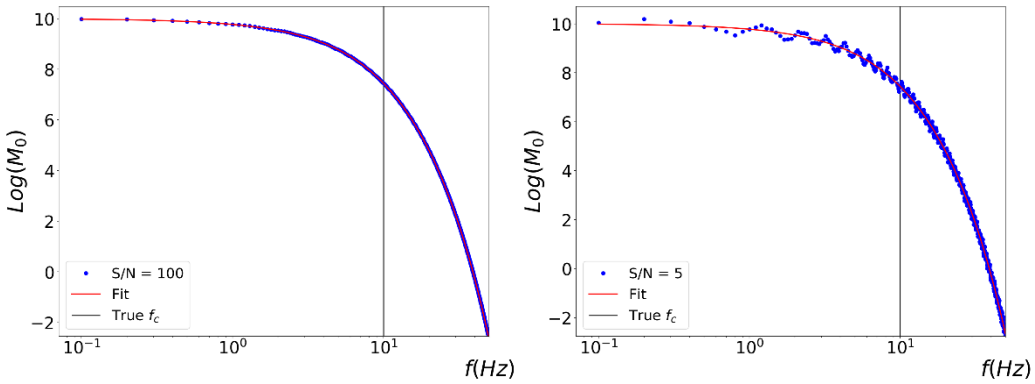

Figure 3.4 Synthetic spectrum (blue curve) and solution retrieved from the inverse problem (red curve, eq. (3.4)) for the case of $R_{S/N}$ = 100 (left panel) and $R_{S/N}$ = 5 (right panel).

The 1-D marginal PDFs are Gaussian distributions, centered on the values imposed to generate the synthetic spectrum (Figure 3.5). We have the following estimates for the source parameters: $\log M_0 = 10.000 \pm 0.004$, $f_c = 9.99 \pm 0.09$ Hz and $\gamma = 1.999 \pm 0.015$, and the final estimate for the quality

factor is $Q = 100.00 \pm 0.05$, whose uncertainty has been obtained by propagating the error on *Q*'. We have very small uncertainties on the seismic moment and the quality factor (<0.1%), while the uncertainty is about at 1% on both f_c and γ.

In Figure 3.6 we represent the 2-D marginal PDFs as heatmaps. Since the data uncertainty is negligible in this case, the maps represent the intrinsic correlation among the parameters. This correlation is due to the modelization uncertainty, and cannot be reduced. The absolute value of all the correlation coefficients is above 0.6; larger (anti-)correlations can be found between f_c and $\log M_0$, γ and Q', with values close to -1. These large correlations provide a support for the selection of the factor λ, used to define the exploration interval for the computation of the marginal PDFs from the conditional PDFs (Section 3.5).

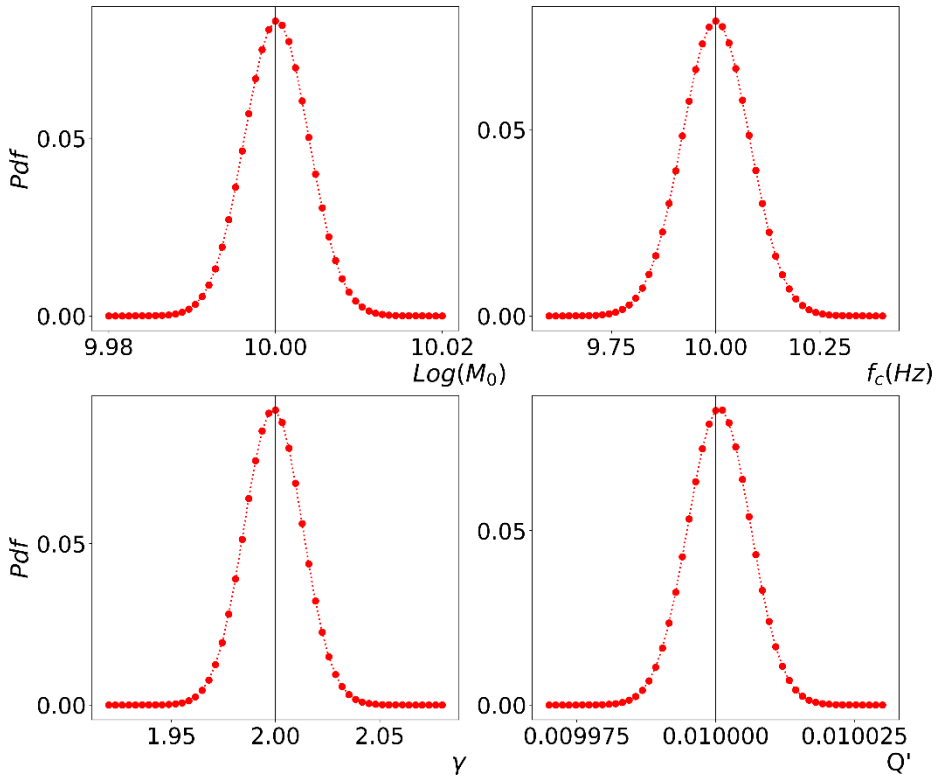

Figure 3.5 1-D marginal PDFs computed for a $R_{S/N}$ = 100. In the four panels the PDF are represented for log(M_0), f_c, γ and Q'. The black vertical line is the true value of the parameter. All the distributions show a Gaussian-like behavior.

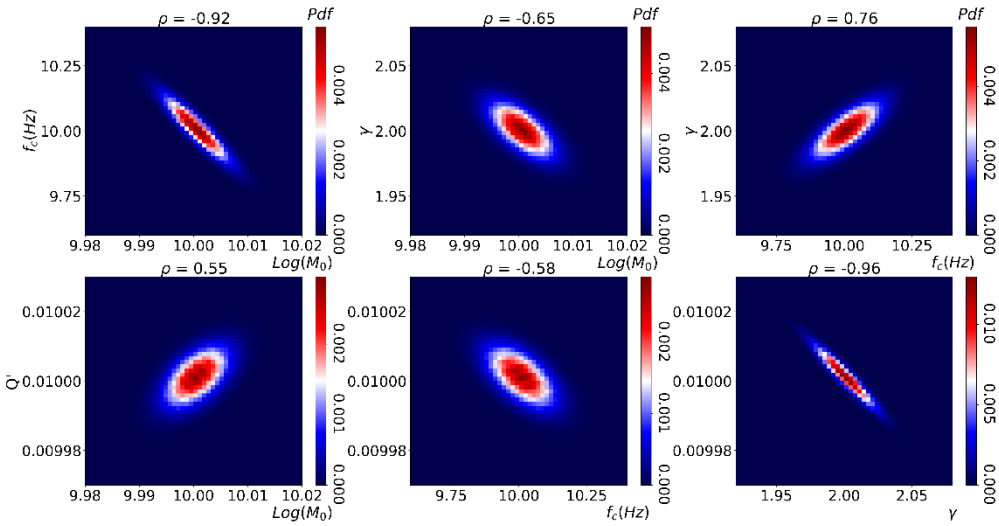

Figure 3.6 2-D marginal PDFs (heatmaps) computed for a $R_{S/N}$ = 100. Correlation coefficients are at the top of each heatmap. We see that large anticorrelations occur for the couples log(M_0)-f_c, and γ- Q', with correlation coefficients close to -1.

3.7.2. Signal to noise ratio $R_{S/N}$ = 5

We perform a test similar to the previous example, with the synthetic spectrum to be retrieved having the same parameters as above and polluted with the same functional perturbation. In this case we use a smaller signal to noise ratio ($R_{S/N}$ = 5), this value being representative of the average $R_{S/N}$ value in the analyzed datasets of tectonic earthquakes. The spectrum is inverted in the same frequency band of [0.1 - 100] Hz. In Figure 3.4 (right panel) we represent the comparison between the retrieved solution and the original spectrum. We still retrieve the final parameters but in this case the uncertainties are larger. The final estimates are $\log M_0 = 10.01 \pm 0.08$, $f_c = 9.7 \pm 1.7$ Hz, $\gamma = 1.9 \pm 0.3$ and $Q = 99.7 \pm 1.1$. Although the smallest uncertainties are still retrieved for the seismic moment and the quality factor, now they have increased to 0.8% and 1.1% respectively. The percentage error is increased to 18% on f_c and to 16% on γ. In Figure 3.7 we compare the marginal distributions for this case with the case of $R_{S/N}$ = 100, on the same

scale. The distributions still maintain their Gaussian shape, but their width is significantly increased. It is very interesting to note that, on the contrary, correlation coefficients do not change significantly (Figure 3.8) : thus, correlation among parameters is mostly due to the modelization uncertainty, and the effect of data uncertainty on it is negligible.

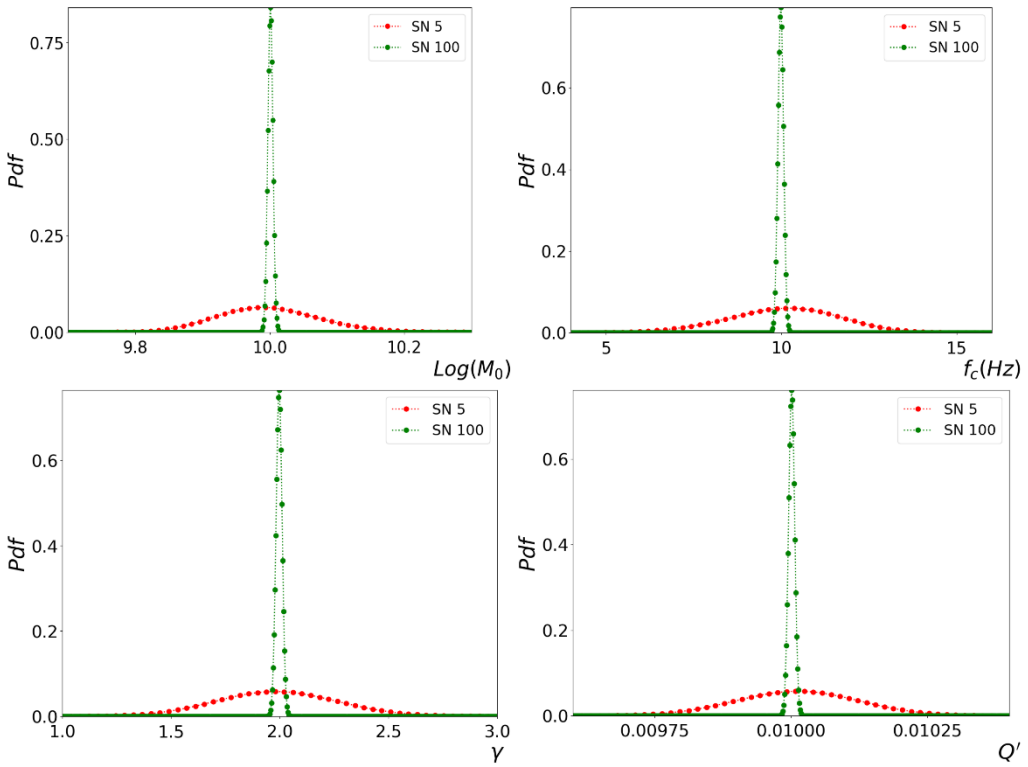

Figure 3.7 Comparison between 1-D marginal PDFs solutions, for $R_{S/N}$ = 100 (green curve) and $R_{S/N}$ = 5 (red curve).

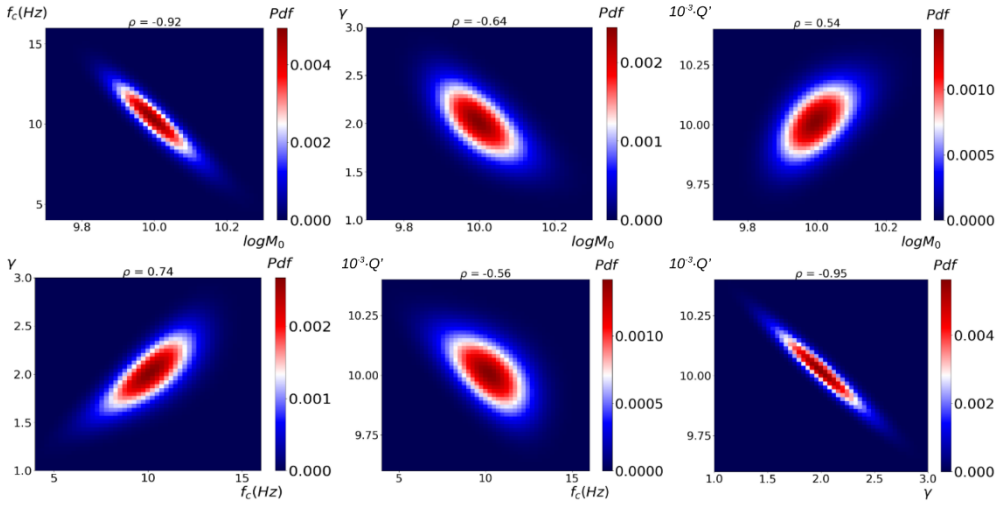

Figure 3.8 2-D marginal PDFs (heatmaps) computed for a $R_{S/N}$ = 5. Correlation coefficients are at the top of each heatmap; both the shape and correlation coefficients do not significantly change as compared to the case of a $R_{S/N}$ = 100 (Figure 3.6).

3.7.3. Frequency bandwidth for the inversion

The resolution of the source parameters and of the quality factor depends on the bandwidth in the frequency domain available for the inversion. In the previous examples the bandwidth for the inversion is enough large, with two decades before the corner frequency and one decade after it, to allow the proper resolution of the parameters. We want to investigate how the resolution degrades when we shrink the bandwidth around the corner frequency. We use the same parametrization of the synthetic spectrum as in the previous examples and we use a value of $R_{S/N}$ = 5. We analyze the reduction of the bandwidth with three different approaches: we reduce the band at frequencies larger than f_c (case 1), smaller than f_c (case 2) and symmetrically around f_c (case 3). The results are shown in Figure 3.9, panels A, B and C respectively. In the Figure we represent the relative difference between the expected and the retrieved values, for all the parameters. In all cases, when we reduce the band, the uncertainty increases and eventually a bias in the estimation of two or more parameters can emerge because of the

unresolved correlations. In Figure 3.9-A we can observe that the parameters are well resolved down to a frequency band as large as 0.4 decade. The seismic moment and the quality factor are almost unsensitive to the reduction of the high-frequency band, while the uncertainty in both f_c and γ significantly increases as the bandwidth decreases. The correlations start to be poorly resolved at a width of 0.4 decade after the corner frequency. The mean value of all the parameters is less sensitive to the reduction of the bandwidth at the left of the corner frequency. Still larger errors arise from the correlation between f_c and γ but with mean values well constrained down to a 0.1 decade. When a symmetric restriction is performed the quality of the solution is controlled by the high-frequency region and again we need a bandwidth of 0.4 decade to have proper resolution on the parameters. Finally, in Figure 3.10 we show the heatmaps of the correlation between Q' and f_c for a symmetric bandwidth size of 0.3 decade and 0.4 decade around the corner frequency. When reducing the bandwidth, we see a migration of the maximum of the marginal PDF toward the upper limit of the explored frequency band, with the smoother decay of the spectrum around f_c being instead explained through a slightly lower Q value.

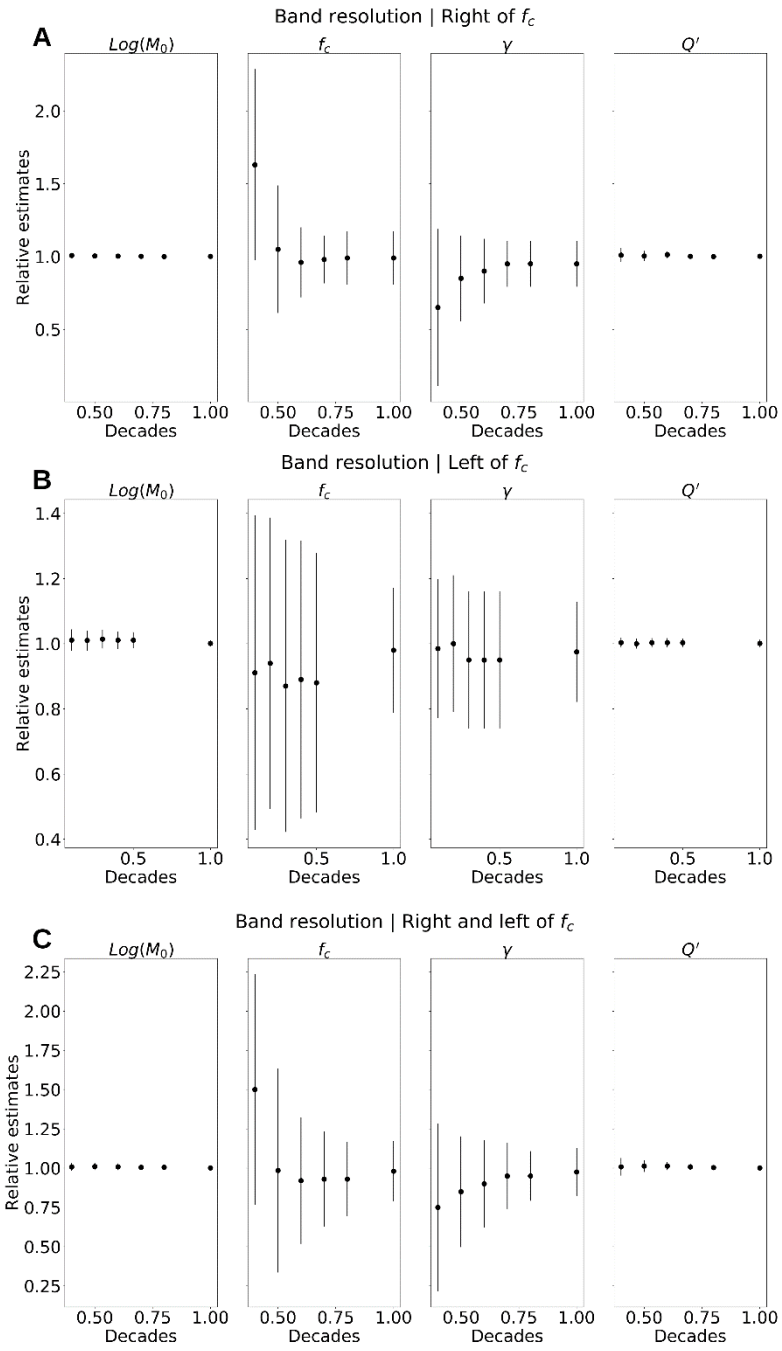

Figure 3.9 Difference between the expected and the retrieved values for the parameters $\log(M_0)$, f_c, γ and Q' as a function of the frequency bandwidth used for the inversion. Panels A, B and C corresponds to a change in the bandwidth from 0.4 to 1 decade to the right of f_c, to the left of f_c and symmetrically around f_c, respectively.

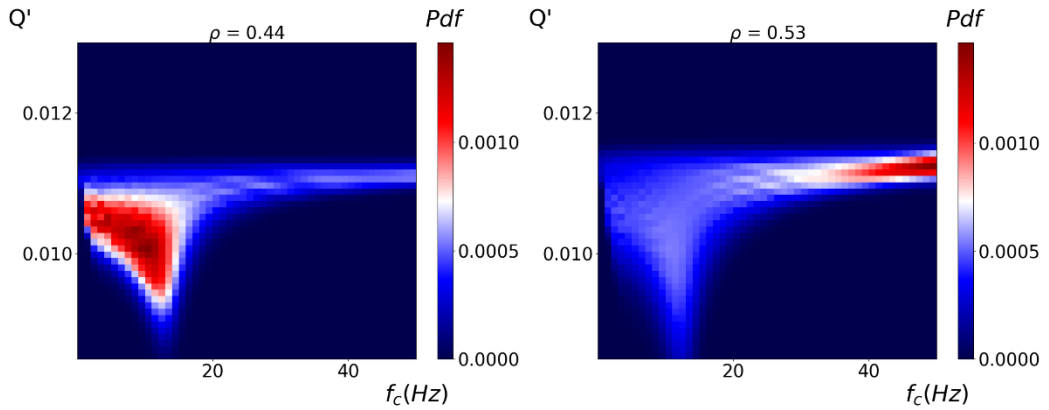

Figure 3.10 2-D marginal PDFs (heatmaps) for the parameters f_c and Q'. In the left panel we represent the solution obtained using a bandwidth of 0.4 decade on the two sides of the corner frequency; in the right panel we show the solution with a bandwidth of 0.3 decade. We see that the maximum of the PDF migrates in the right panel to the upper limit of the explored f_c range, far from the true value Q' = 0.1, f_c = 10 Hz.

3.7.4. Uncertainties variations for different Q factors

The accuracy in the quality factor estimate depends on the value of *Q* itself: the smaller *Q,* the more relevant its effect on the spectrum. We see that the uncertainty on the *Q* estimate increases as *Q* increases. As an example, we consider the solutions for *Q* = 100 and *Q* = 800 obtained from a theoretical spectrum inverted in the same frequency band, symmetric around *fc* with 0.4 decade available on the two sides of the corner frequency. The percentage error moves from 5 % to 37 %, with the estimates for the quality factor of $Q = 98 \pm 5$ and $Q = 680 \pm 250$, respectively. However, the change in the *Q* value does not affect significantly the accuracy and the quality of the solutions for the other parameters.

4. 2016-2017 Central Italy earthquakes

4.1. Data

A major earthquake sequence interested the Central Italy region from August, 2016 to January, 2017. The first event of the sequence, the $M_w = 6.0$ Amatrice earthquake occurred on August 24, 2016 with epicenter in the village of Accumoli; it was a very-high impact event; it caused 298 casualties, more than 17000 displaced persons and it completely destroyed several villages. The largest earthquake of the sequence – the $M_w = 6.5$, Norcia earthquake - occurred on October 30, 2016 with epicenter in the village of Norcia. It generated large slip at the surface, with a maximum amplitude observed on the Monte Vettore of about 2 m.

We computed the source parameters for the major events of this sequence. The dataset consists of accelerometric records for all the events of the sequence with $M_L \geq 4.0$ (56 events), recorded by stations within 100 km from the event epicenter. We have at maximum 62 stations per event (Figure 4.1); the minimum hypocentral distance is equal to 9 Km, the maximum is equal to 100 Km. The total number of records is 2329.

Sampling frequency varies among 100 Hz, 125 Hz and 200 Hz, depending on the station.

The waveforms were downloaded from ESM (Engineering Strong-Motion database) (Luzi et al., 2016); the metadata were acquired from INGV bulletin (ISIDe working group, 2016).

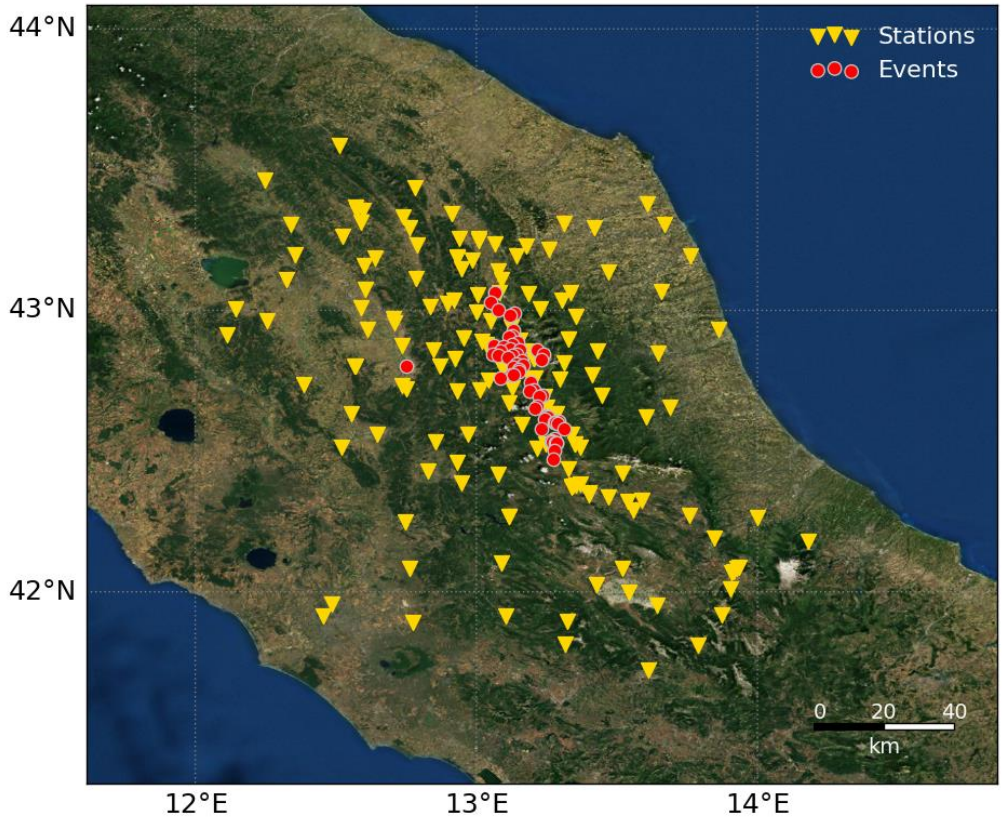

Figure 4.1 Map representing the location of the events (red dots) and stations (yellow triangles).

4.2. Processing

For each record, the definition of the S-wave (signal) duration Δt was based of the expected ground motion duration (Trifunac and Brady, 1975):

$$\Delta t = \frac{0.02 \cdot \exp(0.74 \cdot M_L) + 0.3 \cdot \delta_H}{a} \tag{4.1}$$

where δ_H is the hypocentral distance and $a = 2$ is a factor introduced to rescale the ground motion duration to the S-wave duration. The S-wave time-window ΔT_S was therefore defined using a theoretical S-wave arrival time T_S obtained from a 1-D velocity model (Chiarabba, 2009):

$$\Delta T_S = \left[T_S - 0.1 \cdot \Delta t, T_S + 0.9 \cdot \Delta t\right] \tag{4.2}$$

To be sure to include the direct S wave, the time window starts before the theoretical expected arrival; specifically, it anticipates the S wave arrival time of a time equal to the 10% of the expected duration.

A noise time-window ΔT_N of the same duration Δt was selected before the origin time T_0 :

$$\Delta T_N = [T_0 - \Delta t, T_0] \tag{4.3}$$

With this choice, we do not want to include the P-wave within the noise window. Although the P wave coda may pollute the S wave signal, the direct P wave does not usually perturb the S waveform. Indeed, using the P wave as noise to be compared to the S signal artificially amplifies the noise contribution.

The following operation were performed on both signal and noise waveforms:

1. Constant and linear trend removal
2. Hann-function tapering on the first and last 5 % of the signal; the first half of the window is applied to the first 5% of the signal, the second half to the last 5 %.

Fast Fourier Transform (Cooley and Tukey, 1965) was computed for pre-processed signal and noise, obtaining the amplitude spectra. Finally, each spectrum has been smoothed with a 5-points moving average filter.

4.2.1. Quality control on automatic processing

Automatic processing of large dataset could be very dangerous.

In order to avoid to blindly mix in the processing data with very different quality, we defined two quality selection criteria. The first-one is based on the signal-to-noise ratio, evaluated point by point in the frequency domain; the

second-one is based on the similarity of each a-posteriori probability density function to a Gaussian function as discussed in the Section 3.5.

4.2.1.1. Signal-to-noise ratio quality selection

We computed the signal-to-noise ratio for each point of the frequency domain $\left(0\,\text{Hz} - 0.8 \cdot f_{NYQUIST}\right)$; starting from the center of the domain, we looked for the first (left direction) and the last (right direction) point with S/N larger than 1.25. These 2 points become the bounds of the a-posteriori frequency domain, used for the fit. As a result, this allowed us to reject the frequency subdomain in which the noise was comparable to the signal (Figure 4.2). Moreover, we were able to automatically reject records that carried no information about the earthquake (Figure 4.3) when an empty frequency band was selected.

4.2.1.2. Solution quality selection

One of the assumptions of the probabilistic approach is that modelization uncertainties are Gaussian-like functions. If the forward operator we are using is not able to properly describe the observed data, this assumption does not hold anymore. As a consequence, the a-posteriori pdf (3.25) is no longer similar to a Gaussian function.

In order to reject the data for which this similarity does not hold, we evaluated the similarity of each solution to a Gaussian function (Section 3.5). An example is shown in Figure 4.4.

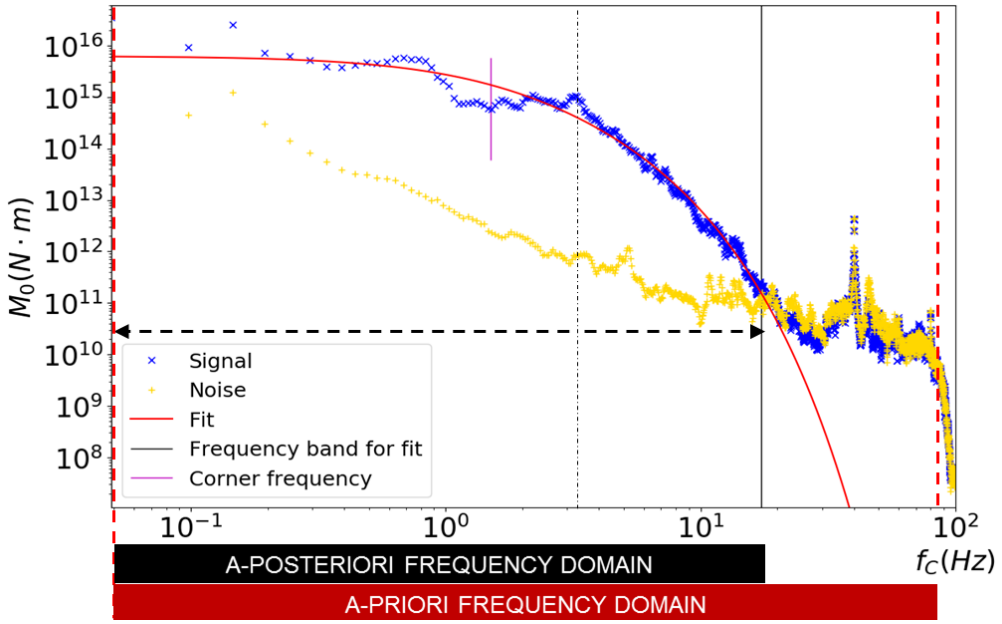

Figure 4.2 A-priori (red rectangle) and a-posteriori (black rectangle) frequency band for the spectrum fit (red curve). The blue curve is the signal spectrum, the yellow curve is the noise spectrum; there is a clear effect of the noise spectrum (change of decay slope beyond 20 Hz) that we are able to avoid thanks to the signal-to-noise ratio criterion.

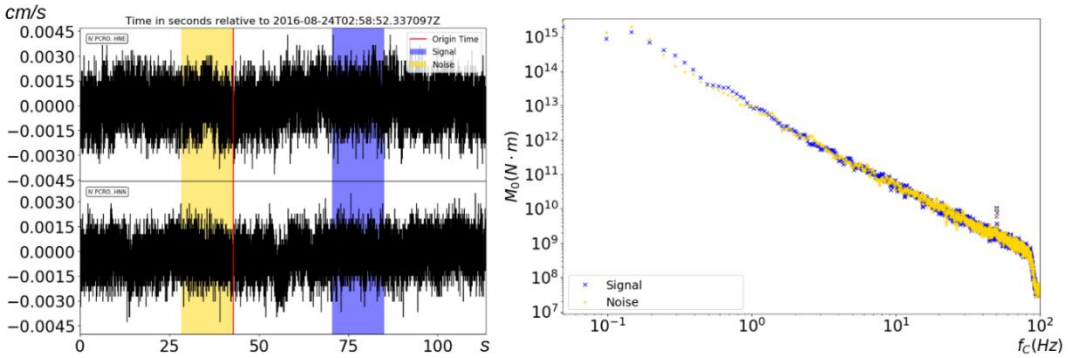

Figure 4.3 Rejected data (Event-ID INGV 7077321, station PCRO) due to the signal-to-noise ratio criterion. On the left, the noise (yellow window) and the signal (blue window); on the right, the noise (blue curve) and the signal (yellow curve) spectrum.

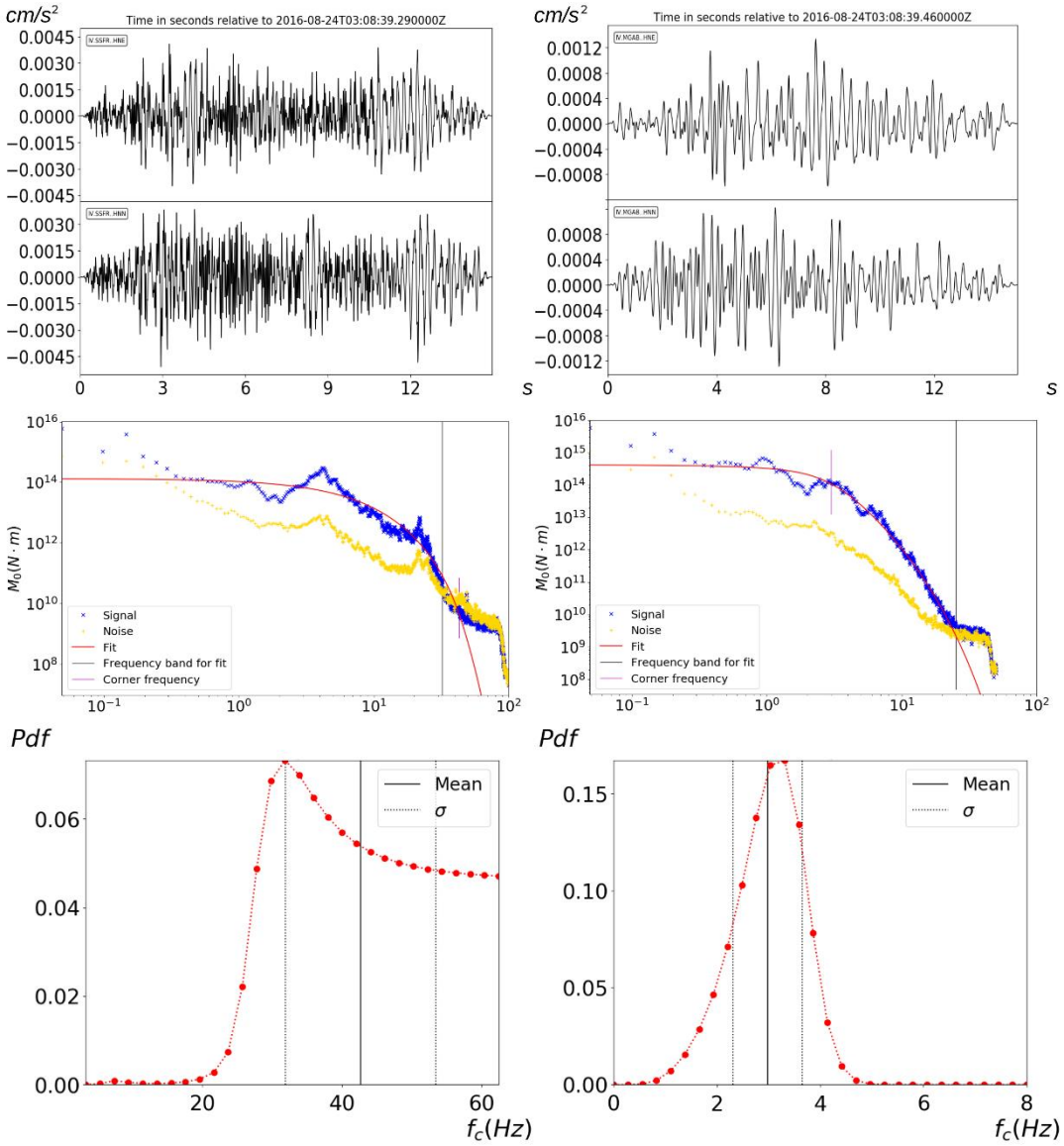

Figure 4.4 Rejected data due to the gaussian similarity criterion for the solution (Event ID-INGV 7077781). The rejected data (upper left, station SSFR) is very different from the S-wave observed at other stations for the same event (upper right, station MBGAB).
Each column, from the top : rejected signal; signal spectrum(blue curve), noise spectrum (yellow curve) and fit (red curve); 1-D marginal PDF for f_c.

4.3. Results

We investigated the earthquake source properties for the main events of the Central Italy 2016-2017 sequence. As an example, we show the solution for the $M_L = 4.0$ event occurred the day 24-08-2016 at 23:22:05 (UTC) (Event 7141891), and recorded at the station FIAM. Observed signals in time and frequency domains are shown in Figure 4.5. The fit is superimposed to the amplitude spectrum of the waveform. 1-D marginal PDFs are shown in Figure 4.6; 2-D marginal PDFs heatmaps are plotted in Figure 4.7, while a comparison with the modelization correlation (Section 3.7.1) is shown in Figure 4.8. It is worth noting that, as observed from synthetic tests, the correlation is governed by the modelization uncertainty.

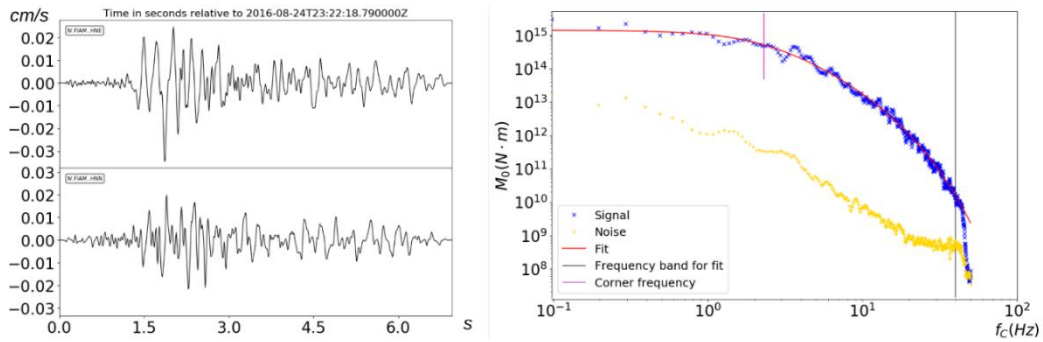

Figure 4.5 An example of accepted solution. In the left panel we plot the 2 horizontal components of the signal; in the right panel we represent the signal spectrum (blue curve), the noise spectrum (gray curve) and the best-fit solution (red curve). The traces are shown for the event ID-INGV 7141891 and the station FIAM.

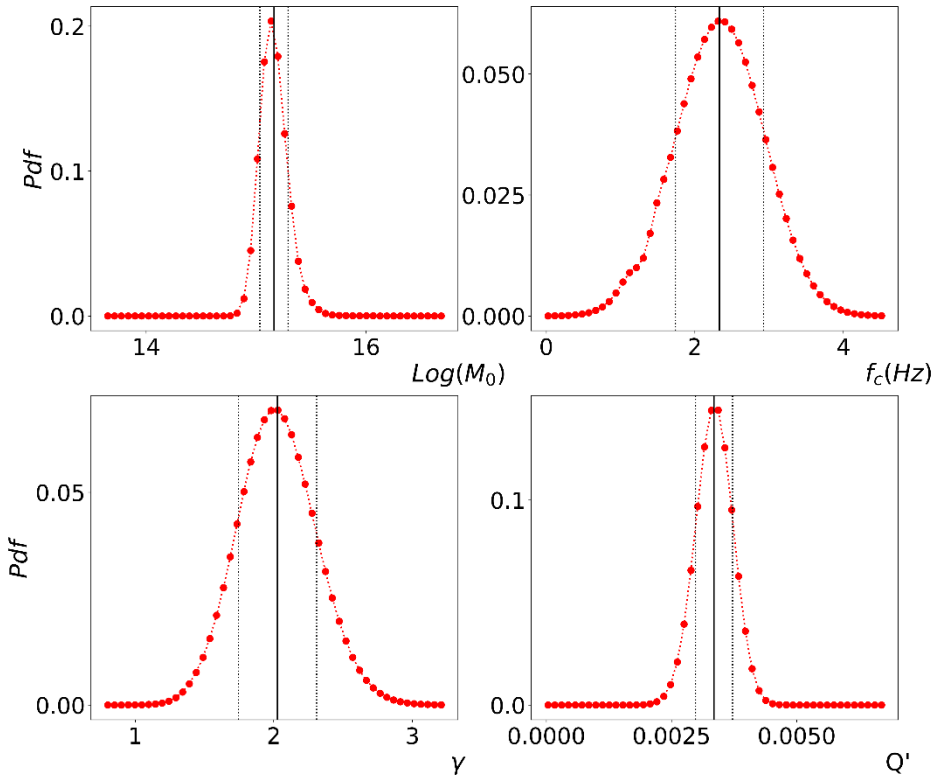

Figure 4.6 1-D marginal PDFs for the parameters log(M_0), f_c, γ and Q'. All the curves show a Gaussian-like behavior for the same event-station as shown in Figure 4.5.

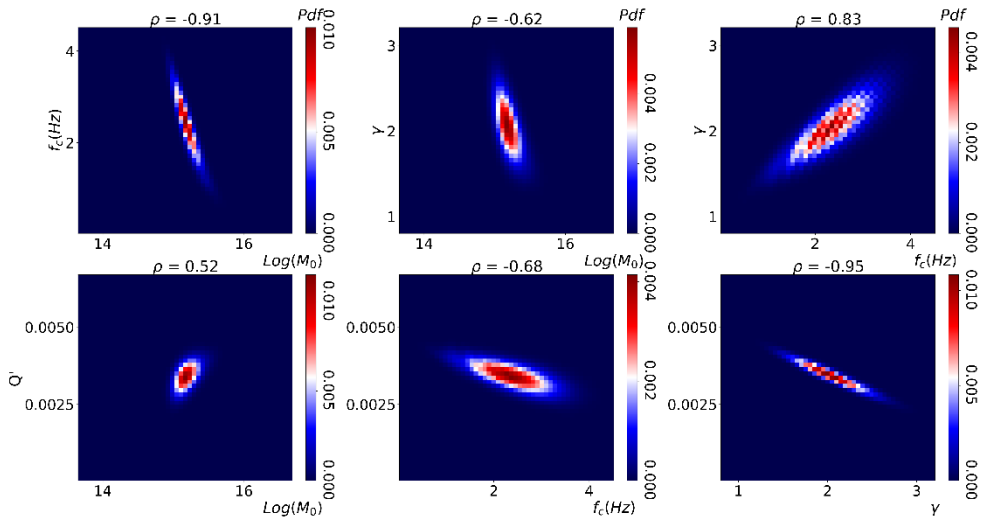

Figure 4.7 2-D marginal PDFs for the parameters log(M_0), f_c, γ and Q', for the same event-station as shown in Figure 4.5. These heatmaps look similar to the theoretical ones of Figure 3.6, indicating that correlations are mainly driven by model uncertainties.2-D marginal PDFs.

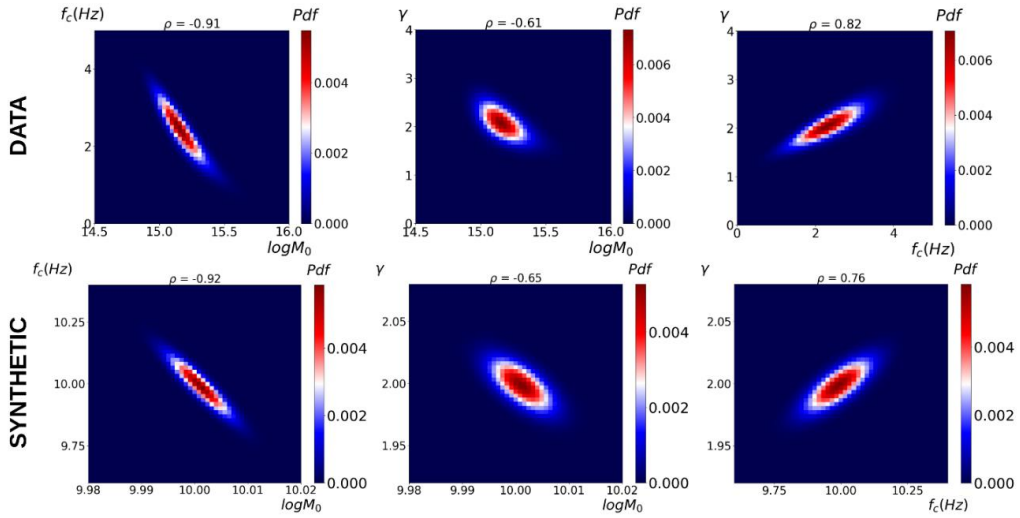

Figure 4.8 Comparison among expected and observed correlation for source parameters. On the top, 2-D marginal PDFs for the event 7141891, station FIAM; on the bottom, 2-D marginal PDFs from synthetic spectrum with S/N = 100 (Section 3.7.1).

In Figure 4.9 we represent the solutions for all the events, in the plot of the corner frequency as a function of the seismic moment. We observe on average that standard scaling $M_0 \propto \frac{1}{f_c^3}$ holds (Aki, 1967) with an average static stress drop $\Delta\sigma = 2.1 \pm 0.3$ MPa, although we have a large variability in the corner frequency estimates for events with similar seismic moment. Specifically, for event with moment magnitude M_W between 4 and 5 a variability in the corner frequency of a factor 5, with the stress drop jumping from few hundreds KPa to 10 MPa. However, the majority of events has a stress drop close to the average values. As the magnitude increases the stress drop increases. For the Norcia event ($M_W = 6.4 \pm 0.1$), we have a corner frequency $f_c = 0.15 \pm 0.03\ Hz$ and a high-frequency decay slope $\gamma = 2.14 \pm 0.08$. The estimated source radius is $r = 8.3 \pm 1.8\ km$ and the static stress drop is $\Delta\sigma = 4 \pm 3\ MPa$. For the Amatrice event, we have a moment magnitude of

$M_W = 6.11 \pm 0.07$, a corner frequency $f_c = 0.27 \pm 0.04\ Hz$ and a high-frequency decay slope $\gamma = 2.05 \pm 0.08$. The estimated source radius is $r = 4.5 \pm 0.7\ km$, the static stress drop is $\Delta\sigma = 9 \pm 4\ MPa$. Finally, for the Visso earthquake, we have a moment magnitude of $M_W = 5.93 \pm 0.05$, a corner frequency $f_c = 0.23 \pm 0.03\ Hz$ and a high-frequency decay slope $\gamma = 1.94 \pm 0.04$. The estimated source radius is $r = 5.3 \pm 0.6\ km$, the static stress drop is $\Delta\sigma = 3.0 \pm 1.0\ MPa$.

To analyze the stress drop retrieved in this study, we compare our findings with scaling relationships of the two major seismic sequences, that have interested the Central Italy region (Umbria-Marche 1997-1998, L'Aquila 2009) in the last two decades. Different studies for this events show a stress drop characterization fully consistent with our results : Bindi et al. (2004) found an average stress drop of 2 ± 1 MPa for the Umbria-Marche sequence; For L'Aquila sequence Pacor et al. (2015) showed a stress drop variability that spans two order of magnitude $(0.1 - 25)$ MPa, with an average value equal to 2.6 MPa, and a higher value - 10 MPa - for the largest event ($M_W = 5.8$). They also observed a stress drop increase from 1 to 10 MPa with the moment magnitude ranging from 3 to 5.8. Also Del Gaudio et al. (2015) reanalyzed the source parameters for some events of the L'Aquila sequence, to extract appropriate empirical Green functions for numerical simulations. They also found a self-similarity in the selected dataset, including events with magnitude ranging between 3.5 and 6.3, with an average stress drop of 3 MPa. The mainshock of the sequence instead showed a higher stress drop of about 9.0 MPa.

All the reported stress drop estimations are consistent among each other and with our estimations, since they are obtained assuming the Brune's circular rupture model.

As in the previous studies we also have a larger stress drop than the average for the largest magnitude events in the sequence. This may be an indication of slip concentration in smaller size patches, as also retrieved from kinematic inversions (Tinti et al., 2016; Liu et al., 2017; Chiaraluce et al., 2017). In the case of the M 6.0, Amatrice earthquake Chiaraluce et al. (2017) retrieved a small size slip patch ($3x3\,Km^2$) with a maximum slip larger than 1 m, just up-dip with respect to the hypocenter and a secondary slip patch of about $5x5$ Km^2, with slip above 50 cm. On the rest of the fault ($\sim 20x15$ Km^2) the slip level is lower (< 30 cm).

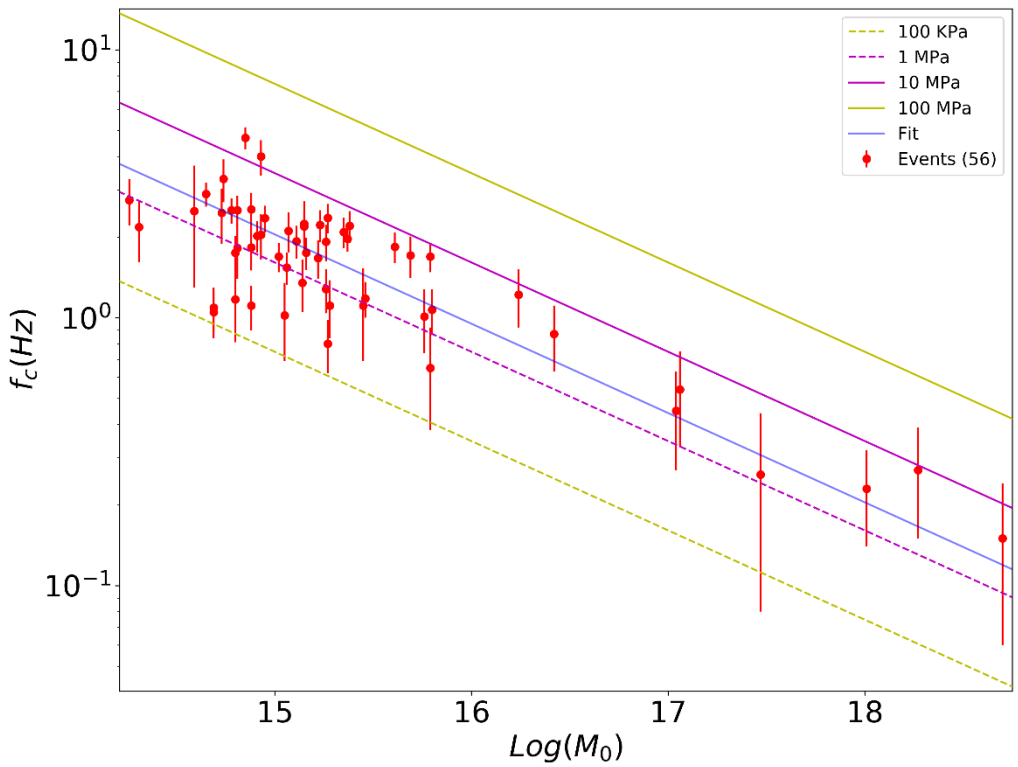

Figure 4.9 Scaling law between the corner frequency and the seismic moment. The red points are the solutions per event; the blue line is the best fit curve, with a scaling of -3; the parallel lines indicate the scaling with stress drops ranging from $\Delta\sigma = 0.1 MPa$ to $\Delta\sigma = 100\,MPa$. The error bars are represented with a $3\,\sigma$ confidence level.

Results for γ and Q are shown in Figure 4.10 and Figure 4.11. The γ distribution has a median value equal to 2.1, with the 60 % of events

exhibiting a γ between 1.9. and 2.3 as expected from the standard Brune's model (Brune, 1970, Section 2.4.1). In this case, retrieved high-frequency scaling could be an indication of standard mechanisms for earthquake generation, mainly driven by tectonic stress perturbed by the occurrence of previously events (static and dynamic triggering).

The Q distribution has a mean value of 230, and a standard deviation of 50; this can be interpreted as a mean value for the anelastic attenuation factor of the whole explored region. It is consistent - at a confidence level of 2 σ - with the estimate of Bindi et al. (2004). They found an average S wave anelastic attenuation factor of 318 for the Central Italy region; it is worth to note that they used a different Green's function with a frequency-dependent Q factor and a constant Q value was found only for frequencies above 8 *Hz*.

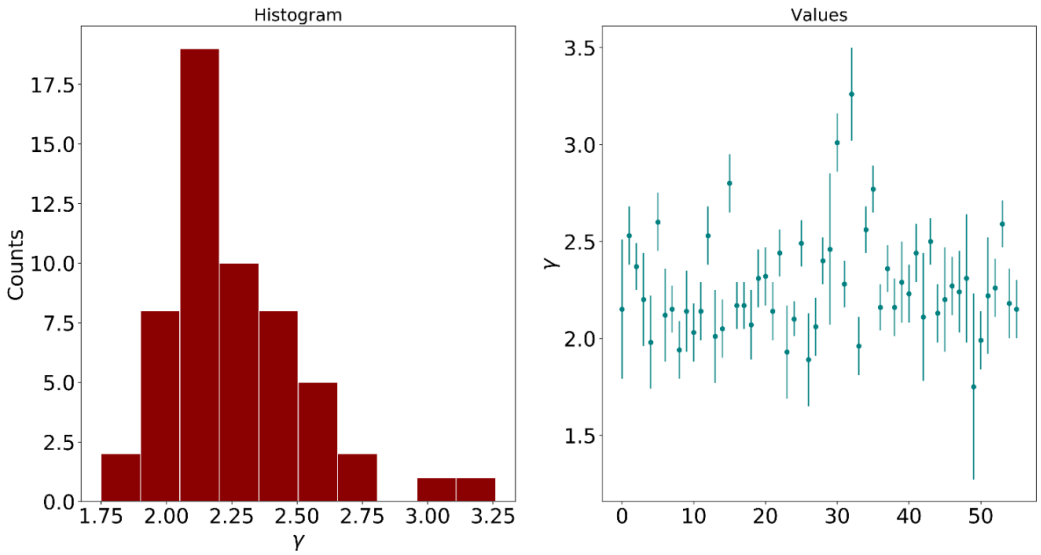

Figure 4.10 γ estimates per single events. In the left panel we plot the histogram for the parameter and in the right panel the retrieved values per event. The error bars are represented with a 3 σ confidence level.

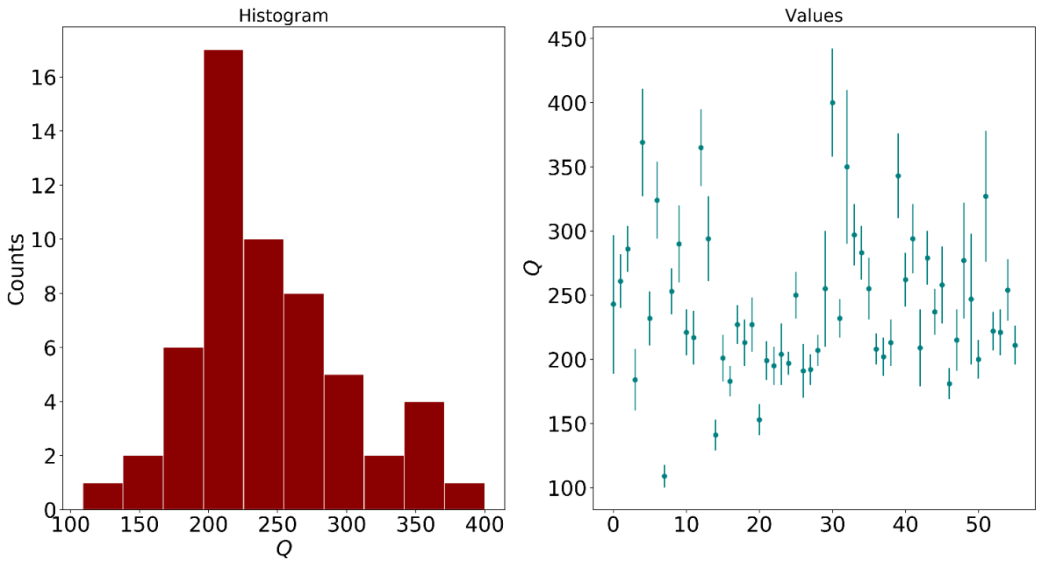

Figure 4.11 Q estimates per single events. In the left panel we plot the histogram for the parameter and in the right panel the retrieved values per event. The error bars are represented with a 3σ confidence level.

5. LFEs in Nankai

Low-frequency earthquakes (LFEs) (Nishide et al., 2000) are a peculiar seismic activity manifestation, characterized by low amplitude, very low signal-to-noise ratio and a frequency content mostly included in the 1-10 Hz band. LFEs are part of a more general phenomenon called *slow earthquakes*; it comprehends *nonvolcanic tremor* (Obara, 2002), *slow-slip events* (SSE) (Dragert et al., 2001) and *very low-frequency earthquakes* (VLFs) (Ito et al., 2007). Two common features distinguish these events from ordinary earthquakes : the longer time duration and the frequency content.

With the exception of very few cases (Kanamori and Cipar, 1974; Linde et al., 1996), a systematic observation of these phenomena was possible only after the recent deployment of dense and highly sensitive seismic networks, such as the NIED Hi-Net (Obara et al., 2005).

Slow earthquakes always occur close to the source area of very-large earthquakes (megathrust earthquakes). The scientific interest in the study of these phenomena is therefore high : they could play a fundamental role in the control and preparation of large seismic events; thus a detailed characterization of the events would help in improving the seismic hazard, mitigating the associated risk. Furthermore, the 1-10 Hz frequency band is relevant for seismic engineering in the study of the stability of several kinds of structures.

In the last years, several complex data analysis methods have been developed in order to enhance the detection of LFEs (Brown et al., 2008; Frank and Shapiro, 2014; Poiata et al., 2016); consequently, very-large datasets are available to the scientific community. Nevertheless, the source characterization of these phenomena still remains unknown; the main difficulty is represented by the very-low signal-to-noise ratio associated with this seismic transient. Ide et al. (2007) and Bostock et al. (2015) observed

two opposite behaviors concerning the scaling of the source duration with the seismic moment. The former study includes all the available slow earthquakes at the time of the publication and shows a seismic moment proportional to the duration (Figure 5.1); the latter study, specifically related to LFEs along the Cascadia subduction plate, retrieves an almost constant duration over two decades of seismic moments. Both results are completely different from what has been largely observed for ordinary earthquakes (Aki, 1967), where the seismic moment is proportional to the cube of the duration.

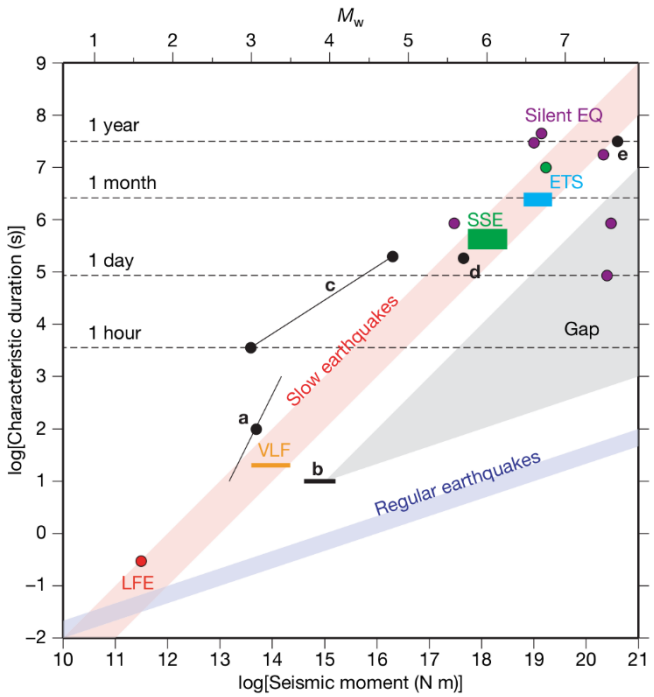

Figure 5.1 Scaling among seismic moment and duration for various slow earthquakes, and comparison with ordinary earthquakes scaling. Figure from Ide et al., 2007.

In this work, we applied the previously described method to characterize the source of more than 40000 LFEs occurred in the Nankai region during the period 2012-2016.

5.1. Data

The dataset is composed by 43183 LFEs detected by applying the BTBB technique (Poiata et al., 2016) to nonvolcanic tremors recorded in southwestern Japan by the dense high-sensitive Hi-net monitoring system (Obara, 2005) during the period 2012-2016. Along this period 100 Hz continuous velocity records were available from 25 stations.

The BTBB technique consists in a multi-scale array-based detection; using characteristic functions extracted from the seismic signals, it detects and locates the events by back-projecting the station-pair time-delay estimates according to theoretical time-delays, and by exploiting coherence across the stations.

The distribution of the events in space and time is represented in Figure 5.2 and Figure 5.3, respectively.

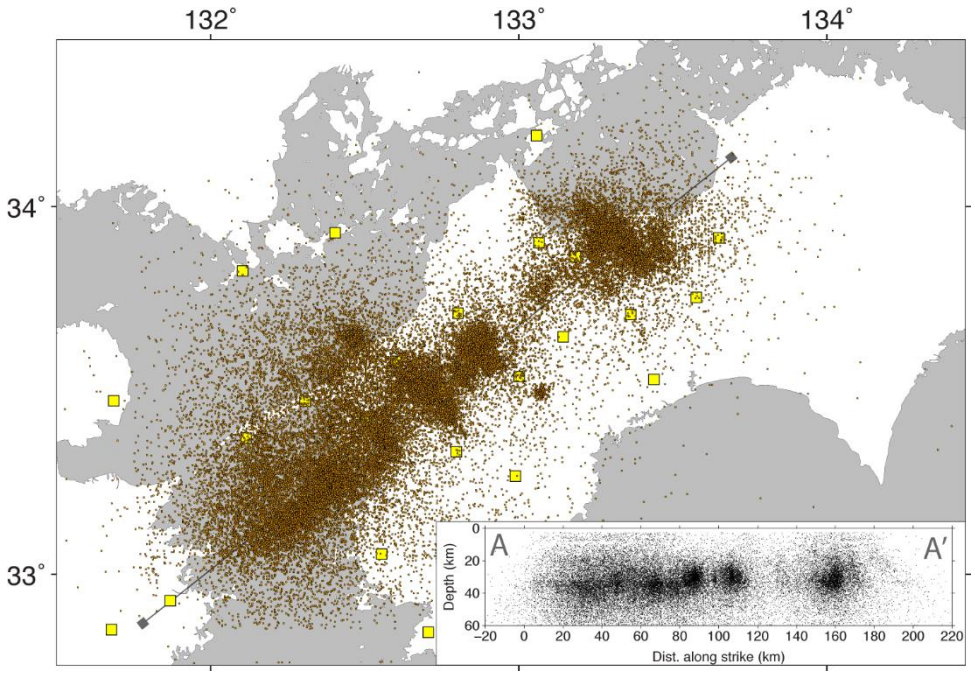

Figure 5.2 Map representing the location of the LFEs (brown dots) and stations (yellow squares).

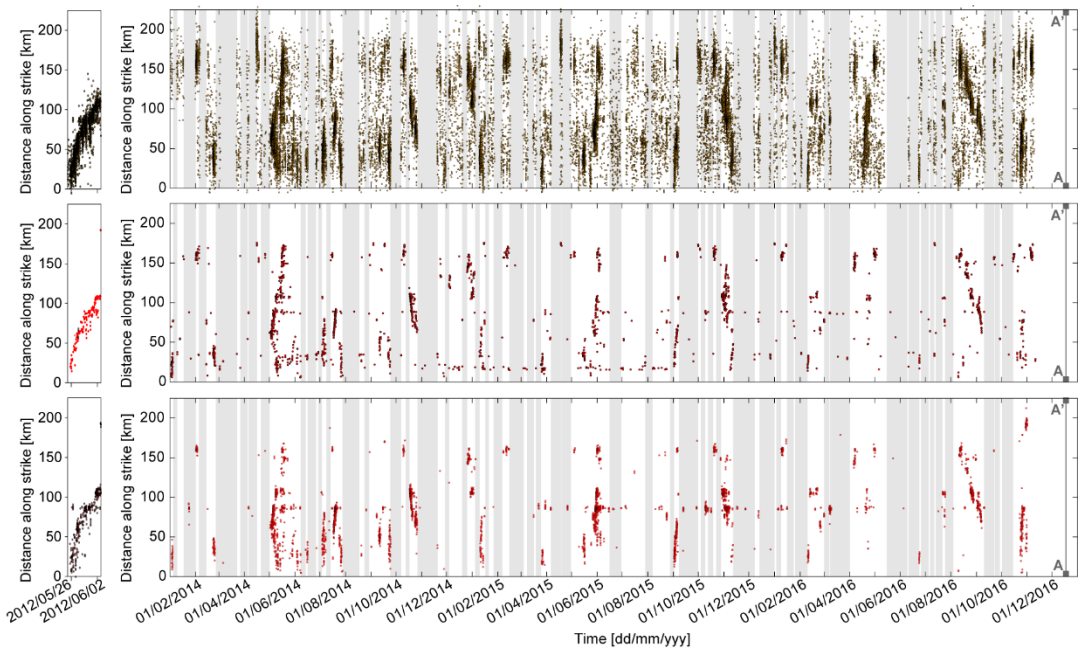

Figure 5.3 Time distribution of the LFEs : on the top, BTBB catalog; in the middle, NIED catalog; on the bottom, JMA catalog.

5.2. Processing

We applied the described methodology to S-wave displacement spectra. S-wave arrival times T_S were theoretically obtained from the 1-D layered velocity model of Kubo et al. (2002).

Following the criterion defined in Section 4.2, a 4 seconds S-wave time window ΔT_S was selected as follows :

$$\Delta T_S = \left[T_S - 0.4, T_S + 3.6\right] \tag{5.1}$$

A noise time-window ΔT_N of the same duration was selected before the origin time T_0 :

$$\Delta T_N = \left[T_0 - 4, T_0\right] \tag{5.2}$$

The following operations were then performed on both signal and noise records:

3. Constant and linear trend removal
4. Hann-function tapering on the first and last 5 % of the data

Fast Fourier Transform (Cooley and Tukey, 1965) was computed for pre-processed signal and noise, obtaining the amplitude spectra. Finally, each spectrum has been smoothed with a 5-points moving average filter.
For each LFE and each station, the observed curve is the geometric mean of the smoothed spectra from the 2 horizontal components.

5.2.1. Quality control on automatic processing

We applied the same quality criteria as described previously (Section 4.2.1), and based on the signal-to-noise ratio, and degree of similarity of the a-posteriori PDF to a Gaussian function.

5.2.1.1. Signal-to-noise ratio quality selection

We computed the S/N for each point of the frequency domain $[0.7-40]$ Hz, where the maximum frequency was selected as the 80 % of the Nyquist frequency, while the minimum frequency is due to the instrument response function; the response is flat above 1 Hz, but when removing the instrument response from the records by deconvolution, the domain can be further extended to 0.7 Hz.
Starting from the center of the interval, we looked for the first (left direction) and the last (right direction) point with S/N larger than 1.25. These 2 points become the bounds of the a-posteriori frequency domain, used for the fit. As a result, this allowed us to exclude from the fitting the frequency subdomain in which the effect of the noise was comparable to the signal (Figure 5.4). Moreover, we were able to automatically reject records with no information

about the earthquake (Figure 5.5), when an empty frequency band was obtained at the end of this phase. This happened for more than 50 % of the available records.

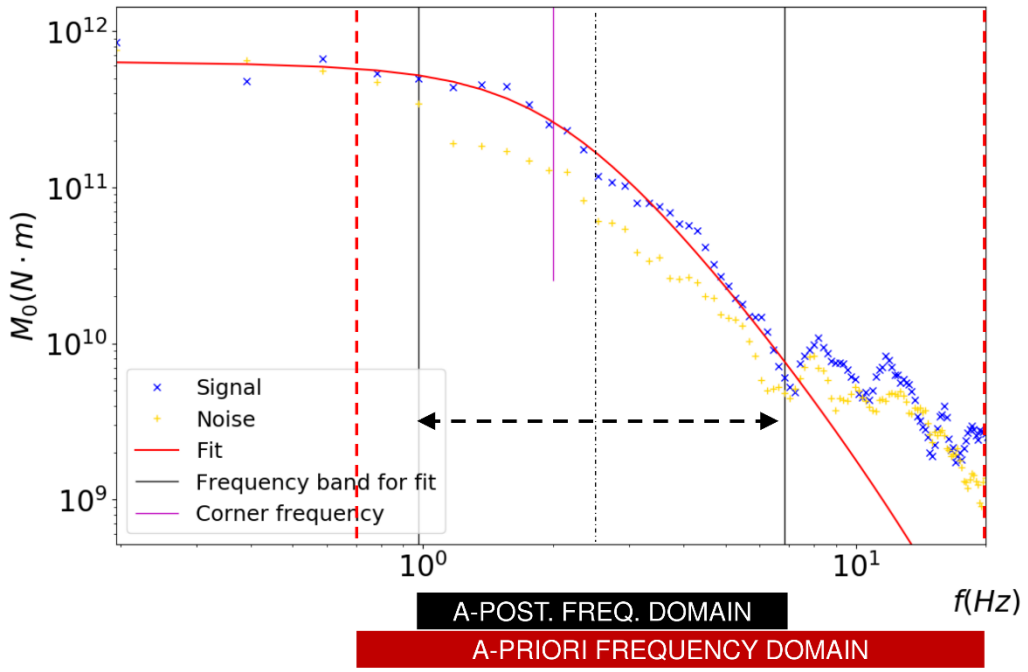

Figure 5.4 A-priori (red rectangle) and a-posteriori (black rectangle) frequency band for the spectrum fit (red curve). The blue curve is the signal spectrum, the yellow curve is the noise spectrum; there is a clear effect of the noise spectrum (change of decay slope beyond 7 Hz) that we are able to avoid thanks to the signal-to-noise ratio criterion. To better visualize the effect of the criterion, the a-priori frequency domain has been cut up to 20 Hz.

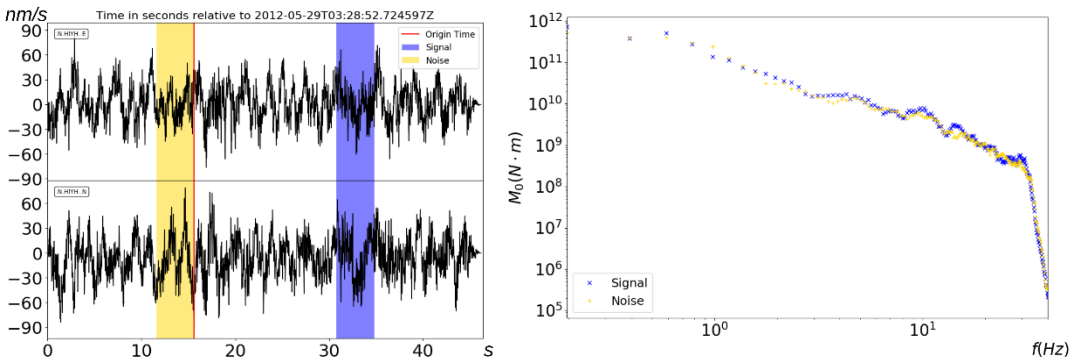

Figure 5.5 Rejected data (Event-ID 20120529_0329D, station N.HIYH) due to the signal-to-noise ratio criterion. On the left, the noise (yellow window) and the signal (blue window); on the right, the noise (blue curve) and the signal (yellow curve) spectrum.

5.2.1.2. Solution quality selection

Since our probabilistic framework is based on the assumption that modelization uncertainties are Gaussian, we verify the similarity of the a-posteriori PDF (3.25) to a Gaussian function (Section 3.5).

As an example of rejected data, we show (Figure 5.6, left column) an ordinary earthquake waveform contained in the dataset, with a corner frequency f_c beyond the data resolution; this event was rejected after processing. The PDF for f_c is clearly different from a Gaussian distribution, and indicates that the true corner frequency is in a frequency domain beyond 40 Hz, which is the maximum data resolution. Indeed, for an ordinary earthquake with a seismic moment equal to $10^{11.7}$ N m the expected corner frequency – assuming a stress drop $\Delta\sigma = 10$ MPa – is ~ 50 Hz. With this criterion, we were able to reject all the ordinary earthquakes contained in the dataset.

Moreover, we show (Figure 5.6, right column) a LFE signal with a very low quality (low signal-to-noise ratio); the S/N criterion described in the previous section is able to individuate a frequency band in which there could be an information different from the noise; this band is very narrow ($[0.8 - 3.0]$ Hz) due to the low quality of the data and from a visual inspection of the spectrum is easy to understand that it is different from the expected displacement spectrum that we want to model (Section 2.3). However, an automatic processing of this signal would lead to an estimation of the source parameters for this station; thanks to this criterion, we were able to reject all the signals characterized by such a low quality.

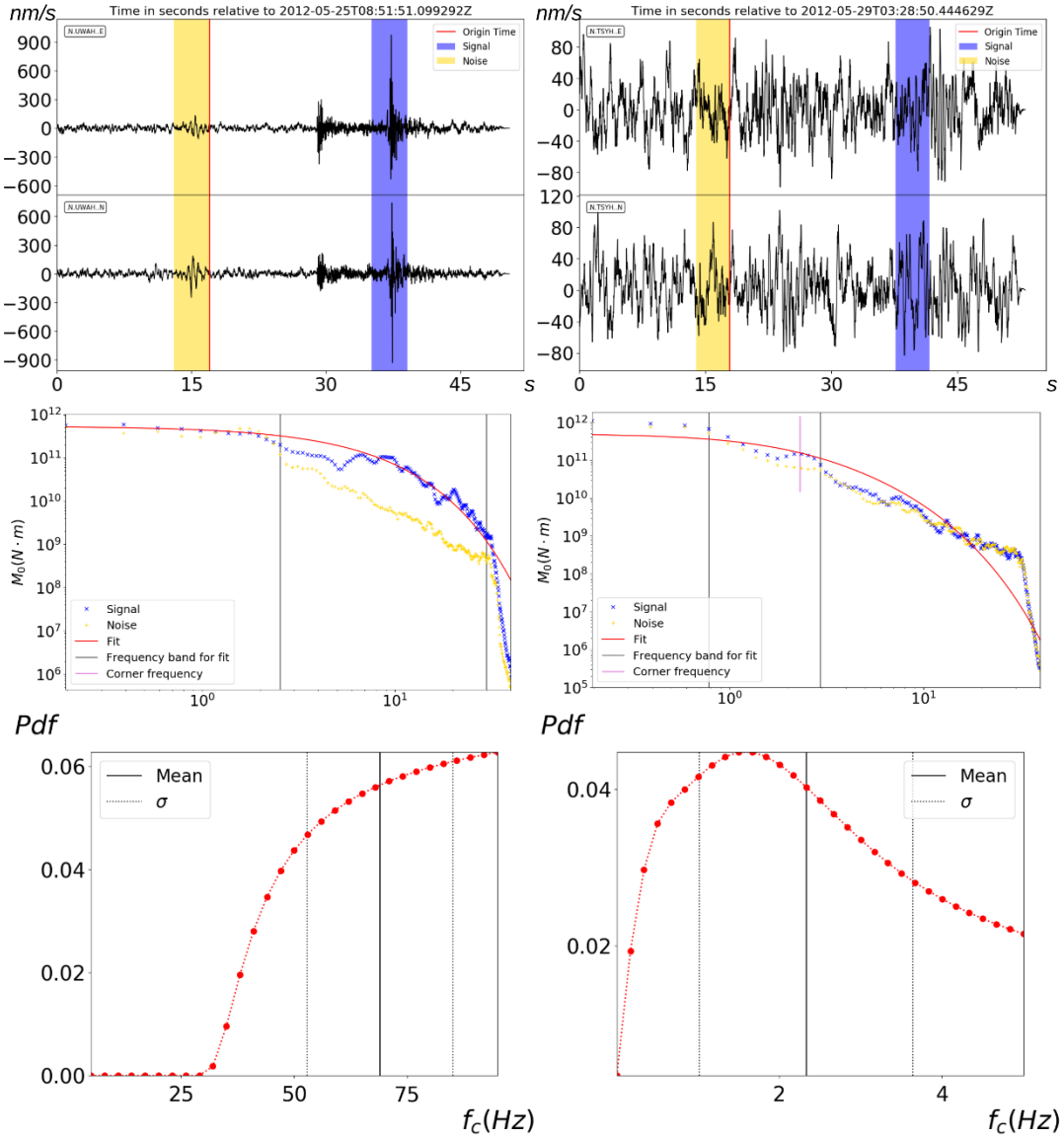

Figure 5.6 Examples of rejected solutions. Left column : signal (blue window) and noise (yellow window) (top), signal (blue curve) and noise (yellow curve) spectrum (middle), corner frequency PDF (bottom) for an ordinary earthquake contained in the dataset (Event 20120525_0852C, station N.UWAH). Right column : signal, spectrum and corner frequency PDF for a low quality data (Event 20120529_0329D, station N.TSYH).

5.3. Results

We analyzed the dataset inverting for the three source parameters $(\log M_0, f_c, \gamma)$, while the Q-factor was fixed to the value $Q = 300$ from literature (Kubo et al., 2002).

We estimated the source parameters for 11076 LFEs (Figure 5.7); the seismic moment of the events varies in the interval $\log M_0 = [10.4 - 12.4]$ ($M_W = [0.86 - 2.2]$), while the corner frequency spans the interval $f_c = [0.8 - 12]$ Hz.

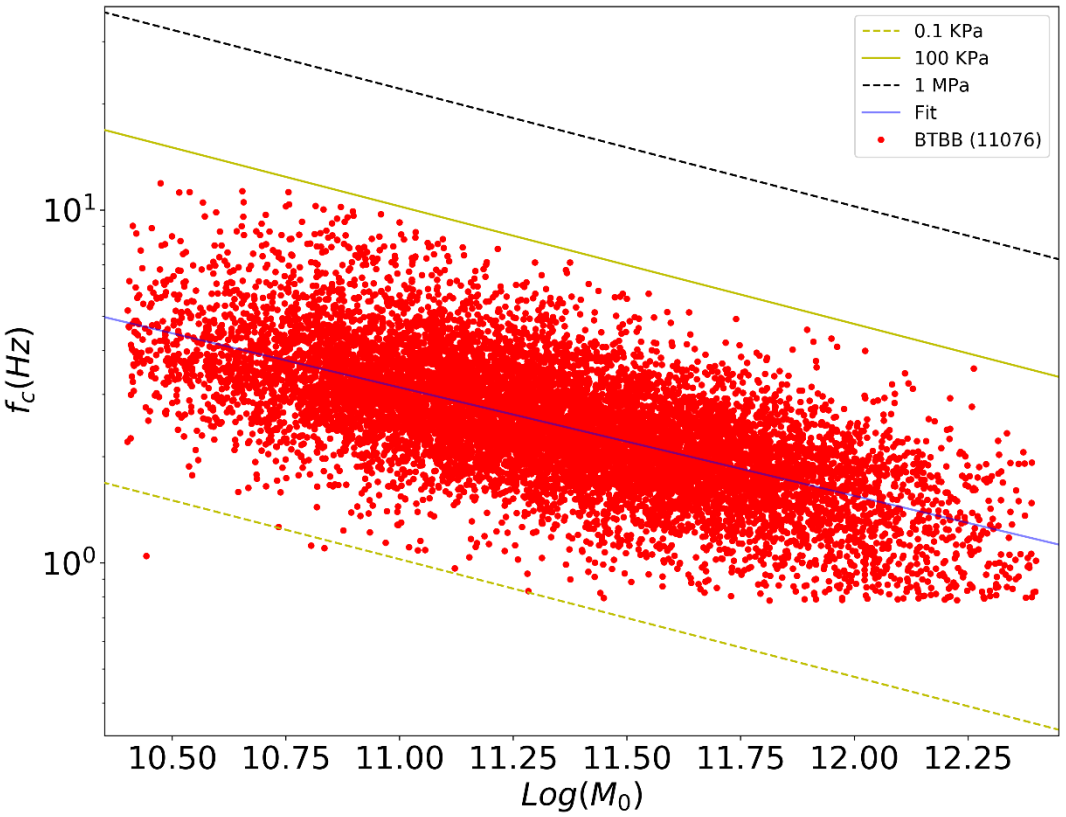

Figure 5.7 Scaling law between the corner frequency and the seismic moment. The red points are the solutions per event; the blue line is the best fit curve, with a scaling of -3.4; the parallel lines indicate the scaling with stress drops ranging from $\Delta\sigma = 0.1$ KPa to $\Delta\sigma = 1$MPa. The error bars are represented with a 3σ confidence level.

As an example, we show the spectra and the solutions for one event (20120531_0326D, $M_W = 1.93 \pm 0.04$, $f_c = 1.59 \pm 0.12$ Hz, $\gamma = 2.26 \pm 0.17$) at all the stations (Figure 5.8) and the velocity records, the spectra and the solutions for 3 events (Figure 5.9, Figure 5.10, Figure 5.11) at the edges and in the middle of the explored seismic moment range (Event *20140505_2358H*, Station *N.UWAH*, $\log M_0 = 12.3$; Event *20150212_0123Q*, Station *N.GHKH*, $\log M_0 = 11.3$; Event *20151101_0439E*, Station *N.KWBH*, $\log M_0 = 10.3$).

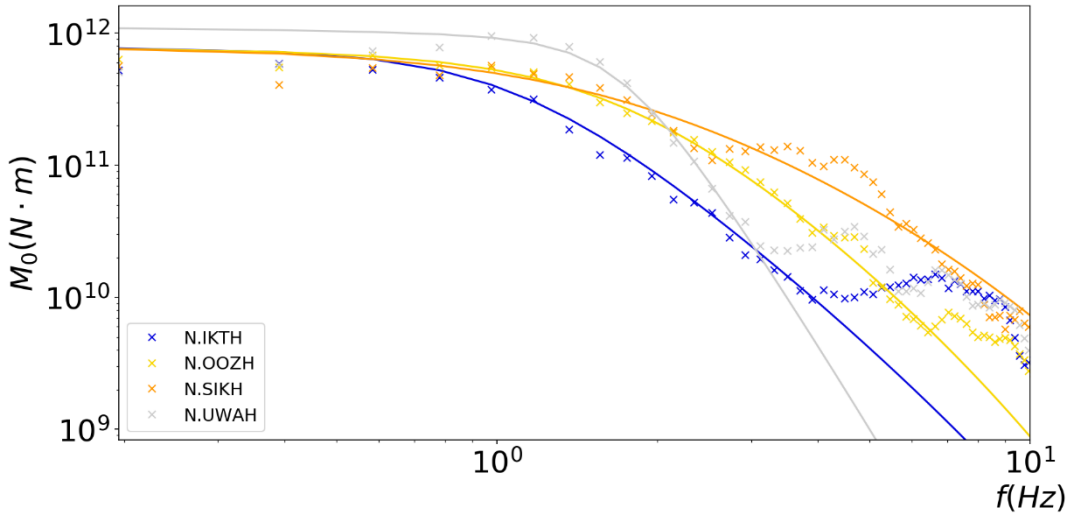

Figure 5.8 Spectra (discrete curves) and solutions (continuous curves), event 20120531_0326D; the estimated source parameters are $M_W = 1.93 \pm 0.04$, $f_c = 1.59 \pm 0.12$ Hz, $\gamma = 2.26 \pm 0.17$.

We found the typical behavior of the slow earthquakes, observing corner frequencies that are much lower than what expected for ordinary earthquakes sharing the same seismic moment. Furthermore, the retrieved order of magnitude of the stress drop (KPa) is well in the range of what reported in literature (Ide, 2014).

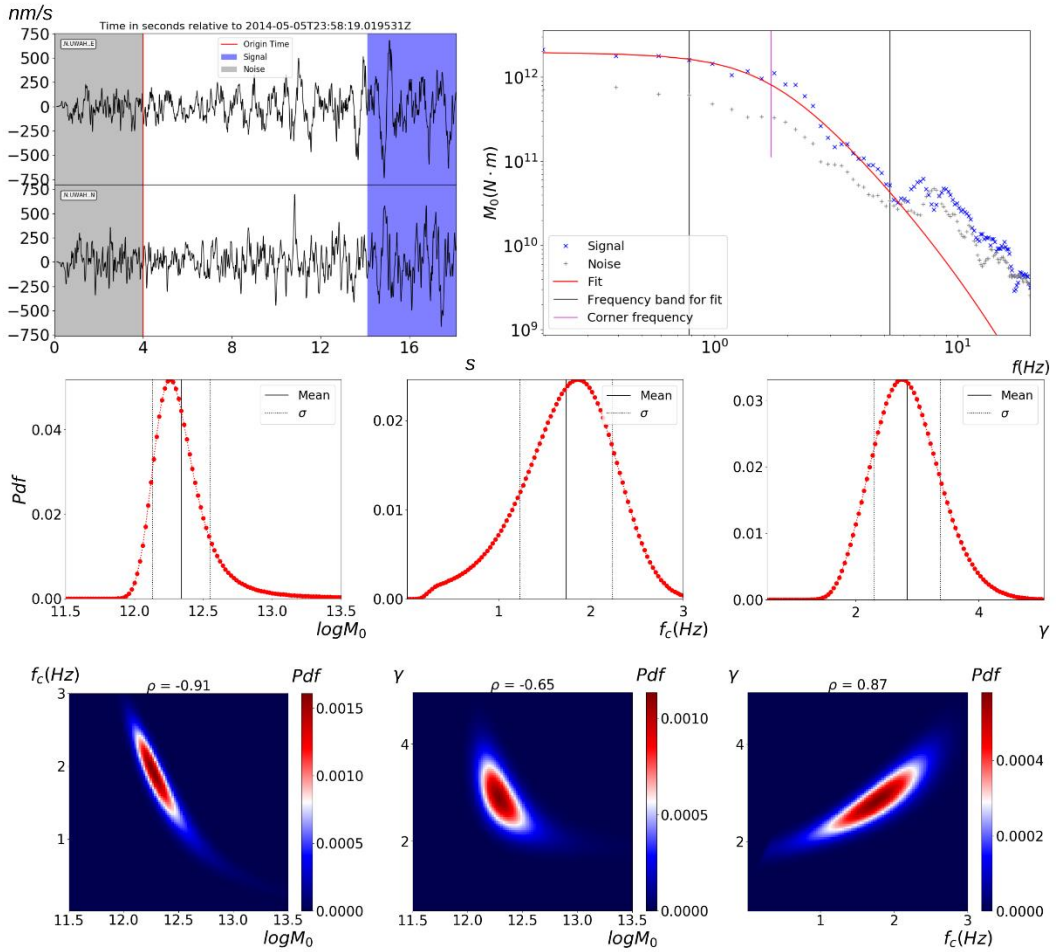

Figure 5.9 Example of accepted solution ($\log(M_0)$ = 12.3, event *20140505_2358H*, station *N.UWAH*). Top panels : signal (blue windows) and noise (grey window) (left), signal (blue curve) and noise (grey curve) spectrum and solution (red curve) (right). Middle panels : 1-D marginal PDFs for the parameters $\log(M_0)$, f_c, and γ. Bottom panels : 2-D marginal PDFs for the parameters $\log(M_0)$, f_c and γ.

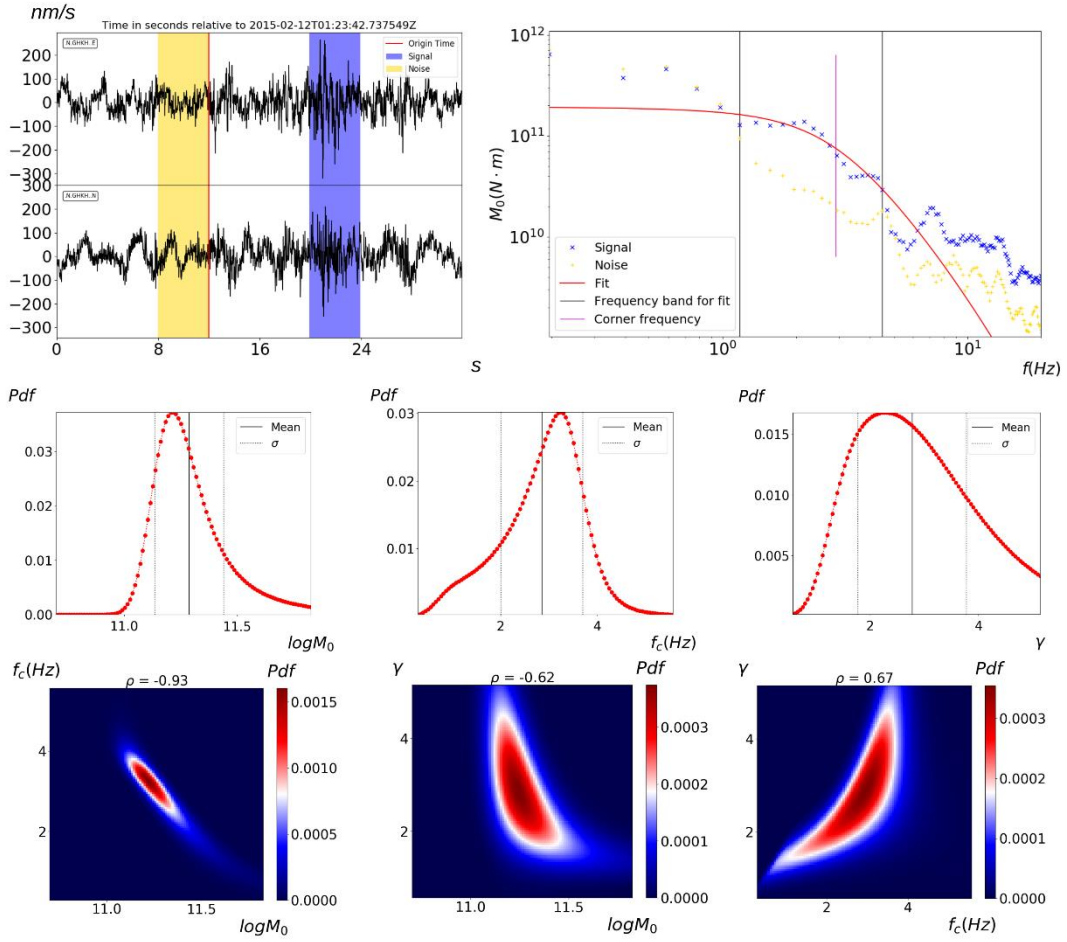

Figure 5.10 Example of accepted solution ($\log M_0 = 11.3$, event *20150212_0123Q*, Station *N.GHKH*). Top panels : signal (blue windows) and noise (yellow window) (left), signal (blue curve) and noise (yellow curve) spectrum and solution (red curve) (right). Middle panels : 1-D marginal PDFs for the parameters $\log(M_0)$, f_c, and γ. Bottom panels : 2-D marginal PDFs for the parameters $\log(M_0)$, f_c and γ.

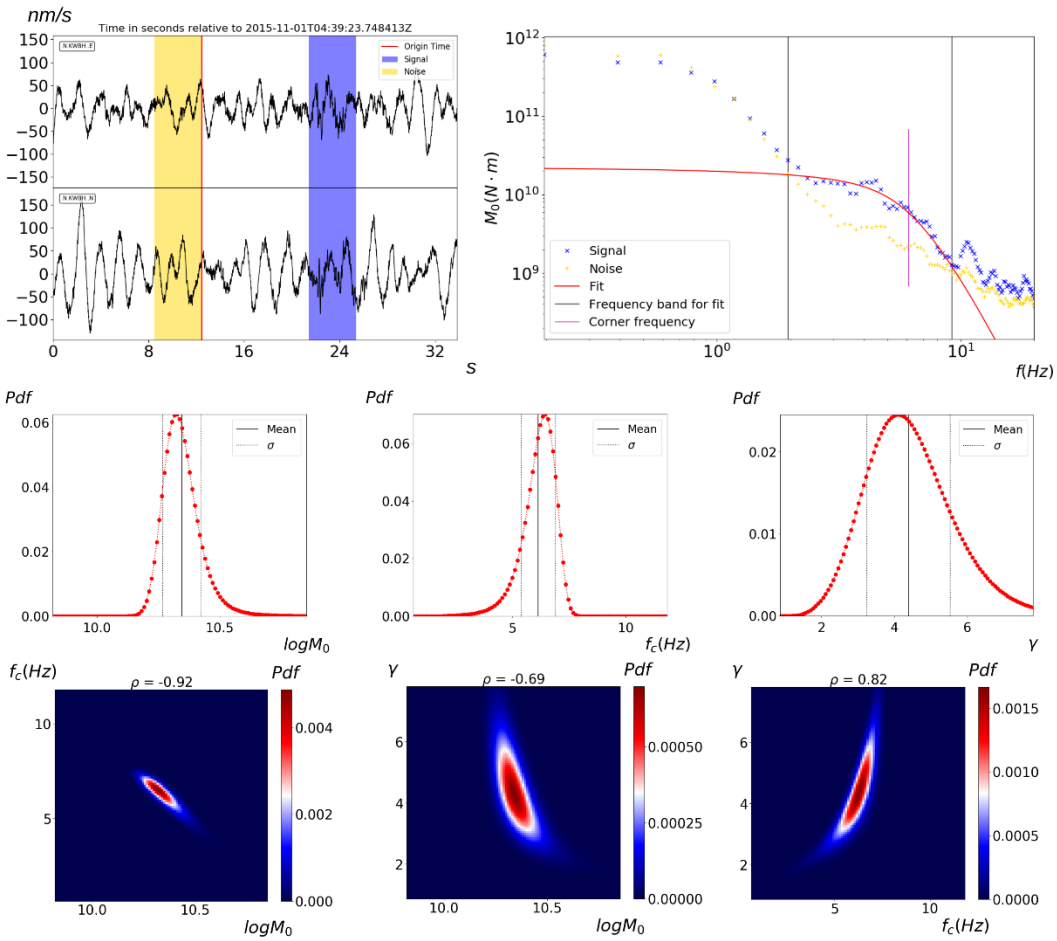

Figure 5.11 Example of accepted solution ($\log M_0 = 10.3$, event *20151101_0439E*, Station *N.KWBH*). Top panels : signal (blue windows) and noise (yellow window) (left), signal (blue curve) and noise (yellow curve) spectrum and solution (red curve) (right). Middle panels : 1-D marginal PDFs for the parameters log(M_0), f_c, and γ. Bottom panels : 2-D marginal PDFs for the parameters log(M_0), f_c and γ.

Although the events in Figure 5.7 show a large variability in the f_c value for fixed M_0, a scaling among corner frequency and seismic moment is evident. From a linear regression $\log f_c - \log M_0$ we obtained a slope whose reciprocal is -3.4, very close to the classical scaling for ordinary earthquakes (-3.0) (Aki, 1967).

In order to avoid that the regions in the seismic moment domain having the largest number of events (the central part of the explored domain) dominate the fit, we grouped the data in bins of size 0.03 (Figure 5.12). We estimated a scaling slope whose reciprocal is equal to -3.5 ± 0.5, compatible with the standard one, through an unweighted linear regression on the mean values of each bin; the unweighted choice is coming from the fact that we want to assign the same importance to each bin, regardless the number of observation it contains.

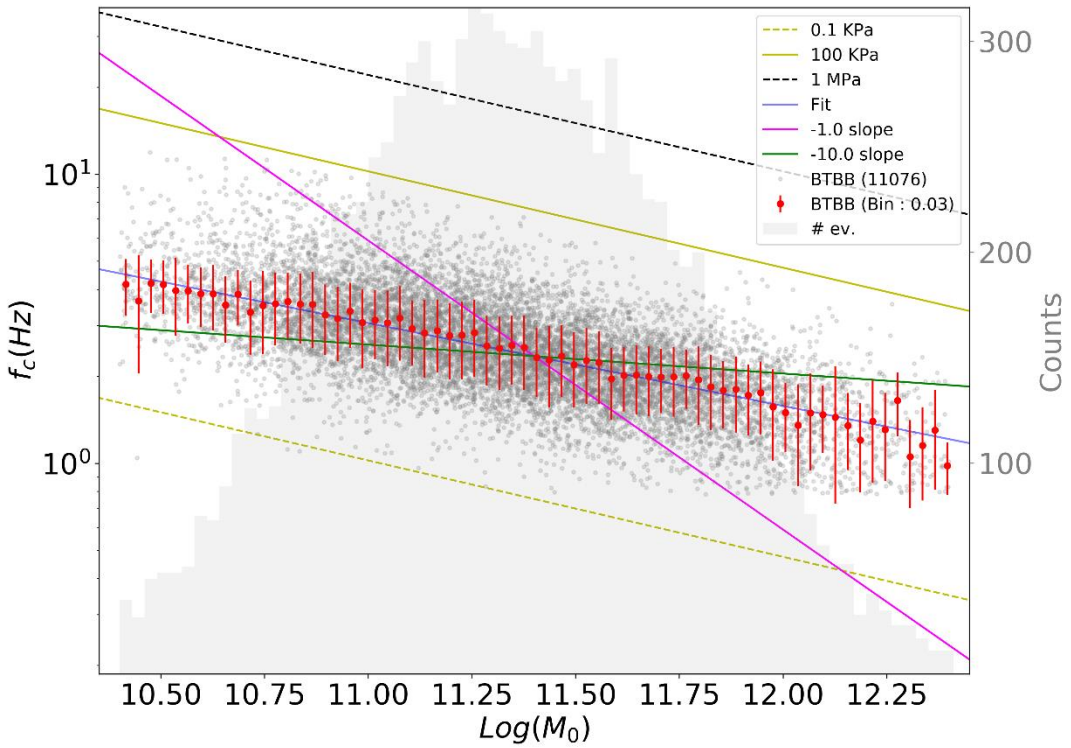

Figure 5.12 Scaling law among corner frequency and seismic moment; the grey points are the solutions per event; the red points are the solutions per bin (bin size = 0.03); the blue line is the best fit curve, with a scaling of -3.5; the green line is the -10 scaling and the magenta line is the -1 scaling; the parallel lines indicate the scaling with stress drops ranging from $\Delta\sigma = 0.1$ KPa to $\Delta\sigma = 1$MPa. The represented error is the weighted standard deviation.

We chose to represent two different uncertainties associated to the mean value in the bin : the weighted standard deviation σ_W (Figure 5.12), which represents the observed corner frequency variability in each bin, and the standard error $\overline{\sigma}$ (Figure 5.13), which is the error usually associated to the mean value of repeated measures (Taylor, 1997).
These errors are defined as follows :

$$\sigma_W \equiv \sqrt{\frac{\sum_{i=1}^{N} \frac{1}{\sigma_i^2}\left(f_{c_i} - \overline{f_c}\right)^2}{\sum_{i=1}^{N} \frac{1}{\sigma_i^2}}} \qquad (5.3)$$

$$\overline{\sigma} \equiv \frac{1}{\sqrt{\sum_{i=1}^{N} \frac{1}{\sigma_i^2}}}$$

where N is the number of corner frequency estimates for each bin and σ_i is the standard deviation of each f_{c_i} estimate.

Since the size of the uncertainties, both σ_W and $\overline{\sigma}$, is very similar among the bins, a weighted linear regression would give a result very close to the unweighted one.
For each bin, from Figure 5.12 we still observed an important variability of f_c. Nevertheless, the classical scaling becomes prominent.

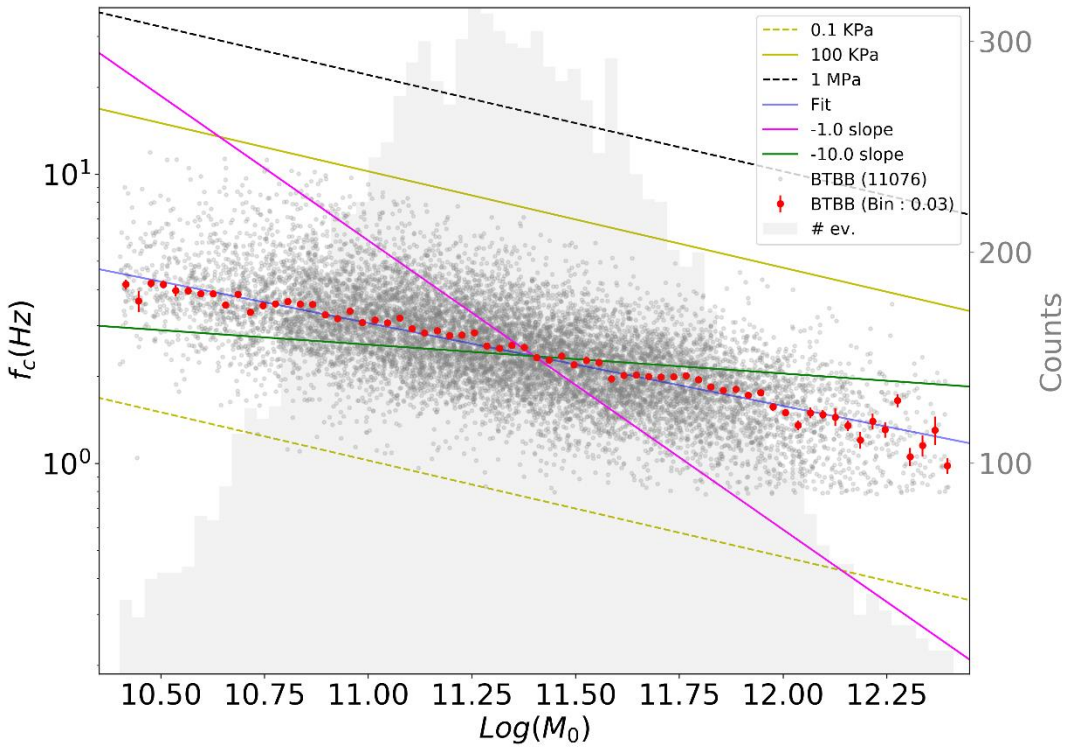

Figure 5.13 Scaling law among corner frequency and seismic moment, as represented in Figure 5.12, with the difference that the represented error is the standard error.

5.4. Discussion

We characterized the source of a very-large number of LFEs occurred in Nankai region between 2012 and 2016. We observed the typical behavior of LFEs, that is durations much longer than expected for ordinary earthquakes sharing the same seismic moment, and very low stress drops (~ KPa).

We specifically analyzed the scaling among corner frequency and seismic moment. When considering all the events and looking at their average behavior, the scaling is close to the standard one within uncertainties (Figure 5.12, Figure 5.13). The robustness of this result arises from the probabilistic method used to estimate the source parameters for single station (Chapter 3), combined with the quality selection criteria used for the automatic

processing of the data (Section 5.2.1). Additionally, we explored a large magnitude interval (two decades) and the scaling relies on a very large number of events per magnitude bin.

In Figure 5.12 we represented the two different scaling reported in literature for this kind of phenomena. To test the possibility that our dataset could be also described by any of these two models, we performed a bootstrap test. We extracted a single value of f_c per magnitude bin, to have a collection of corner frequency points as a function of the seismic moment. The probability to observe an almost flat behavior (green line, slope equal to $-1/10$, as retrieved by Bostock et al., 2015) or a steeper slope (magenta line, slope equal to -1, as retrieved by Ide et al., 2007) is very small, except in the case we extract data in a limited portion of the magnitude range (e.g. half a decade). Moreover, if we average the information from a large amount of data per bin (from 50 to 300), the uncertainty in the mean value becomes very small (Figure 5.13), indicating that a slope larger or smaller than $-1/3$ is very unlikely even in a small magnitude interval.

Hence, we can argue that the mechanism that rules the fracturing process of fault patches generating LFEs is the same as for ordinary earthquakes; it is characterized by a self-similarity which consists in a constant ratio among the seismic moment of the events and the cube of the radius of the ruptures. This ratio is proportional to the static stress drop.

Finally, we checked the possibility that this trend could arise from the combination of clusters of events having different scaling with different slopes and different intercepts, such that their combination would show an apparent -3 scaling. Thus, we plotted the events divided in classes (Figure 5.14).

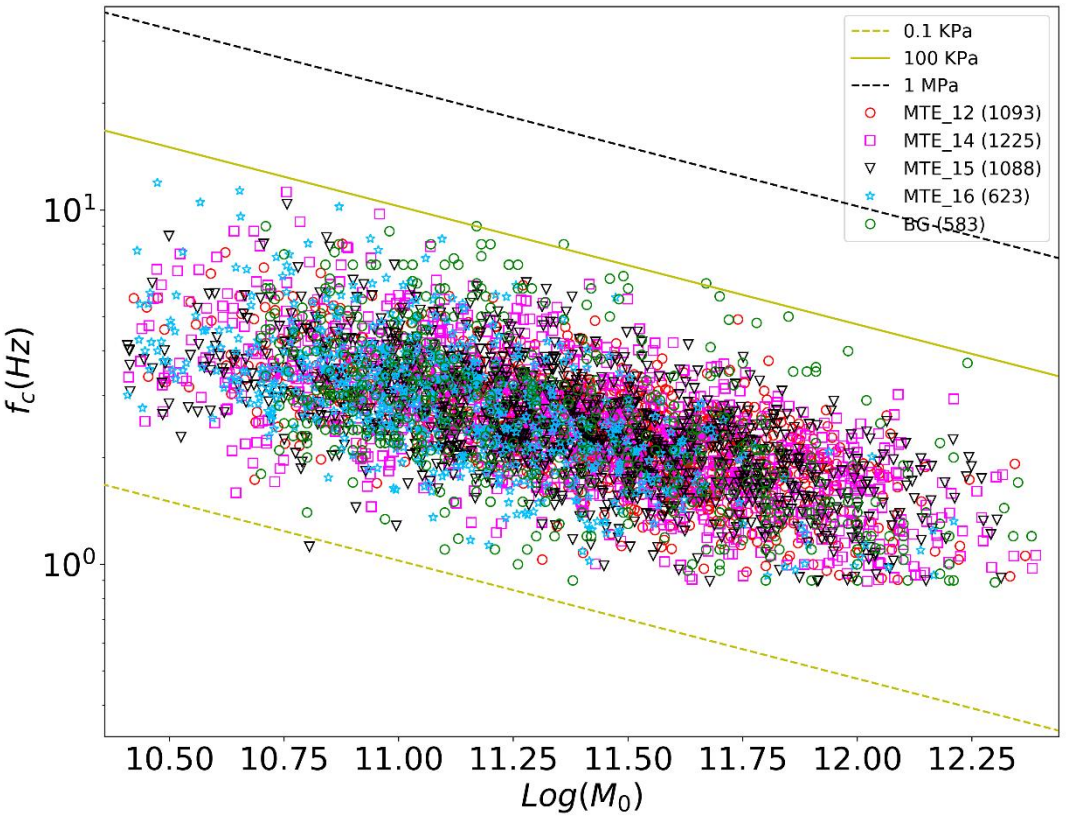

Figure 5.14 Scaling among corner frequency and seismic moment, each symbol represents a different collection of LFEs. MTE_12, MTE_14, MTE_15, MTE_16 are referred to the collection of LFEs coming from the major tremor event of the year 2012,2014,2015 and 2016, respectively; BG is referred to the collection of all the events not clustered neither in space nor in time. The parallel lines indicate the scaling with stress drops ranging from $\Delta\sigma = 0.1$ KPa to $\Delta\sigma = 1$MPa

We select as classes the collection of LFEs coming from a single, major tremor event in each analyzed year; these events are well grouped in space and time. Furthermore, we collected all the events - in the whole explored time interval - that are not clustered neither in space nor in time and we refer to them as background activity (BG). From Figure 5.14 we observe that each class shows a slope similar to the average one, and almost covers the same range in magnitude.

If we represent the slope (with 2σ confidence level uncertainty) per single class (Figure 5.15), we find that each slope is similar all along the classes and compatible with a -3 scaling.

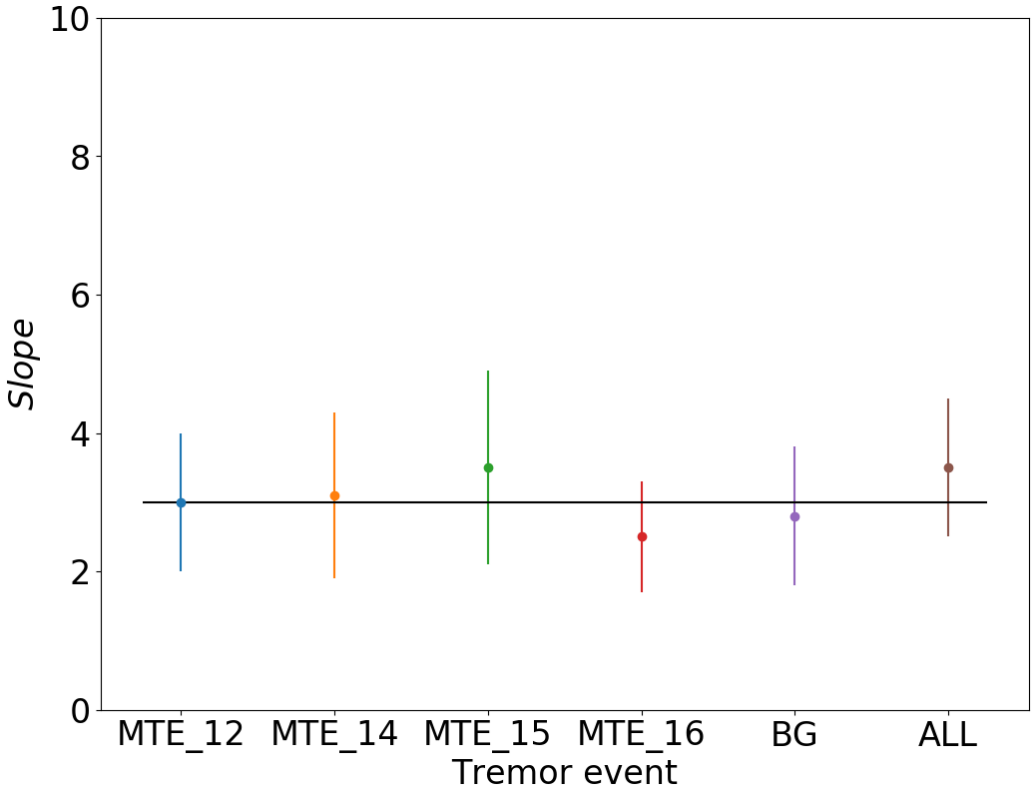

Figure 5.15 Scaling slopes per class of LFEs. MTE_12, MTE_14, MTE_15, MTE_16 are referred to the collection of LFEs coming from the major tremor event of the year 2012,2014,2015 and 2016, respectively; BG is referred to the collection of all the events not clustered neither in space nor in time.

Each class shows a different stress drop (Figure 5.16); although within a narrow interval ($1-5$ KPa), this could be a signature of the class.

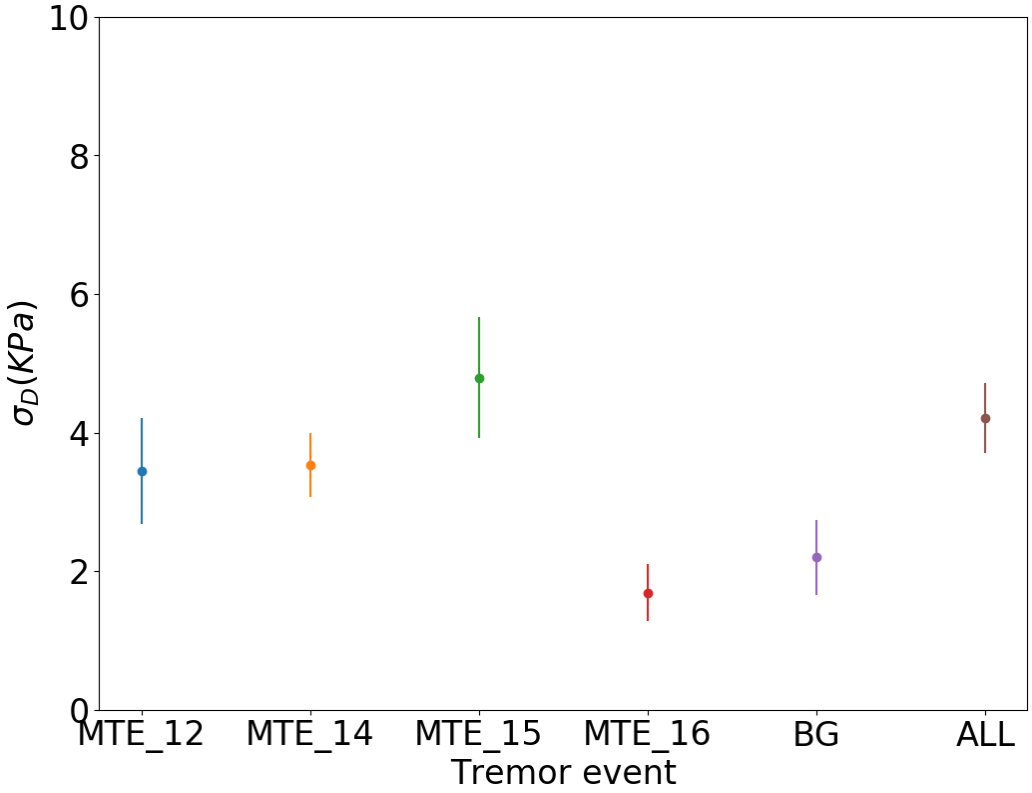

Figure 5.16 Stress drop per class of LFEs. MTE_12, MTE_14, MTE_15, MTE_16 are referred to the collection of LFEs coming from the major tremor event of the year 2012,2014,2015 and 2016, respectively; BG is referred to the collection of all the events not clustered neither in space nor in time.

We used the Madariaga's model to estimate the source radius from the corner frequency (2.45), and then the stress drop (2.31). The Madariaga's model is averaging the expected directivity effect on the corner frequency; since in most cases only few stations (~ 3) contribute to the source parameter estimation per event without a complete azimuthal coverage, we believe that this choice should be preferred to the Brune interpretation (2.36).

The coefficient $k = 0.21$ in (2.45) linking the corner frequency to the ratio between the S-wave velocity and the radius of the source has been computed assuming $v_R = 0.9\beta$. Ide (2014) found that slow earthquakes could be characterized by a v_R much lower than the S-wave speed, lying in the interval

$[0.1–10]$m s^{-1}. Decreasing the rupture speed implies a decrease in the k coefficient; since the stress drop estimate depends on the inverse of the cube of k , even a factor ~ 3 in k would imply an increase of a factor ~ 30 in the stress drop value. Thus, the estimate of the stress drop should be connected to an independent estimation of the rupture velocity.

6. Micro-seismicity in North Ibaraki

The Northern Ibaraki region in Japan has been interested by a significant increase of the seismicity after the Tohoku earthquake (2011); thus, a very-high sampling-rate network has been deployed by AIST (GSJ).
We investigated the seismic source properties for more than 1000 earthquakes occurred from 2016 to 2017 in this region; a selection on the full catalog (more than 10000 events) was made, based on geographic (6 clusters) and local magnitude $(0-4.5)$ criteria.
Thanks to the extremely high sampling rate of the dataset (1000 Hz), we were able to properly assess the characterization of the source parameters; in the explored magnitude range, expected corner frequencies usually fall beyond the frequency resolution for standard sampling rates ($f_{MAX} \approx 40-80$ Hz, $f_{SAMP} = 100, 200$ Hz). This network will thus provide a unique opportunity to evaluate earthquake source properties with proper resolution in the data space ($f_{MAX} \approx 400$ Hz, $f_{SAMP} = 1000$ Hz).

6.1. Data

The dataset is composed by 1061 events occurred in the North Ibaraki region (Figure 6.1) in the time interval 2016-2017 and recorded by the high sampling rate (1000 Hz) AIST seismic network (GSJtemp). Instruments are 3-component velocimeters with a flat response beyond 2 Hz; thus the a-priori frequency domain for spectral analysis is 2-400 Hz. This band could be modified during the processing, trace by trace, due to the signal-to-noise quality selection criterion (Section 6.2.1).

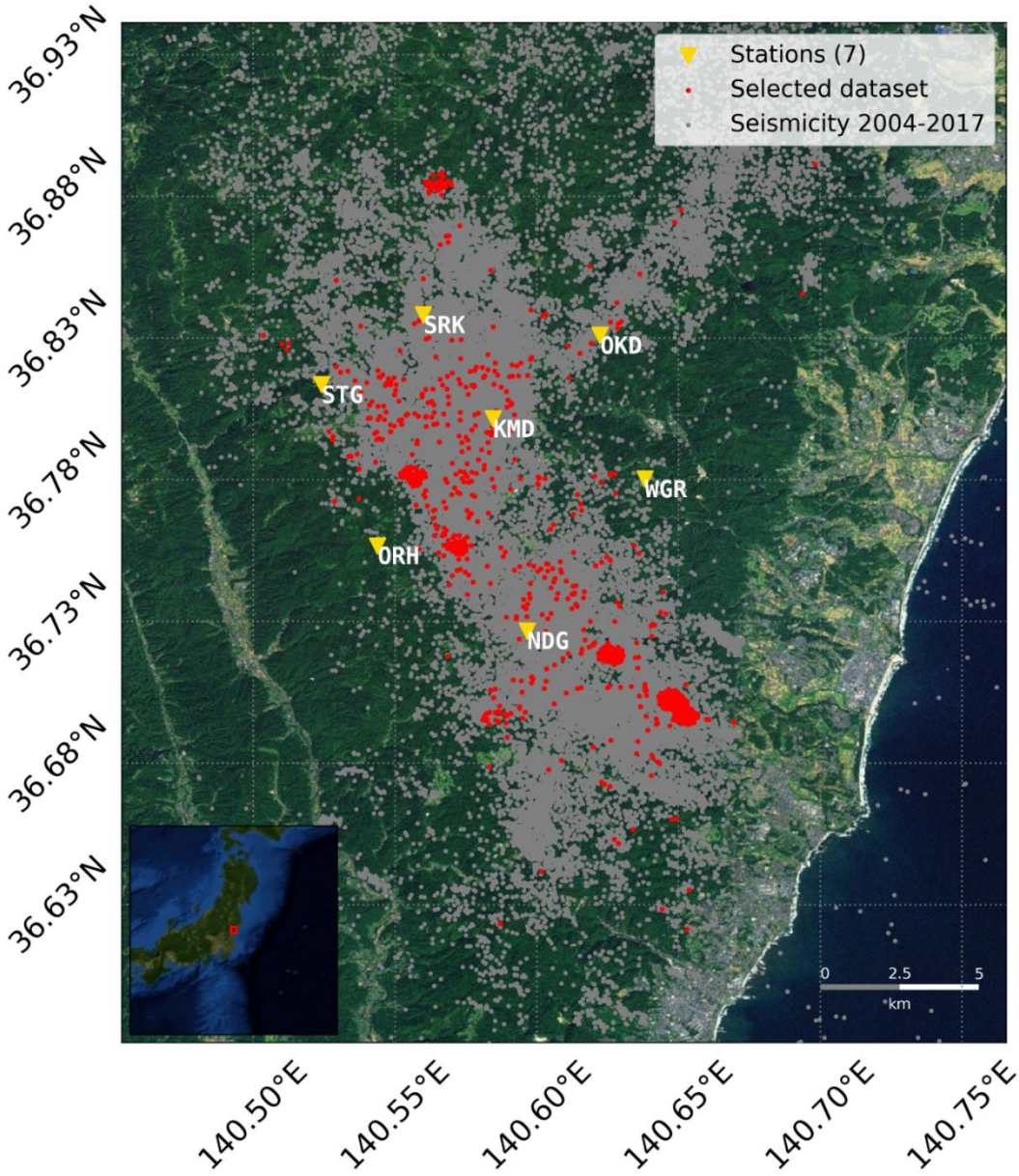

Figure 6.1 Map representing the location of the analyzed events (red dots), the overall seismicity (grey dots) and stations (yellow squares).

6.2. Processing

For each station record we pre-processed signal and noise, obtaining the amplitude spectra, as described in Section 4.2.

6.2.1. Quality control on automatic processing

We again applied the two quality selection criteria defined in Section 4.2.1 . The first-one is based on the signal-to-noise ratio, evaluated point by point in the frequency domain $[2-400]$ Hz. Contrarily to the frequency domain used for the Central Italy analysis, the minimum frequency is 2 Hz due to the velocimeter response curve, which is flat beyond 2 Hz, and the maximum frequency is still equal to $0.8 \cdot f_{NYQUIST}$. The second-one is based on the similarity of each solution to a Gaussian function. Examples of the signal-to-noise ratio quality selection and of the solution quality selection are reported in Figure 6.3 and Figure 6.4, respectively.

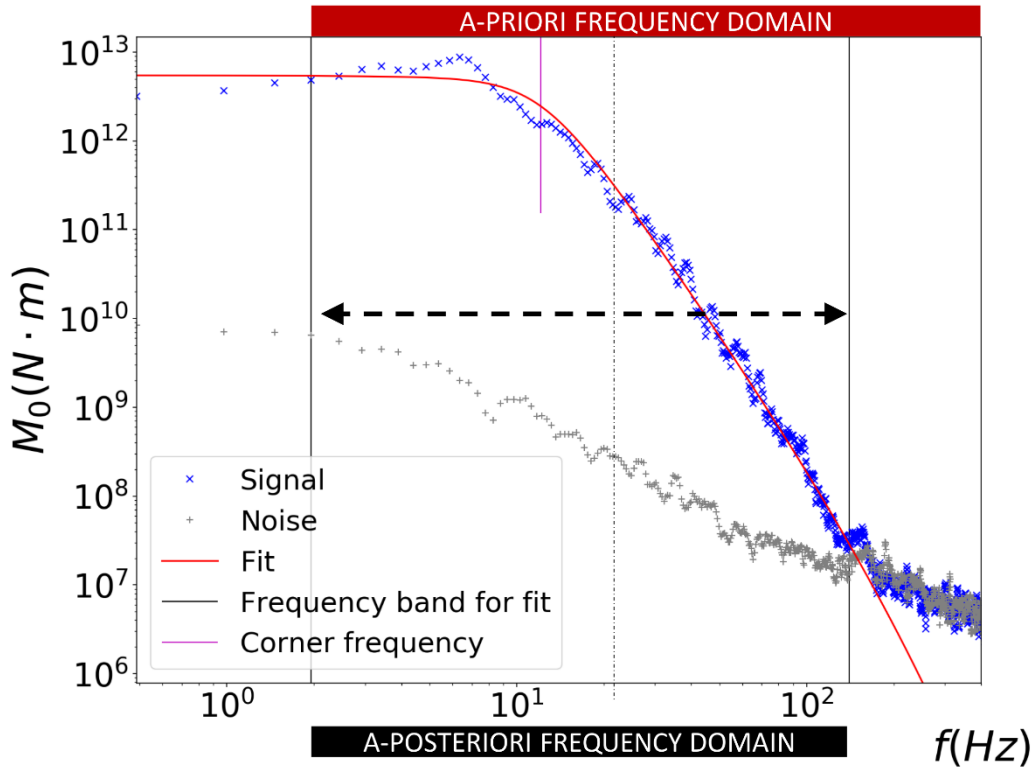

Figure 6.2 A-priori (red rectangle) and a-posteriori (black rectangle) frequency band for the spectrum fit (red curve). The blue curve is the signal spectrum, the grey curve is the noise spectrum; there is a clear effect of the noise spectrum (change of decay slope beyond 150 Hz) that we are able to avoid thanks to the signal-to-noise ratio criterion.

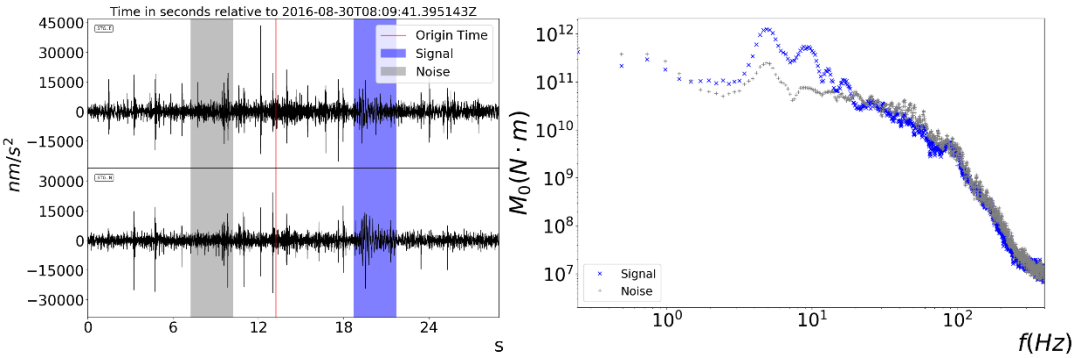

Figure 6.3 Rejected data (Event-ID 201608300809A, station STG) due to the signal-to-noise ratio criterion. On the left, the noise (grey window) and the signal (blue window); on the right, the noise (blue curve) and the signal (grey curve) spectrum.

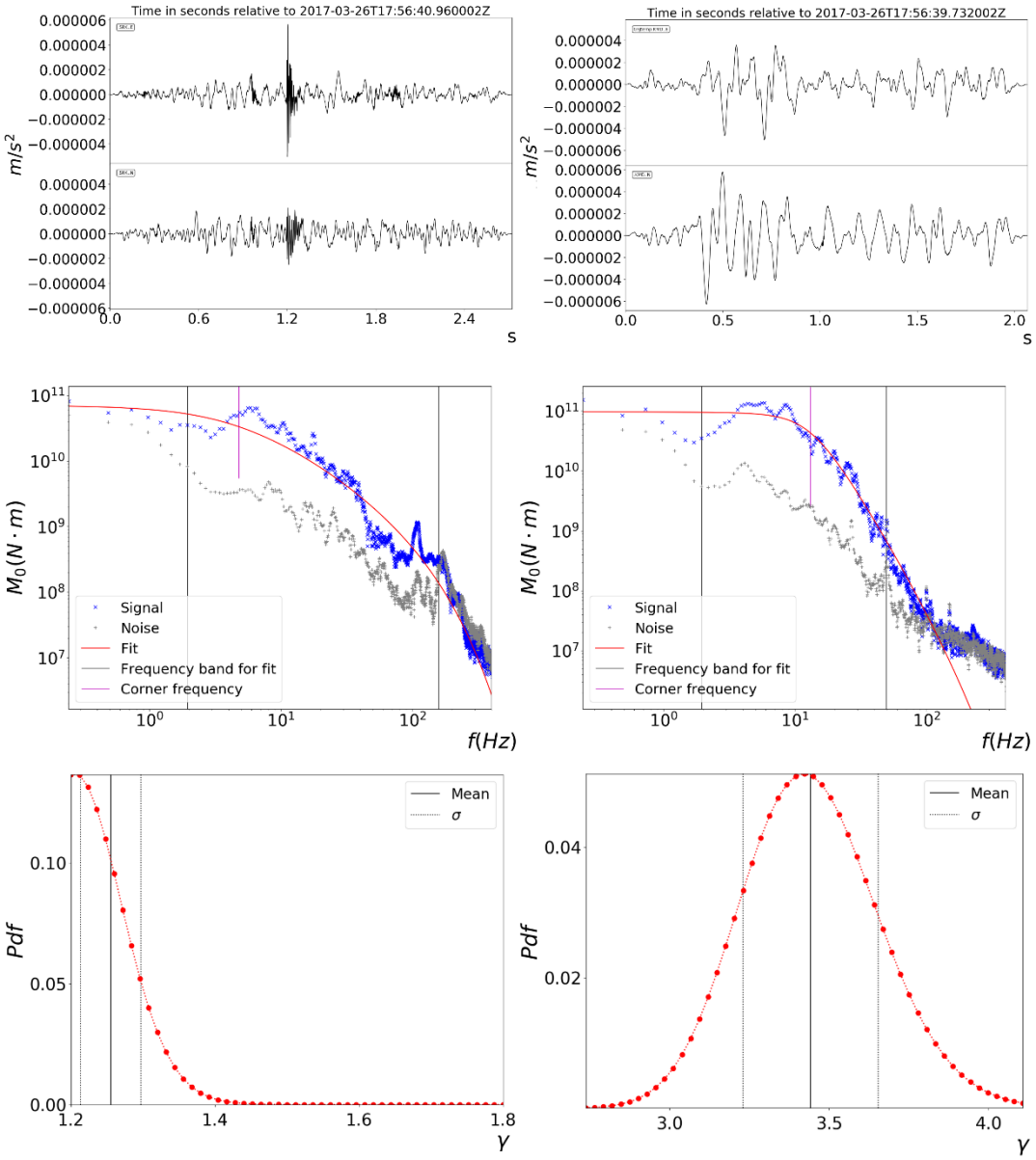

Figure 6.4 Rejected (upper left) and accepted (upper right) data due to the gaussian similarity criterion for the solution (Event-ID 201703261756D). The rejected data is very different from the S-wave observed at other stations for the same event.
Upper left : Signal (2.5 s, Station SRK); Middle left : signal spectrum (blue curve), noise spectrum (grey curve) and fit (red curve); Lower left : Rejected 1-D PDF for γ ; Upper right : Signal (2 s) at a different station (KMD) for the same event; Middle right : signal spectrum (blue curve), noise spectrum (grey curve) and fit (red curve); Lower right : Accepted 1-D PDF for γ .

6.3. Results

First, we analyzed the dataset using a 4D model space; we thus inverted for the 3 source parameters, and the Q-factor.

6.3.1. Q-value

Q-values as obtained from the inversions are reported in Figure 6.5. A very low anelastic attenuation effect is observed (high Q values); this is consistent with the findings from literature for the explored region (Takahashi, 2012) (Figure 6.6). Moreover, the geological map of the area provided by the GSJ reports an Abukuma granitic rock in the depth interval 0-20 Km, which includes the rocks hosting the analyzed seismicity, located in the range 5-10 Km. For this rock, a high Q-value is expected (Lebedev et al., 2003) (Figure 6.7).

When Q is large, the spectrum becomes less sensitive to the variations of Q; thus, in this domain of the anelastic attenuation both the inversion and the computation of the PDF for the estimation of the uncertainties become computationally expensive. On the other hand, since events are grouped in clusters, for all the events in one cluster analyzed at a single station we should not expect changes in the Q value. In Figure 6.8 we observe the distribution of the Q values for the station NDG for events in the same cluster. We observe that the 70 % of the retrieved values is above 1500, while other values fall in the range of 300<Q<1000, with an almost random distribution. Thus, we start by testing the hypothesis of fixing the Q value for couples of events in the same cluster and station. In Figure 6.9, we theoretically evaluate how the spectrum is affected by different values of Q. We see that up to 100 Hz there is almost no sensitivity to Q values larger than 1000. These spectra differ of half a magnitude order in the $\log(M_0)$ scale from the spectrum characterized

by the same source parameters and a Q value of 300. Hence, we decided to compare a Q value of 1500 with Q values smaller than 1000.

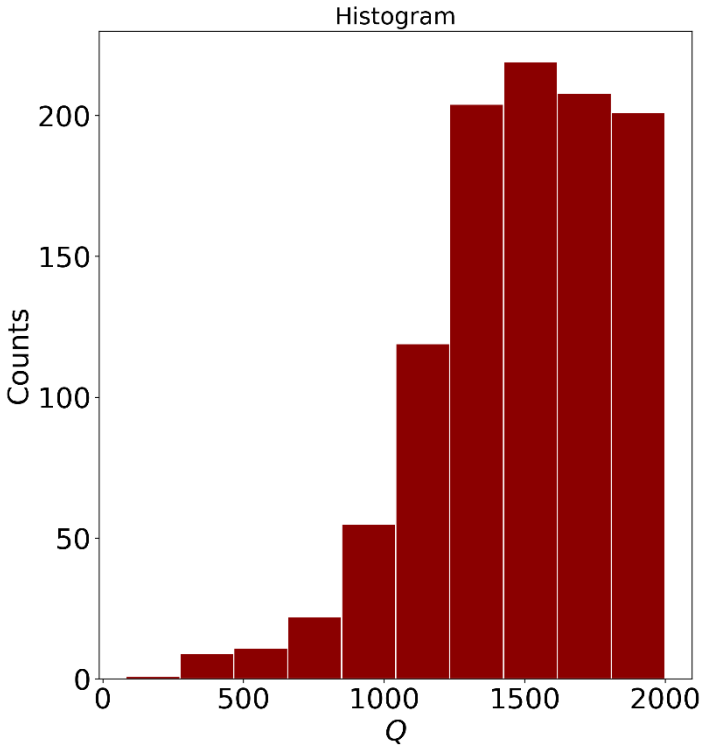

Figure 6.5 Histogram of the Q values obtained as solutions per event.

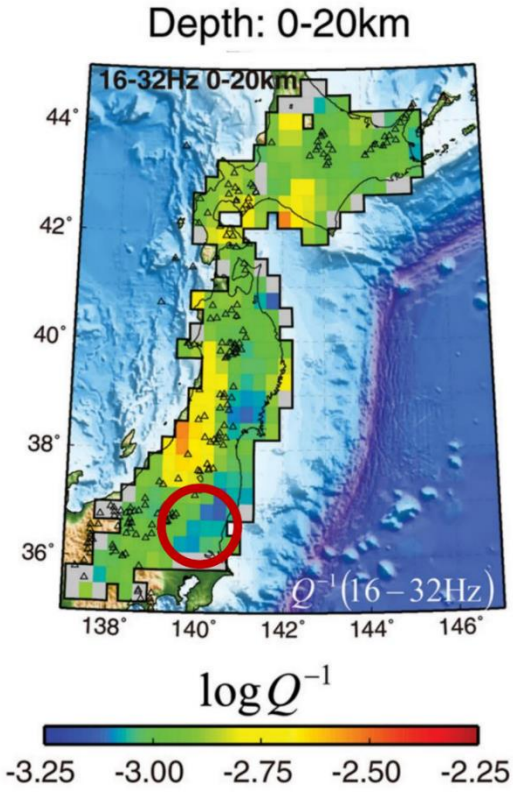

Figure 6.6 Q tomography in the frequency band 16-32 Hz, for a depth varying from 0 to 20 Km. The area explored in this study is in the red circle. Figure from Takahashi, 2012.

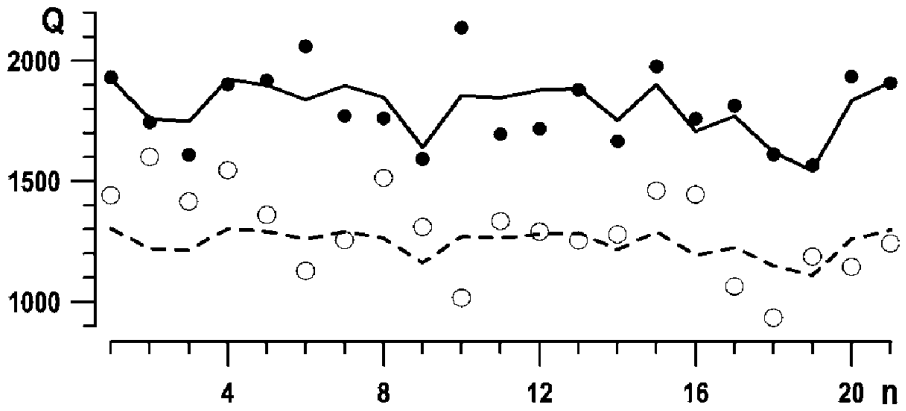

Figure 6.7 Q-factor estimates for granite. Empty and solid circles refer to two different measurement techniques. Figure from Lebedev et al., 2003.

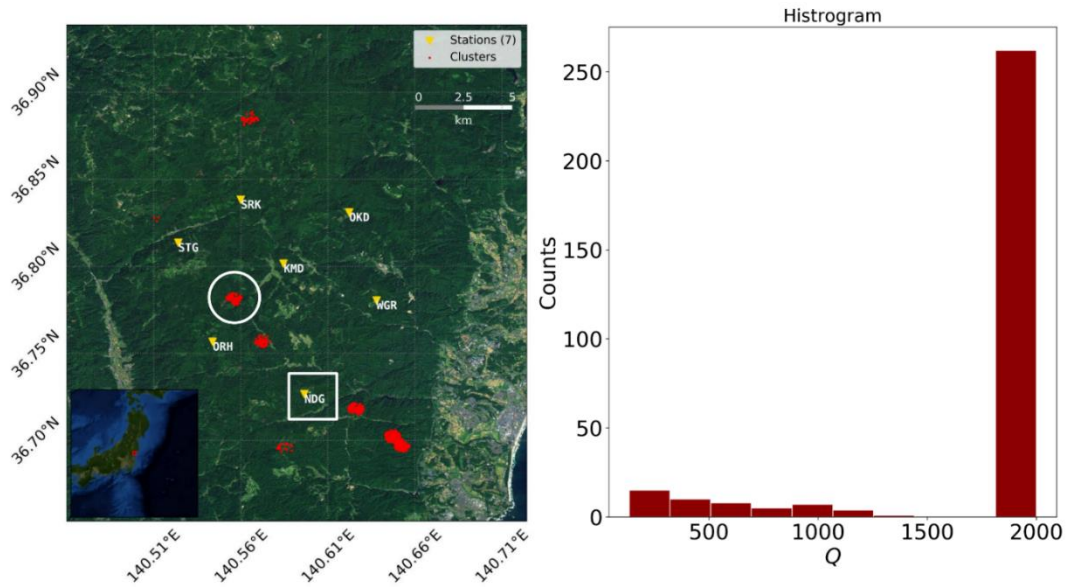

Figure 6.8 Q-values from cluster analysis. On the left, map with the location of the selected cluster (white circle) and the selected station NDG (white square). On the right, the histogram of the Q values obtained at the station NDG for the events of the cluster.

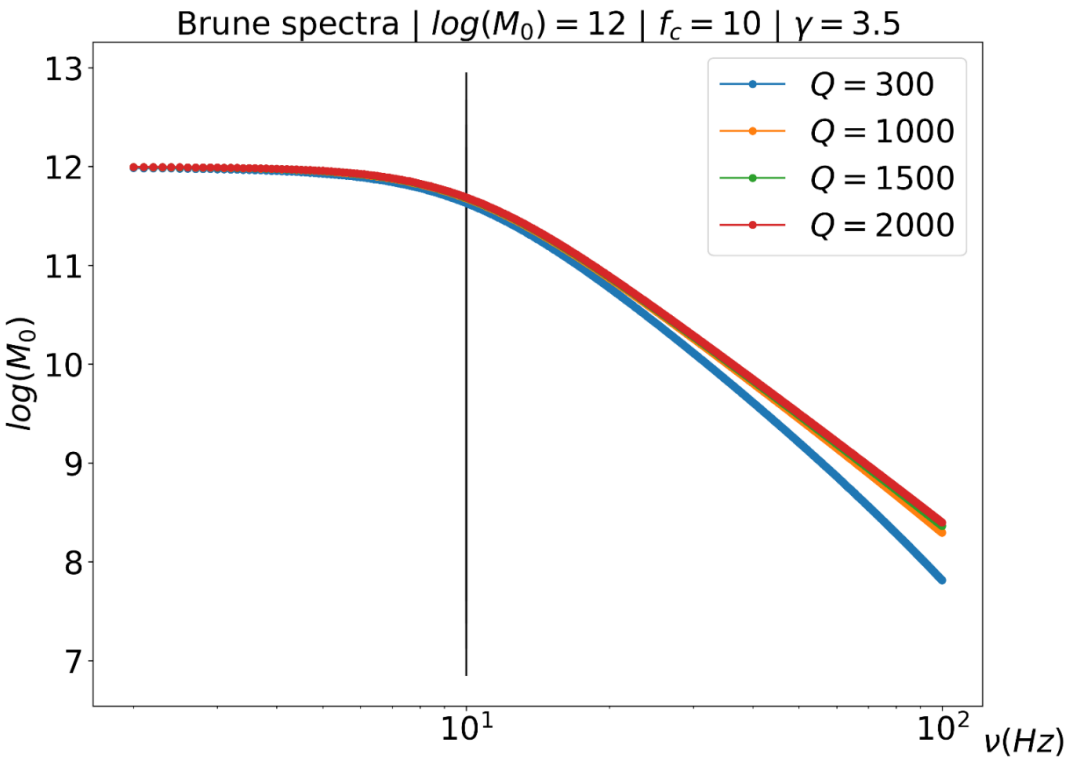

Figure 6.9 Expected Brune's spectra (3.4) for Q = 300, 1000, 1500, 2000. Even from a visual inspection, it is very difficult to distinguish between the expected spectra for the three high Q-values.

The tests show the comparison between the case with Q = 1500 and the case of Q = 300 (high anelastic attenuation effect). The results are clearly pointing in the direction of Q = 1500 as the best value for the spectrum modelling.

In Figure 6.10 we report the histograms of the RMSE, defined as the square root of the MSE, for the two cases applied to all the source-receiver couples. We observe that the RMSE between observed and predicted amplitude spectra is significantly larger for Q = 300 (mean value 47 % larger). Furthermore, using the probabilistic framework, we evaluated the ratio between accepted and rejected solutions, and the estimated uncertainties.

In the case Q = 300, the number of accepted solutions is decreased by 44 % (Figure 6.11), moving from 6148 to 3462; the number of available data (single station records) is 7360.

In the case of Q = 300, the error on the corner frequency estimates is increased of a factor of 107 % (Figure 6.12), while the error on the seismic moment estimates is increased by a factor of 39 % (Figure 6.13). Thus, in the large majority of fits, a large Q value better describes the spectral decay as compared to Q=300. In Figure 6.14 we finally compare the solutions obtained for the two cases for the same observed spectrum.

Thus, we decided to perform the inversion fixing the Q value to Q=1500.

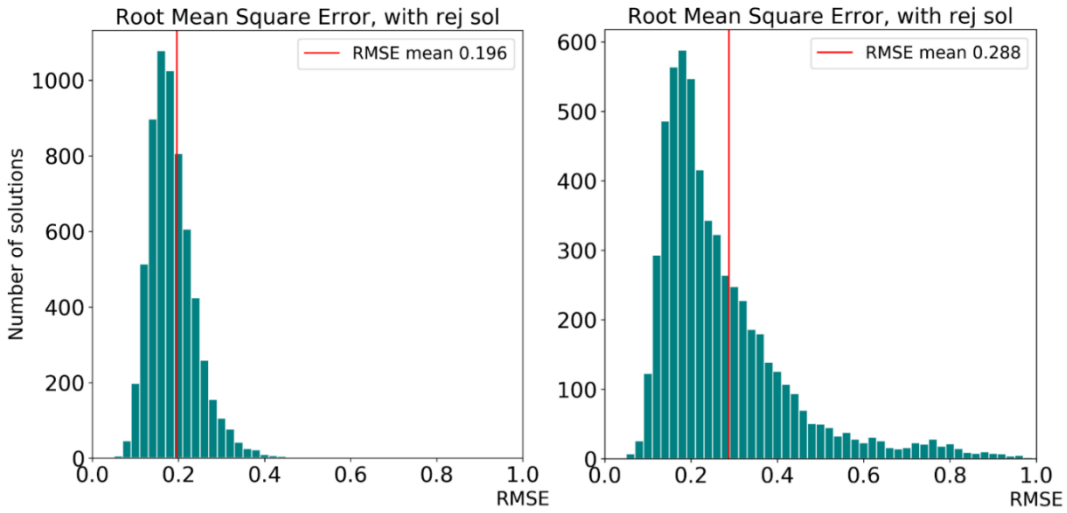

Figure 6.10 Histogram of the RMSE between the observed and predicted amplitude spectra. On the left, the RMSE is evaluated for the expected spectra with Q = 1500; on the right, Q = 300. For the model with Q = 300 the RMSE is 47 % larger compared to Q = 1500, indicating a worst fit.

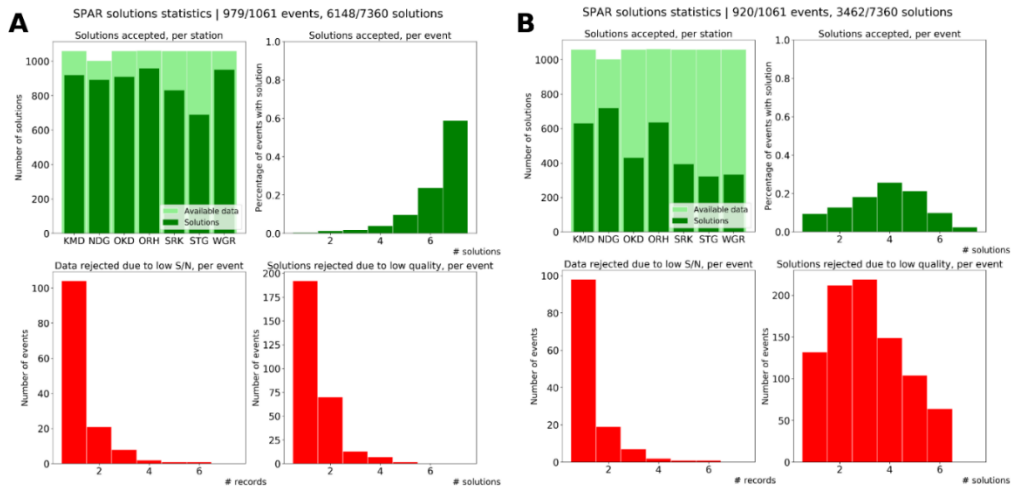

Figure 6.11 Statistics on the accepted and rejected solutions and data. Upper left : accepted solutions in dark green, available data (station records) in light green; Upper right : number of accepted solutions per event; Lower left : number of reject data, per event; Lower right : number of rejected solutions, per event. Panel A is referred to Q = 1500, panel B is referred to Q = 300.

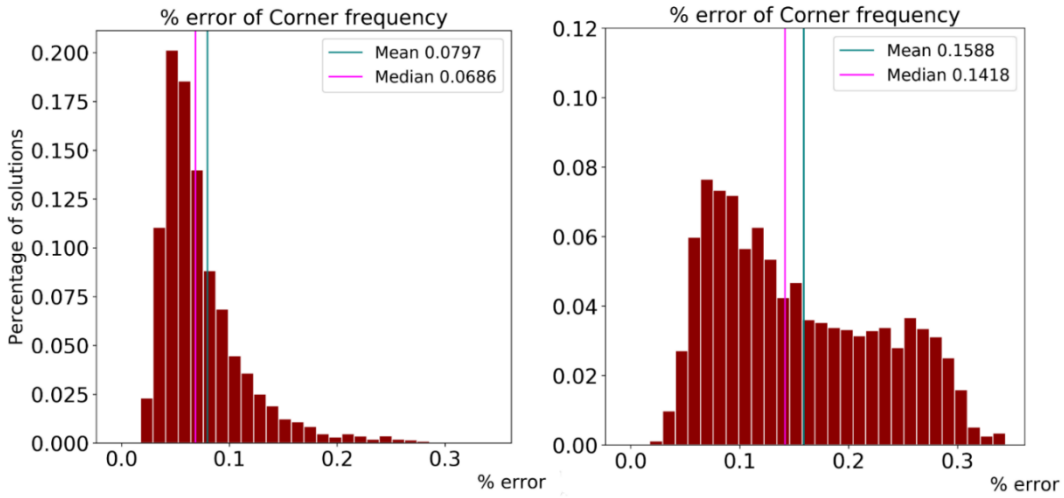

Figure 6.12 Histograms of the percentage error on the corner frequency. On the left, the errors retrieved with Q = 1500; on the right, Q = 300. In the case of Q = 300, the error on the corner frequency estimates is increased of a factor of 107 %, indicating a worst fit.

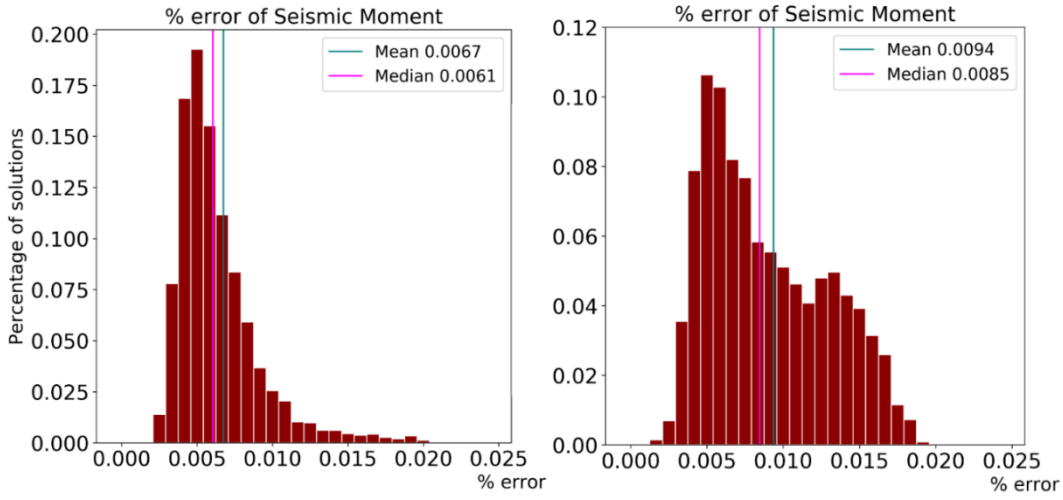

Figure 6.13 Histograms of the percentage error on the seismic moment. On the left, the errors retrieved with Q = 1500; on the right, Q = 300. In the case of Q = 300, the error on the corner frequency estimates is increased of a factor of 39 %, indicating a worst fit.

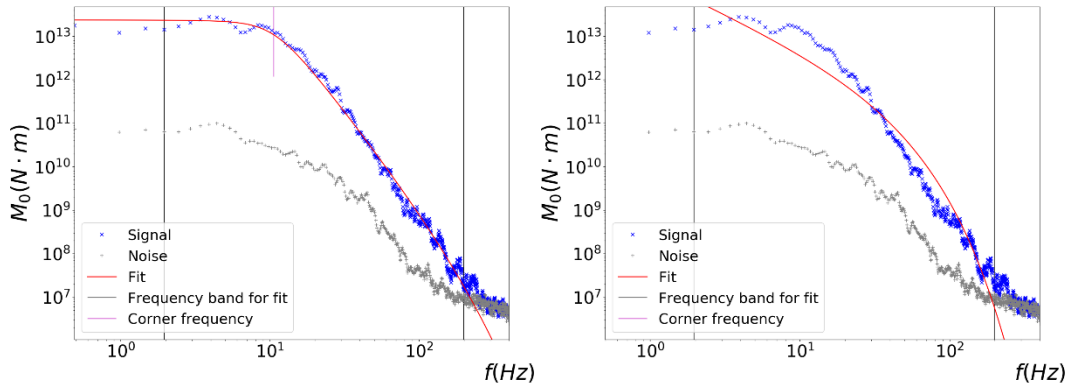

Figure 6.14 Signal spectrum (blue curve) and noise spectrum (grey curve) for the station KMD, event-ID 2017010811127C. On the left, the solution (red curve) for Q = 1500, on the right for Q = 300. The fit of the solution for Q = 300 is clearly worse than the fit of the solution retrieved for Q = 1500.

6.3.2. Standard versus generalized Brune's model

Most of the source inversion are performed using an omega-square model, as originally proposed by Brune (1970).

We thus compared the results obtained without fixing gamma (generalized Brune's model, Section 2.4.1) with the results corresponding to $\gamma = 2$. Since

there is a trade-off between Q and gamma, we compared the inversion performed with the generalized Brune's model and fixed Q-value to 1500 with the inversion performed with $\gamma = 2$ and Q-value as a free parameter. A comparison with a model with both γ and Q fixed would be meaningless, since there would be no degree of freedom to model the high-frequency spectrum decay.

When inverting for gamma with Q fixed, the histogram of the γ values is reported in Figure 6.15; The median value is $\gamma = 3.5$, and the probability to observe $\gamma = 2$ is very low.

RMSE comparison shows a higher RMSE mean value for $\gamma = 2$ (+ 26 %) (Figure 6.16). This is a clear indication for bad modeling. Once more, let us analyze the quality of the modeling using the statistics from the developed, probabilistic framework.

In the case $\gamma = 2$, the number of accepted solution is decreased by 28 % (Figure 6.17), moving from 6148 to 4454; the number of available data (single station records) is 7360.

In the case $\gamma = 2$, the error on the corner frequency estimates is increased by 170 % (Figure 6.18), while the error on the seismic moment estimates is increased by 57 % (Figure 6.19). All these comparisons show that the model with fixed Q and variable gamma better describes the data, as compared to the model with fixed gamma and variable Q. As an example, in Figure 6.20 we compare the best fit solutions for the two models and the same displacement spectrum. The representation of the observed spectrum is significantly improved when fixing Q and inverting for gamma.

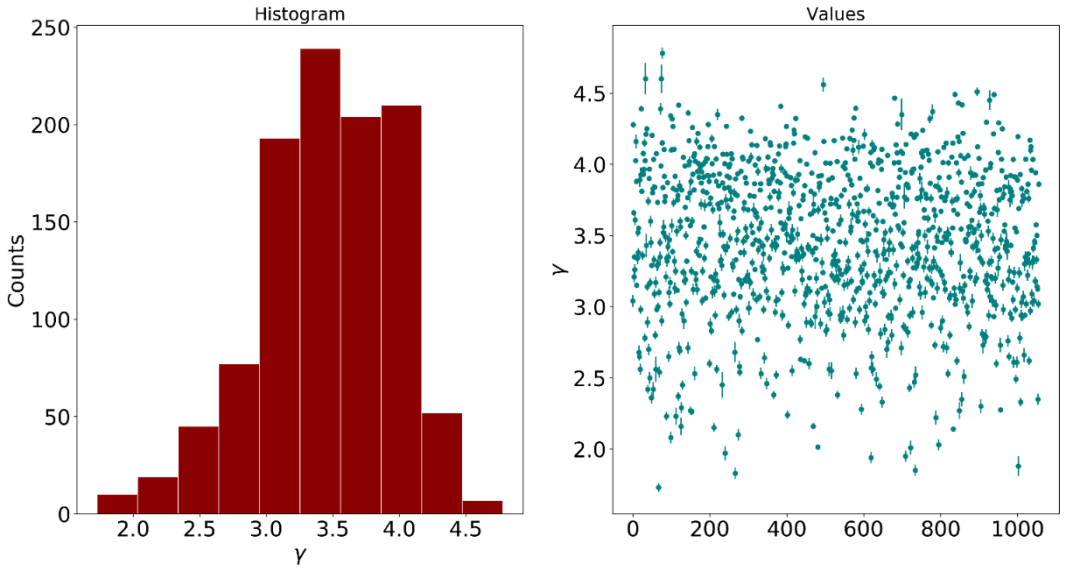

Figure 6.15 γ estimates per single events. In the left panel we plot the histogram for the parameter and in the right panel the retrieved values per event. The error bars are represented with a $3\,\sigma$ confidence level.

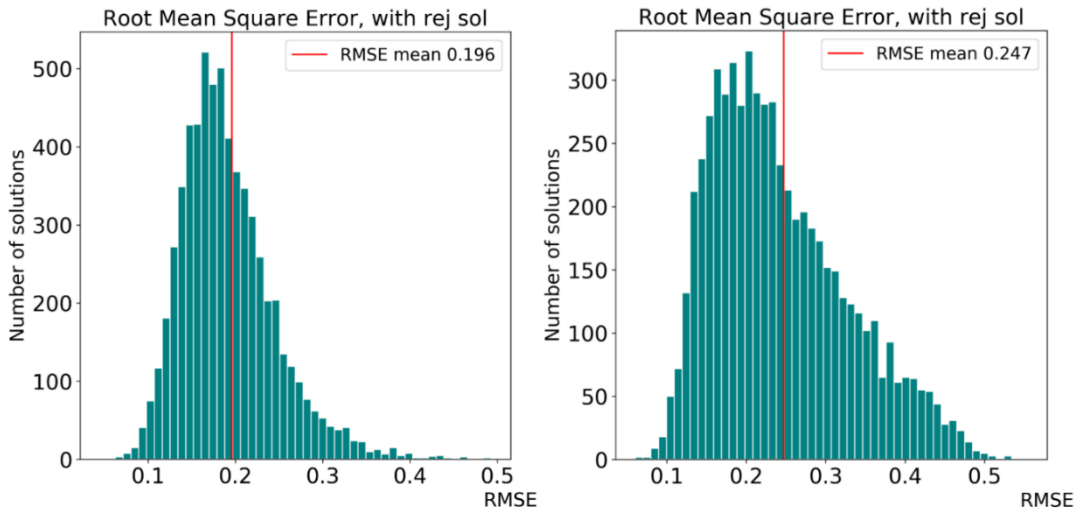

Figure 6.16 Histogram of the RMSE between the observed and predicted amplitude spectra. On the left, the RMSE is evaluated for the expected spectra with γ as a free parameter; on the right, $\gamma = 2$. For the model with $\gamma = 2$ the RMSE is 26 % larger compared to the free γ model, indicating a worst fit.

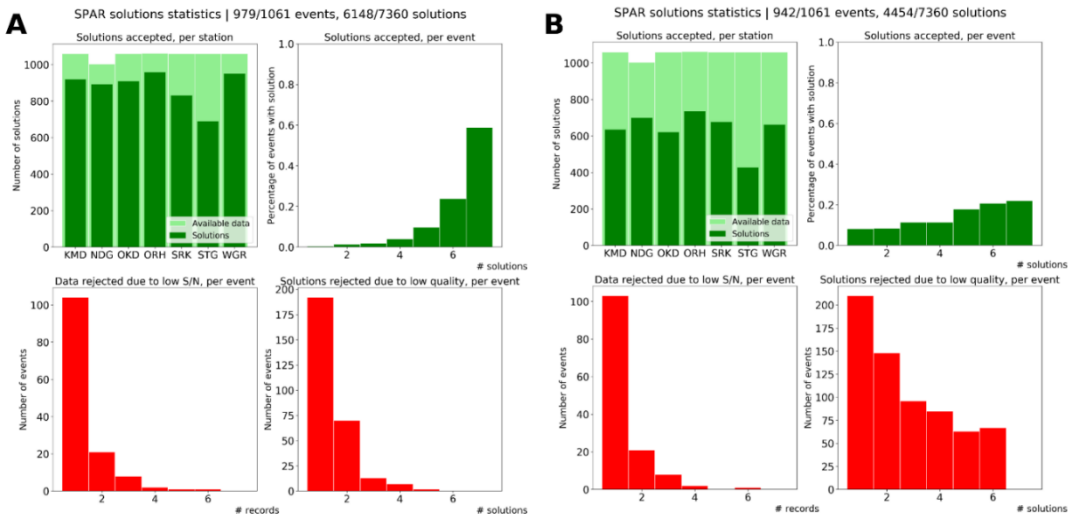

Figure 6.17 Statistics on the accepted and rejected solutions and data.
Upper left : accepted solutions in dark green, available data (station records) in light green; Upper right : number of accepted solutions per event; Lower left : number of reject data, per event; Lower right : number of rejected solutions, per event. Panel A is referred to the generalized Brune's model, panel B is referred to $\gamma = 2$.

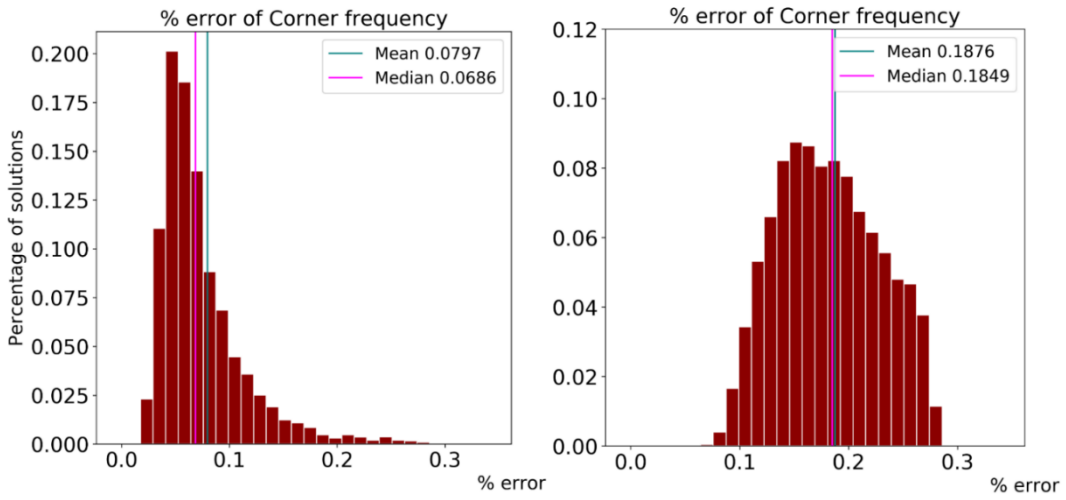

Figure 6.18 Histograms of the percentage error on the corner frequency. On the left, the errors retrieved with γ as a free parameter; on the right, $\gamma = 2$. In the case of $\gamma = 2$, the error on the corner frequency estimates is increased of a factor of 170 %, indicating a worst fit.

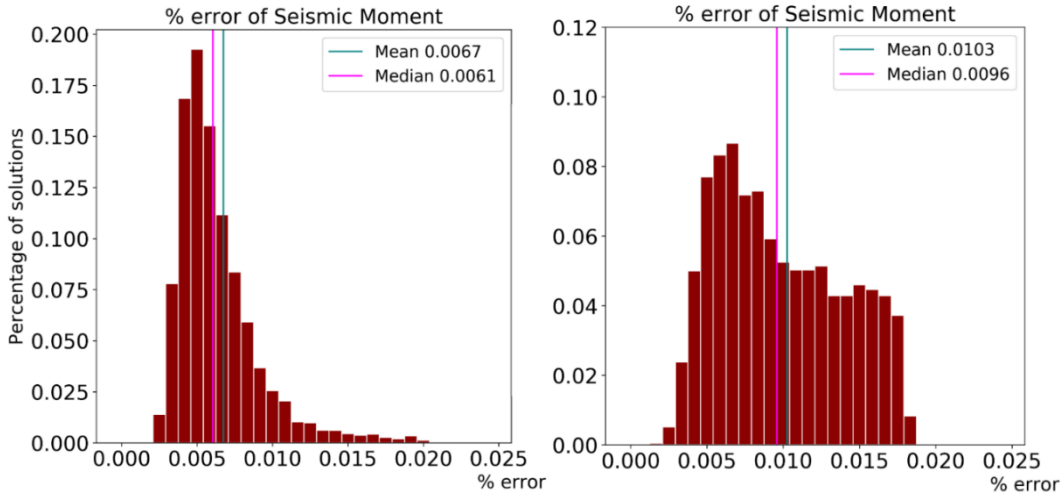

Figure 6.19 Histograms of the percentage error on the seismic moment. On the left, the errors retrieved with γ as a free parameter; on the right, $\gamma = 2$. In the case of $\gamma = 2$, the error on the corner frequency estimates is increased of a factor of 57 %, indicating a worst fit.

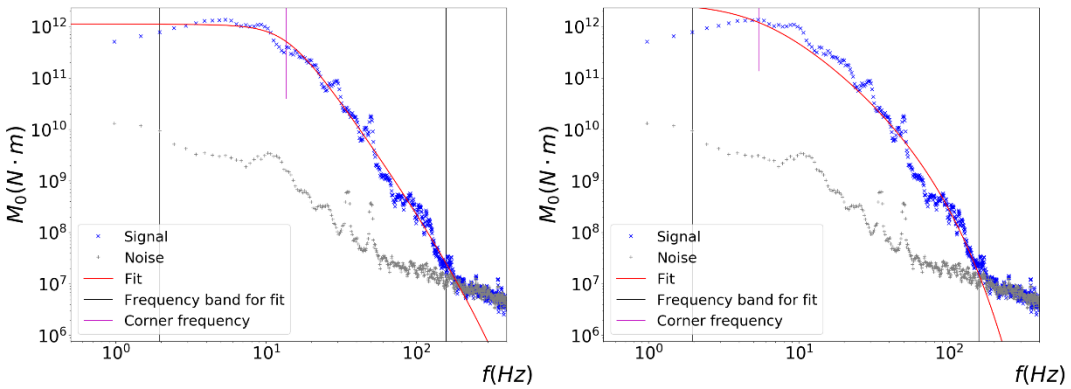

Figure 6.20 On the left the solution for the generalized Brune's model ($f_C = 13.6 \pm 0.8$ Hz) , on the right the solution for $\gamma = 2$ ($f_C = 5.6 \pm 0.9$ Hz). We represent the signal spectrum (blue curve), the noise spectrum (grey curve) and the solution (red curve). Station OKD, event-ID 201606240055A.

In addition, if we consider the distribution for the Q-values estimated with the omega-square model ($\gamma = 2$) we get a high anelastic attenuation effect for the entire dataset, with a median value for the quality factor Q= 250 (Figure 6.21).

Since it is common to obtain Q tomographic images relying on the omega-square assumption, this result puts a warning on correlation resolution among parameters.

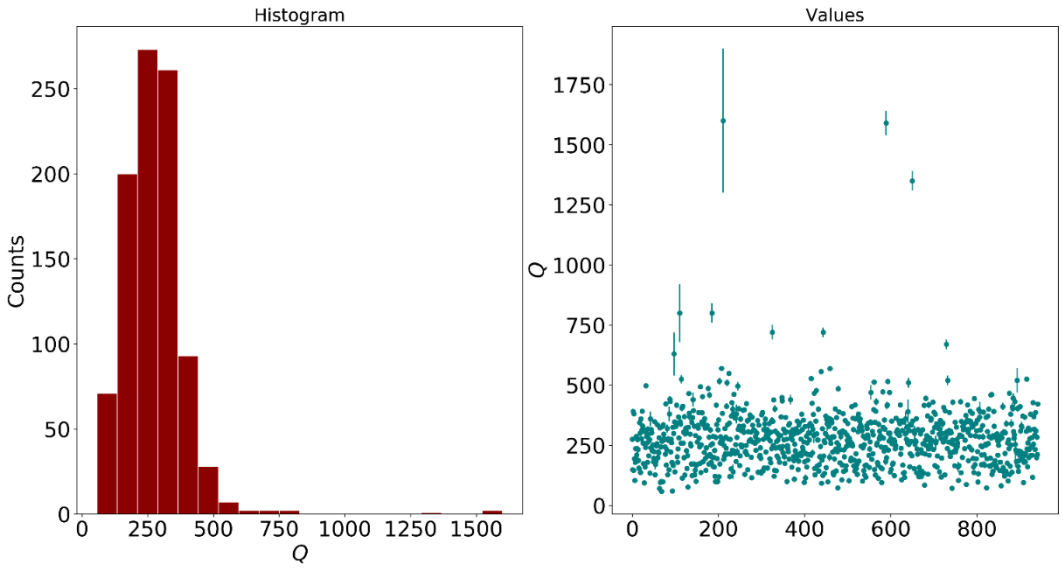

Figure 6.21 Q estimates per single events, assuming an omega-square model ($\gamma = 2$). In the left panel we plot the histogram for the parameter and in the right panel the retrieved values per event. The error bars are represented with a 3 confidence level.

6.3.3. Moment-corner frequency scaling law

We analyzed the scaling law between the corner frequency and seismic moment.

We found two very different behaviors in the explored seismic moment interval $(10^{10.5} - 10^{14.5})$ N m (Figure 6.22). The self-similarity does not hold in the low seismic moment range $(10^{10.5} - 10^{13.5})$ N m, where we observe an almost constant corner frequency despite the seismic moment; on the contrary, we observe a variability of the corner frequency as a function of the seismic moment in the upper range of the explored domain $(10^{13.5} - 10^{14.5})$ N m. Here the scaling is compatible with a -1/3 slope, corresponding to an average static stress drop of 5.9 MPa (Figure 6.23).

In Figure 6.24 we represent the spectra of two events having different seismic moment values, at the boundaries of the flat domain; we also represent the best fit solutions superimposed to the observed spectra. In both cases, we can observe a plateau up to 10 Hz, and then a clear decay of the spectrum. The estimated corner frequencies are 11.1 ± 0.6 Hz and 10.9 ± 0.5 Hz. Assuming a -1/3 slope we expect a corner frequency of 44 Hz for the smaller magnitude event, while fixing $f_c = 10$ Hz for the larger magnitude event.

Looking at the uncertainties in the corner frequency estimation, and at the discrepancies from the classical scaling relationship, the flattening of the corner frequencies around 10 Hz when decreasing the magnitude and the consequent deviation from the -3 scaling are a robust feature of the data.

In the framework of a circular rupture model, an upper bound for the corner frequency implies a minimum rupture size ($r \sim 100$ m) for the seismic sources in this area. Below this dimension, we do not observe any rupture to nucleate. The analyzed seismicity could describe families of repeated earthquakes rupturing same patches with different slip/stress drop; these could be related to changes in the frictional conditions of the patches owing, for instance, to lubrication mechanisms induced by fluid diffusion. Assuming a constant rupture velocity, this means that lower energy ruptures provide smaller slip Δu on the fracturing fault patches; these ruptures behave differently from larger events ($\Delta u \propto r$). This behavior holds for stress drops lower than $\backsim 1-4$ MPa. Above these values, a transition in the mechanism of rupture generation is observed and standard self-similarity occurs. This behavior is not new, and it has been observed also in the Northern Nagano area (Imanishi and Uchide, 2017) as reported in (Figure 6.25), although for a different seismic moment range ($10^9 - 10^{13.5}$ N m).

Assuming[2] the following slip-weakening model (Nielsen et al., 2016) :

$$\begin{aligned} &u \ll u_w, \quad \tau \approx \tau_p \\ &u_w < u < u_w \left(\tau_p / \tau_{ss} - 1\right)^{1/\alpha}, \quad \tau \approx \tau_p \left(u/u_w\right)^{\alpha} \\ &u \gg u_w \left(\tau_p / \tau_{ss} - 1\right)^{1/\alpha}, \quad \tau \approx \tau_{ss} \end{aligned} \tag{1.1}$$

where τ is the sliding shear stress, τ_p is the peak stress, τ_{ss} is the minimum sliding stress and $\alpha \approx 0.5$, we would expect a stress drop gradually increasing with slip if $u \approx u_w$ or $u < u_w$, and a constant stress drop $\Delta\sigma = \tau_0 - \tau_{ss}$ if $u \gg u_w$. Since we observe this behavior, we can obtain an estimate of the characteristic slip distance u_w from the observed transition point in the scaling law (Figure 6.22) : from $\log M_0 = 13.5$, $r = 100$ m and $\mu = 3 \cdot 10^{10}$ Pa, we obtain $u_w = 3$ cm.

[2] This interpretation has been suggested by one of the thesis reviewers, prof. S. Nielsen.

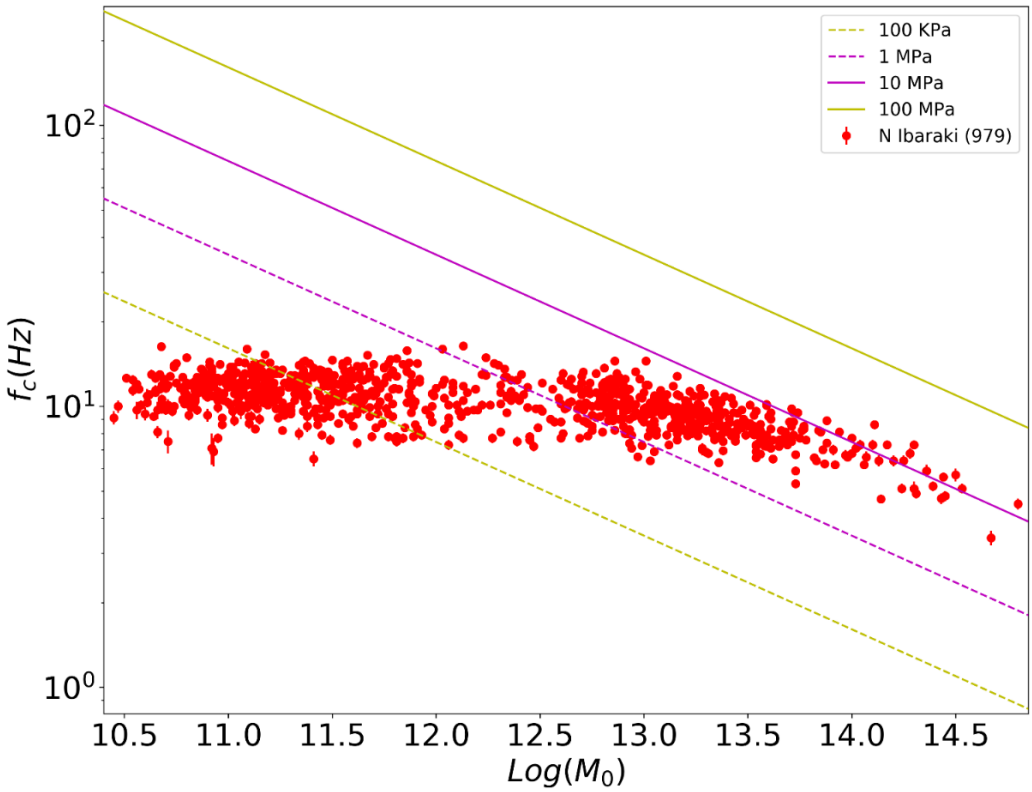

Figure 6.22 Scaling law between the corner frequency and the seismic moment. The red points are the solutions per event; the parallel lines indicate the scaling with stress drops ranging from $\Delta\sigma = 0.1$ MPa to $\Delta\sigma = 100$ MPa.

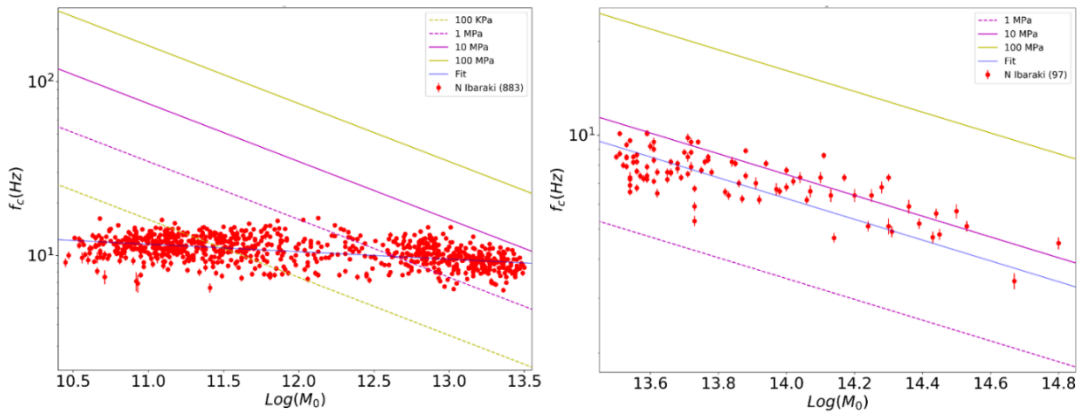

Figure 6.23 Scaling law as represented in Figure 6.22; here we focus on the two different behaviors observed in the explored seismic moment domain. On the left, constant rupture size; the blue line is the best fit curve (scaling = -23). On the right, classical self-similarity with an average stress drop equal to 5.9 MPa; the blue line represents the classical scaling -3.

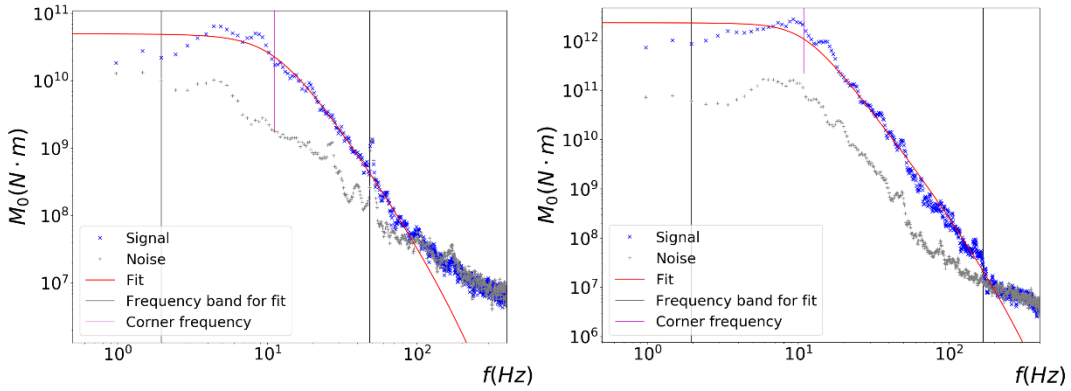

Figure 6.24 An example of the observed constant corner frequency, over two decades of seismic moment. On the left, $\log(M_0) = 10.7 \pm 0.1$, $f_C = 11.1 \pm 0.6$ Hz. On the right, $\log(M_0) = 12.4 \pm 0.1$, $f_C = 10.9 \pm 0.5$ Hz. Event-ID 201705070913A (Station KMD) and 201612290423B (Station OKD), respectively.

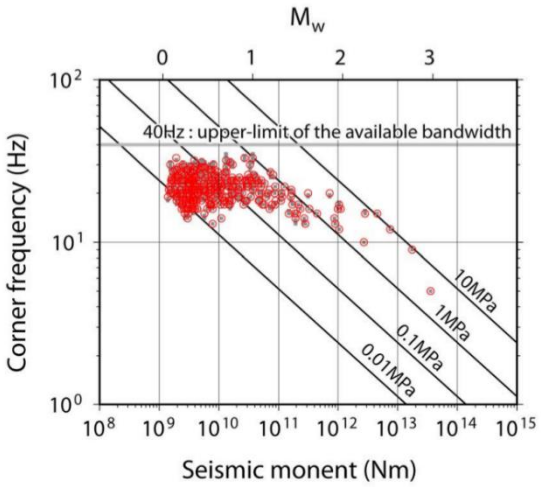

Figure 6.25 Scaling law in the Northern Nagano area. Figure from Imanishi and Uchide, 2017.

When fixing $\gamma = 2$ (omega-square model), the observed scaling law exhibits a mixed behavior (slope = - 1/7) among the constant corner frequency and the standard self-similarity (Figure 6.26).

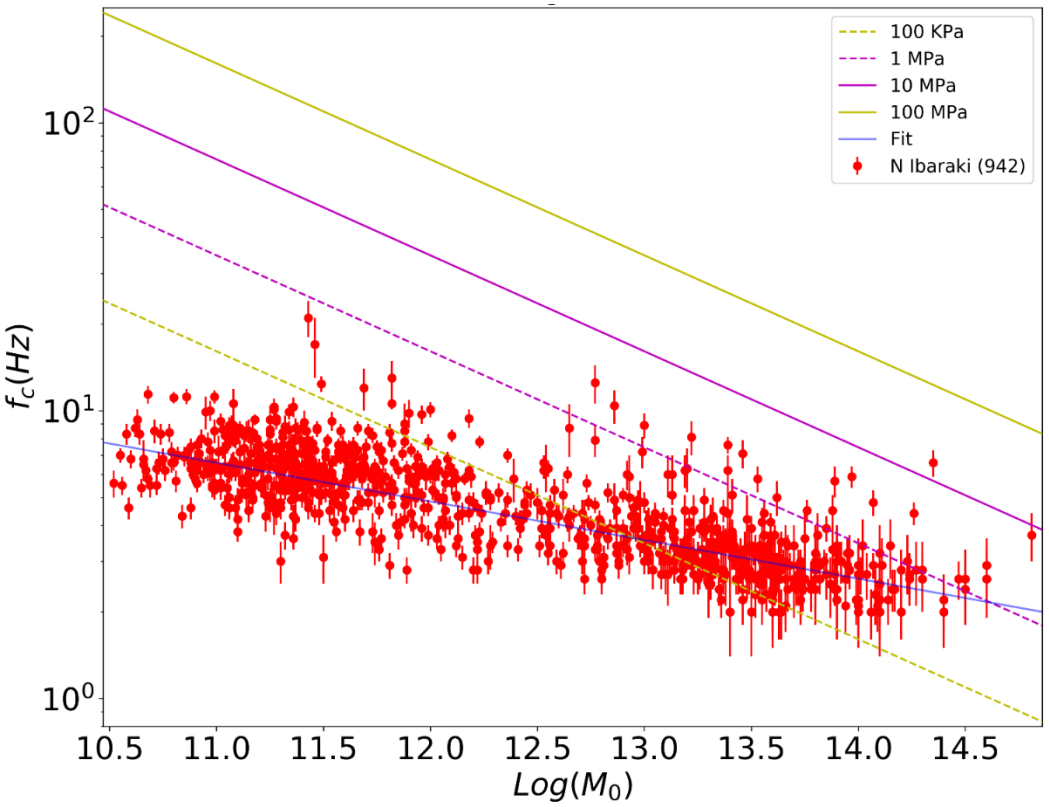

Figure 6.26 Scaling law among corner frequency and seismic moment, with the solutions per event (red points) evaluated assuming an omega-square model. The best-fit line, in blue, represents a scaling of -7; ; the parallel lines indicate the scaling with stress drops ranging from $\Delta\sigma = 0.1$ MPa to $\Delta\sigma = 100$ MPa.

6.3.4. Moment magnitude and JMA local magnitude

For each event, we have a moment magnitude (M_w) estimate coming from the seismic moment estimate (Hanks and Kanamori, 1979). We compared those magnitudes with the local magnitude (M_j) estimates in the catalog, provided by JMA (Figure 6.27).

We observe and underestimation of microearthquake size by the local magnitude scale. This result was already observed by Uchide and Imanishi (2018) (Figure 6.28).

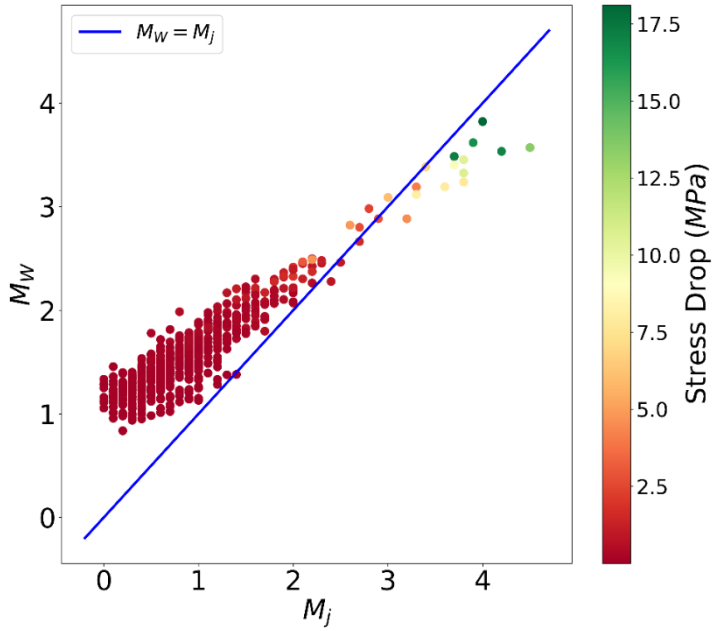

Figure 6.27 The retrieved moment magnitude, M_W, per event as a function of the local (JMA) magnitude, M_j. The color of the points indicates the stress drop evaluated for each event. The blue line represents the curve $M_W = M_j$.

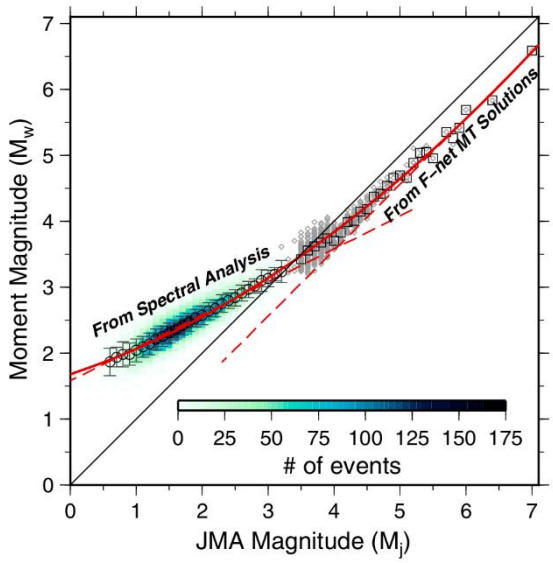

Figure 6.28 Moment magnitude, M_W, as a function of the local (JMA) magnitude, M_j. Figure from Uchide and Imanishi, 2018.

6.3.5. Directivity effect on corner frequency

Our dataset includes 6 clusters; we thus analyzed the retrieved source parameters as a function of the azimuth and the hypocentral distance, cluster by cluster, looking for a directivity effect on the estimates. We analyze the data also as a function of the distance, to be sure to rule out any unexpected propagation effect on the parameter estimates.

When collecting all data (Figure 6.29), we do not observe any specific trend. We then isolate the information per single cluster. Specifically, we analyze the cluster with the best azimuthal coverage. Results are shown in Figure 6.30 and Figure 6.31, where the source parameters are represented only as a function of the azimuth, since we do not observe any trend as a function of the hypocentral distance. In this case, we clearly recognize a directivity effect on the corner frequencies since we observe a periodicity of π (Figure 6.30). Supposing that this is due to Doppler effect, we are observing bilateral ruptures approximately along the direction N-S, which is the direction along which the corner frequency is maximum on average. Coherently, the minimum frequency emitted by the source is observed along the direction orthogonal to the rupture plane (station WGR, Azimuth = 90°). This interpretation is consistent with the focal mechanisms given by the NIED for the major events in the dataset, whose average strike is 164°.

The seismic moment estimates do not show any dependence on the azimuth. On the other hand, we still observe a variability on the γ parameter (Figure 6.31), although it does not follow the same trend as the corner frequency. At this stage we are not able to understand if this effect is related to the source or to the site. However, we observe a minimum of the γ function in correspondence of a minimum in the corner frequency. This indicates that the lateral station shows a smoother high frequency decay as compared to a directive station. Assuming that the source model has the same level of

complexity at scales smaller than the earthquake size, in the directive directions we have different apparent sizes, depending on the location of the small-scale asperities, if they are in the directive or anti-directive direction. These scales interfere negatively making the high-frequency decay steeper. This effect is minimized at a lateral stations, showing a smoother decay.
However, this variability could be ascribed to a propagation effect; the high-frequency decay has been obtained under the assumption of a frequency independent anelastic attenuation factor. Nevertheless, if such a dependence exists, Q should smoothly change with the frequency, since the spectra do not show a second slope (a *k* effect, Anderson and Hough, 1984) at high frequencies.

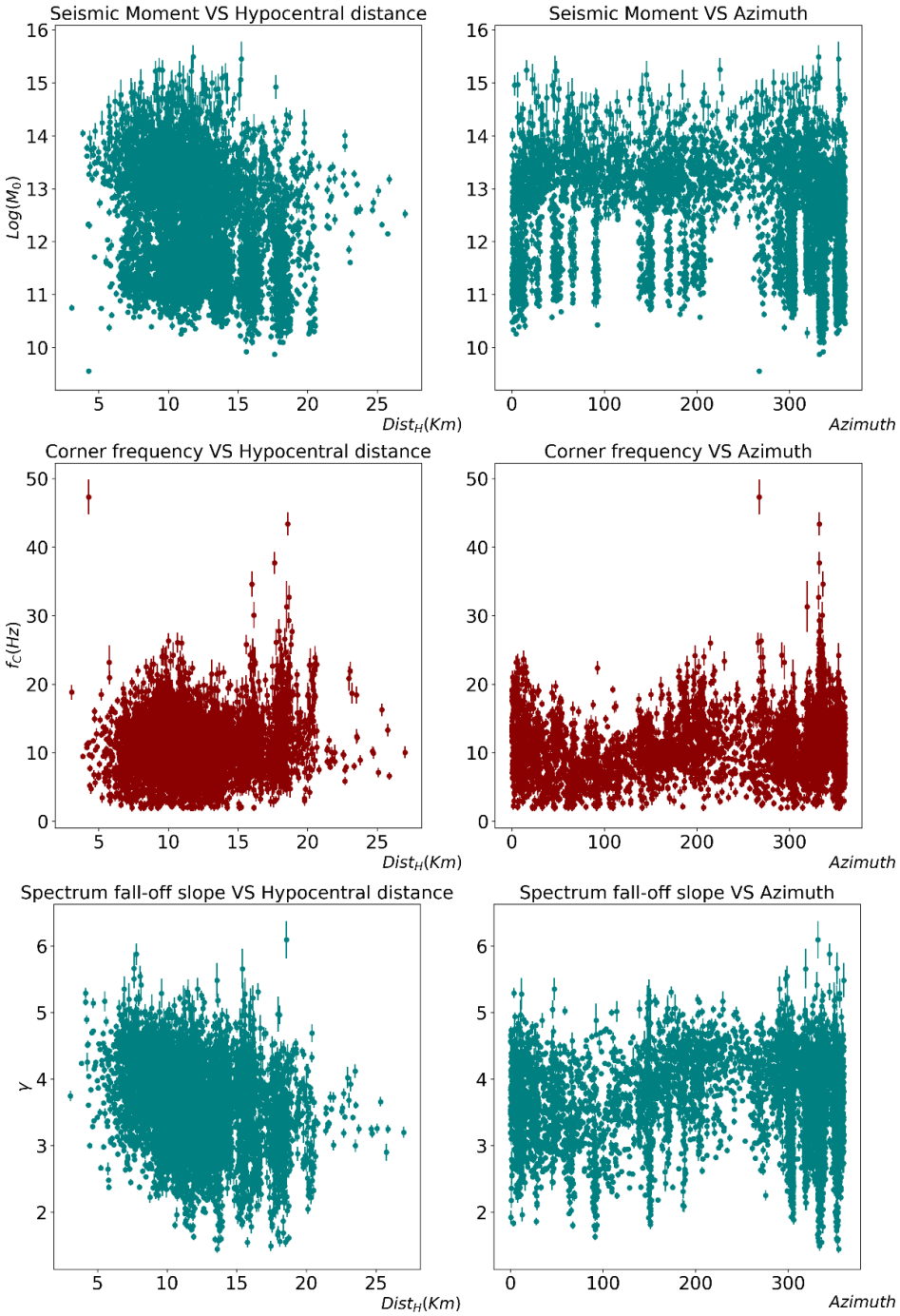

Figure 6.29 Seismic moment, corner frequency and high-frequency decay factor as a function of hypocentral distance (left column) and azimuth (right column), respectively. Here we represent all the retrieved solutions per station, for the whole dataset are represented.

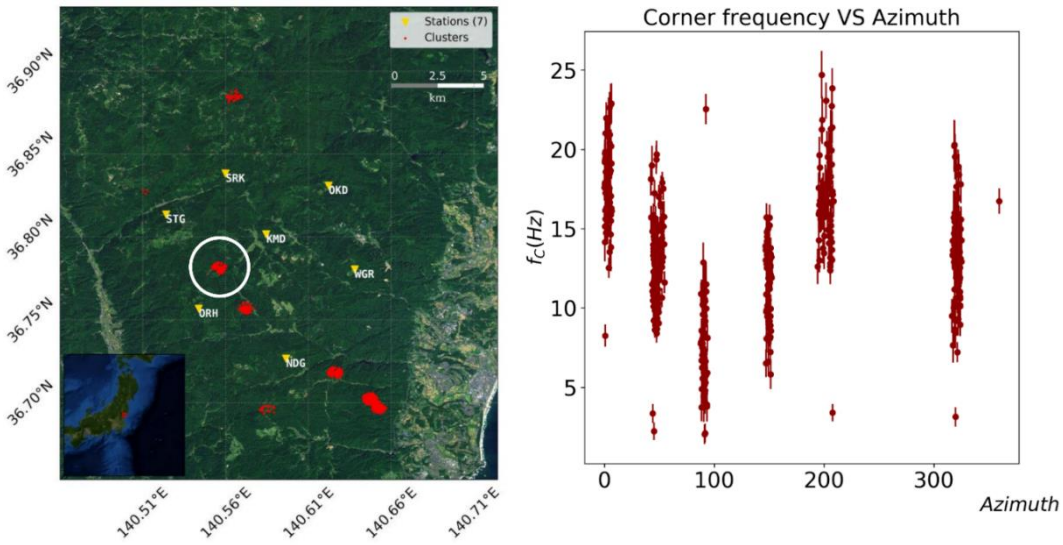

Figure 6.30 Directivity effect on corner frequency. On the left, the selected cluster of events (white circle); on the right, the corner frequency solutions per events as a function of azimuth; we observe a periodicity of π as a directivity effect.

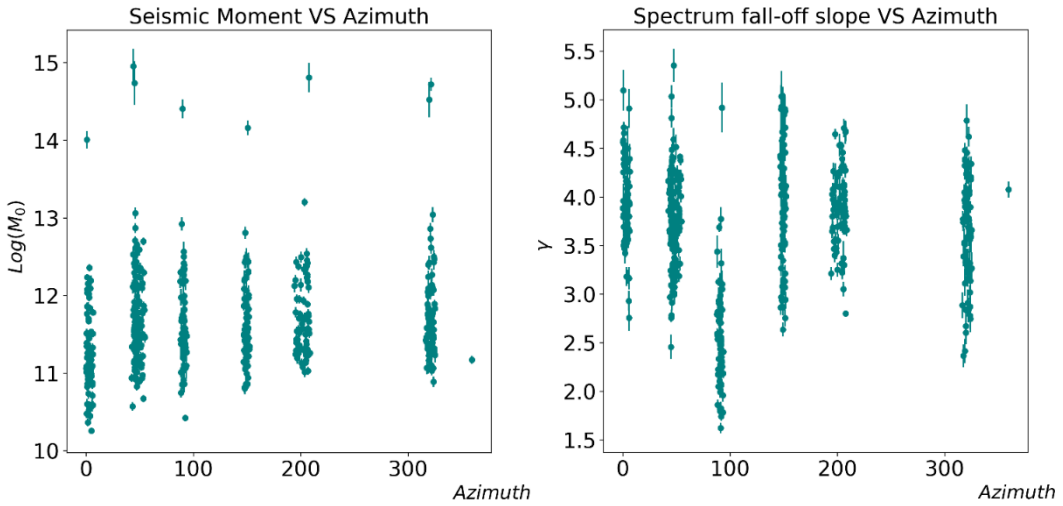

Figure 6.31 Seismic moment and high-frequency decay factor as a function of azimuth for the selected cluster, as shown in Figure 6.30. There is no evidence for a directivity effect, although the γ estimates show a variability.

7. Code implementation

The described methodology has been implemented by the software *SPAR* (*S*ource *PAR*ameter estimator) using Python language (Van Rossum, 1995). Computation relies on Numpy and Scipy libraries (Oliphant, 2007), signal processing on Obspy library (Megies et al., 2011), graphic output on Matplotlib library (Hunter, 2007).

The core function of the method (*PMCF*, *P*robabilistic *M*arkov *C*hain based *F*it) and *SPAR* software are distributed under the GNU GPL v3 copyleft license; at the moment, the software can be obtained by contacting the author.

A flowchart of the software is represented in Figure 7.1; details are given in the following sections.

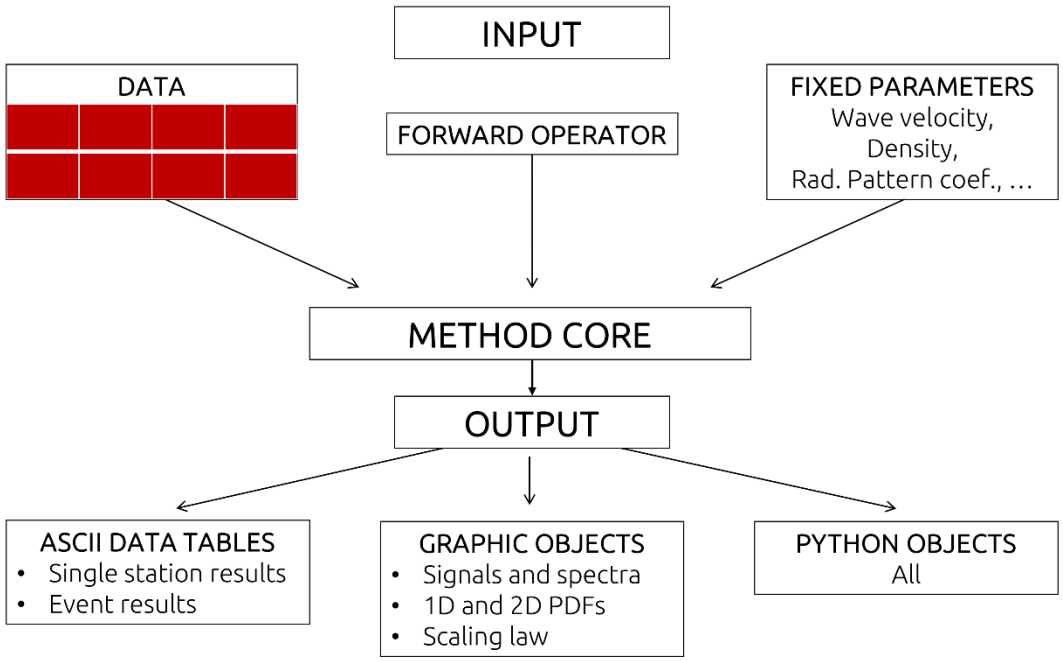

Figure 7.1 Flowchart of the SPAR software.

7.1. Input

The software automatically processes a set of events (dataset), analyzing S- or P-waves. The dataset directory should contain a directory for each event; the name of the directory will be used by the software as the ID of the event. Each event folder should contain the 3-components records (data), that are accelerometric or velocimetric signals, for the available stations, the stations metadata and the event metadata.
Although the software is specifically designed to read data and metadata in SAC file format, both of them are converted into Python's objects through Obspy at the beginning of the processing. Since Obspy can read multiple data and metadata formats (more than 20 file formats, among them MSEED, KNET, WIN, WAV), the software could easily process such file formats.
As input for the processing, the user has to provide information about the propagation medium, indicating the S- or P-wave velocity model, density, crustal shear modulus and the free surface coefficient.
Information on wave arrival times should be provided as metadata, but it is not strictly required : theoretical arrival times can be also computed by the software.

7.2. Data parallelism

Parallel computing allows to solve a large problem splitting it into smaller ones, solved simultaneously. This could dramatically reduce the computation time required by a software; this becomes more and more important as the data to be processed increases, that is, as the size of the problem to be solved increases.
Data parallelism has been implemented in *SPAR*, as a consequence of the nature of the problem we want to solve: the software is able to process

separately and simultaneously each event of the dataset, assigning each event to a different CPU of a parallel computing system.
We used the S-CAPAD platform of the IPGP (Institut de Physique du Globe de Paris) to perform the LFEs analysis described in Chapter 5. Thanks to data parallelism, we were able to process the entire dataset (43183 events, 718870 traces) in 52 minutes, running the software simultaneously on 192 CPUs. The required computation time, using an INTEL i5 machine, is larger than 72 hours.

7.3. Output

The output directory contains a subdirectory for each event, named with the event ID. For each station-source couple the produced output is the following :

- Selected signal and noise in time domain (image)
- Noise and signal spectra (image and Numpy object)
- Solution as joint PDF (Numpy object) and marginal PDFs (1-D,2-D and 3-D, as images and Numpy object)
- Results: source parameters and correlation matrix (ASCII table and Numpy object)

For each event, the software produces:

- Spectra for all the stations (image)
- Results for all the station and weighted mean (ASCII table and Numpy object)

8. Performance of Earthquake Early Warning Systems during the 2016–2017 M_W 5–6.5 Central Italy Sequence

Performance of Earthquake Early Warning Systems during the 2016–2017 M_w 5–6.5 Central Italy Sequence

by Gaetano Festa, Matteo Picozzi, Alessandro Caruso, Simona Colombelli, Marco Cattaneo, Lauro Chiaraluce, Luca Elia, Claudio Martino, Simone Marzorati, Mariano Supino, and Aldo Zollo

ABSTRACT

Earthquake early warning systems (EEWSs) are nowadays contributing to seismic risk mitigation actions, both in terms of losses and societal resilience, by issuing an alert promptly after the earthquake origin and before the ground-shaking impacts the target to be protected. In this work, we analyze the performance of network-based and stand-alone (on-site) early warning systems during the 2016–2017 central Italy sequence, characterized by events with magnitude as large as 6.5. For the largest magnitude event, both systems predict well the ground shaking nearby the event source, with a rate of success in the 85%–90% range, within the potential earthquake damage zone. However, the lead time, that is, the time available for security actions, is significantly larger for the network-based system. For the regional system, it increases to more than 10 s at 40 km from the event epicenter. The stand-alone system performs better in the near-source region, still showing a positive albeit small lead time (<2 s). Far away from the source (>60 km), the performances slightly degrade, mostly owing to the large uncertainty in the attenuation relationships. This study opens up the possibility for making an operational EEWS in Italy, based on the available acceleration networks, provided that the delay due to data telemetry has to be reduced.

INTRODUCTION

A devastating and long-lasting earthquake sequence shook central Italy between August 2016 and January 2017, generating about 300 causalities and diffuse damage estimated up to 1.4% of Italy GDP and forcing more than 30,000 people to be displaced from their home, as reported on the Italian civil protection website (Chiaraluce *et al.*, 2017). Until now, the sequence generated more than 1000 events with moment magnitude (M_w) larger than 3.0 (National Institute of Geophysics and Volcanology [INGV] catalog; see Data and Resources). It started with the M_w 6.0 Amatrice earthquake occurring on 24 August 2016, without being preceded by a significant foreshock activity. Then, two months later, an M_w 5.9 event (Visso earthquake) nucleated 20 km north of Norcia. These two earthquakes likely contributed to the development of the largest magnitude event (M_w 6.5 Norcia earthquake), which occurred on 30 October 2016. This event ruptured an about 40-km-long fault bridging the seismic gap left from the previous two earthquakes, partially extending over regions already hit by the previous seismicity (Chiaraluce *et al.*, 2017). The last event of the sequence occurred south of Amatrice, on 18 January 2017 (M_w 5.5 Montereale earthquake).

This sequence affected a sector of the central Apennines bounded at north by the 1997 Umbria–Marche sequence and at south by the 2009 L'Aquila earthquake. The ruptures associated with the seismic events almost covered the whole area between the two regions except for a 15–20-km-long segment, north of L'Aquila, that may still represent a seismic gap, thus increasing the potential to generate in this area an $M_w > 5.5$ event in the future. From the aftershock distribution, the sequence occurred along a segmented normal fault system with an along-strike extension of about 70 km (Chiaraluce *et al.*, 2017). The rupture of the main events reached the surface with a significant slip (larger than 30 cm for the Amatrice event and 2 m for the mainshock), along an about 20-km-long trace on the Monte Vettore region (Livio *et al.*, 2016; Emergeo W.G. *et al.*, 2016; Pucci *et al.*, 2017). Kinematic inversions of the main events obtained from geodetic and/or strong-motion data revealed localized slip patches, with maximum slip reaching 1 m for the M_w 6.0 Amatrice event (Tinti *et al.*, 2016; Liu *et al.*, 2017) and about 2 m for the M_w 6.5 Norcia earthquake (Chiaraluce *et al.*, 2017; Liu *et al.*, 2017). The presence of localized slip together with fast rupture propagation enhanced both along-strike and up-dip directivity effects, as it can be recognized in the ground-motion distribution (Liu *et al.*, 2017; Picozzi *et al.*, 2017) and in the pulse-like signature of the near-source waveforms (Iervolino *et al.*, 2016).

For this study, we selected nine events, representing the earthquakes with magnitude larger than 5.0; this threshold yields good signal-to-noise ratio (SNR) at accelerometers within ~100 km from the hypocenters. The list of events is

doi: 10.1785/0220170150

Table 1
Earthquake Parameters for the 2016–2017 Central Italy Dataset (see Data and Resources)

Event Number	M_w	Origin Time (yyyy/mm/dd hh:mm:ss)	Latitude (°N)	Longitude (°E)	Depth (km)	Number of Stations
1	6.0	2016/08/24 01:36:32	42.6983	13.2335	8.1	169
2	5.4	2016/08/24 02:33:29	42.7922	13.1507	8.0	146
3	5.4	2016/10/26 17:10:36	42.8802	13.1275	8.7	172
4	5.9	2016/10/26 19:18:06	42.9087	13.1288	7.5	181
5	6.5	2016/10/30 06:40:18	42.8322	13.1107	9.2	171
6	5.1	2017/01/18 09:25:42	42.5468	13.2623	9.2	138
7	5.5	2017/01/18 10:14:12	42.5293	13.2823	9.1	148
8	5.4	2017/01/18 10:25:26	42.4943	13.3112	8.9	136
9	5.0	2017/01/18 13:33:37	42.4773	13.2807	10	142

reported in Table 1. Although a regional earthquake early warning system (EEWS) was under testing at the INGV during the sequence, we cannot directly analyze the associated real-time performances. Indeed, the current seismic networks in central Italy are not designed to support an early warning (EW), owing to latency in data packeting, to data transmission without controlled delay, and to stations sending data in trigger mode, after the event detection (for sake of comparison, the telemetry at the Irpinia Seismic Network [ISNet] accelerometric network in southern Italy has been specifically designed for real-time data transmission and the associated delay is smaller than 1 s; e.g., Satriano *et al.*, 2011). For this reason, we analyzed the performances by playing backthe waveforms in the EEWS, as they were acquired in real time, with a maximum latency, due to data packeting, of 1 s and no transmission delay, thus corresponding to a nearly optimal situation for evaluating the system performances.

EEWSs are real-time-controlled systems that process the seismic signals radiated by an earthquake rupture while it is still evolving; they predict the ground shaking at selected target sites and they possibly pilot automatic actions aimed at protecting people and machineries, thus facilitating the postevent resilience of struck communities or industrial plants. These systems analyze the early portion of the *P*-wave to forecast the *S*-wave shaking both at near-fault locations and at farther sites. EEWSs are typically classified in two approaches: regional (or network-based) and on-site (or stand-alone) systems. A regional system uses dense strong-motion networks surrounding faults known as potential seismic threats, and it is aimed at detecting, locating, and estimating the size of an earthquake from the analysis of the first few seconds of the *P*-wave record. Then, they predict the expected ground motion at targets through empirical ground-motion prediction equations (GMPEs; Allen and Kanamori, 2003; Zollo *et al.*, 2006). Earthquake size estimation from regional EEWS may saturate when limiting the analysis to a fixed *P*-wave time window (Zollo *et al.*, 2006; Festa *et al.*, 2008). Saturation can be avoided when expanding the *P*-wave time window (Colombelli, Zollo, *et al.*, 2012) or following the growth of the strong-motion data from the *P*-wave onset (Colombelli *et al.*, 2014). A relevant EW parameter is the lead time, that is, the time available for emergency actions after issuing the alert. It depends on the distance between the earthquake source and the site to protect. The lead time is negative for sites located nearby the earthquake epicenter, defining the blind or no warning zone, whose size depends on geometrical (i.e., network density and epicenter-to-target distance) and technological (i.e., telemetry and computational time) parameters. It is as large as 25–30 km for standard dense networks in near-fault observatories (Satriano *et al.*, 2011; Picozzi *et al.*, 2015). Despite this limitation, however, several network-based EEWSs are operational worldwide (e.g., in Romania, United States, Mexico, and Japan). The experimentation of seismic EW in Italy is limited to a pilot testing phase in southern Italy, where the system uses the ISNet (Iannaccone *et al.*, 2010) as the backbone monitoring infrastructure.

On-site systems are based on one or more seismic sensors installed at the site to be protected, where early *P*-wave signals are analyzed to predict the following shaking caused by *S* and surface waves through empirical amplitude-scaling relationships defined at a regional level (Kanamori, 2005; Zollo *et al.*, 2010). Although the estimation of source parameters from stand-alone systems is less robust and accurate than for network-based systems, they usually provide reliable predictions for the peak ground-motion parameters, and they provide a nonnegative lead time for targets located close to the fault. Such systems usually operate in trigger mode, issuing the alert based on predefined thresholds, calibrated on the ground-motion intensity (Wu and Kanamori 2008; Zollo *et al.*, 2010; Colombelli *et al.*, 2015).

In this study, we evaluated the performances of both the network-based PRobabilistic and Evolutionary early warning SysTem (PRESTo) v.1.0 (Satriano *et al.*, 2010) and the stand-alone on-Site-Alert-leVEl (SAVE) v.1.0 (Caruso *et al.*, 2017) EEWS on the main events of the central Italy sequence. In the Data and Methods section, we describe the selected dataset in terms of events and stations and summarize the primary features of the two systems. Then, we discuss the performances of the two EEWSs, both for the M_w 6.5 Norcia earthquake and considering all the selected events. The performance analysis is based on the correct estimation of the strong-motion parameters and on the available lead time as a function of the distance

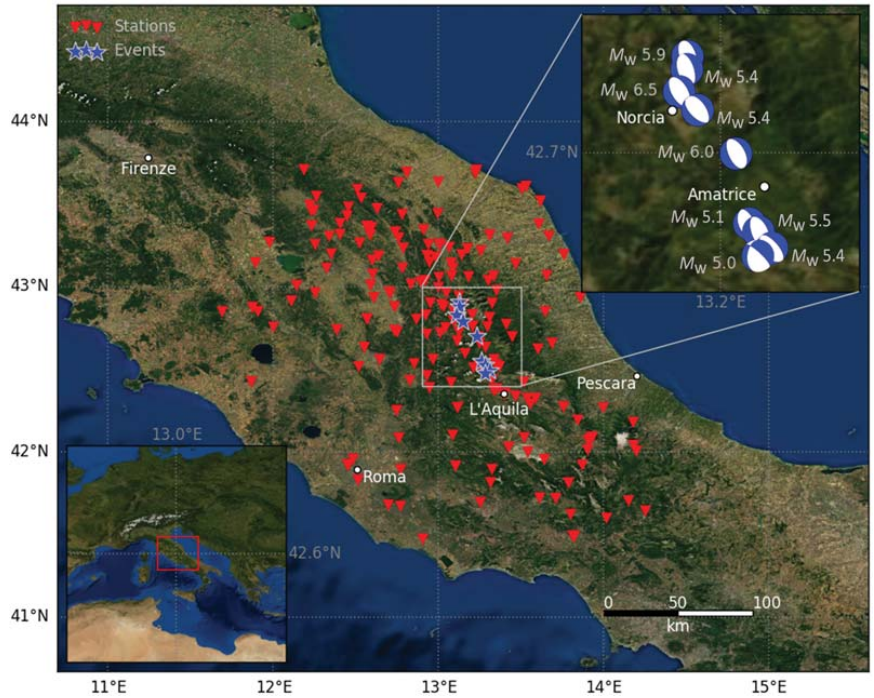

▲ **Figure 1.** Map of the accelerometric stations from Civil Protection Department and National Institute of Geophysics and Volcanology (INGV, red triangles) and earthquakes of the 2016–2017 central Apennines sequence with $M_w \geq 5$ considered in this study (blue stars). In the upper inset, details about earthquake location, focal mechanism, and moment magnitude are shown (data from INGV network, Engineering Strong Motion database; see Data and Resources).

from the earthquake epicenters. In the case of the network-based system, we also compare the location and the magnitude estimated by the EEWS with the reference values.

DATA AND METHODS

The dataset considered in this study consists of nine earthquakes with M_w larger than 5.0, occurred in the central Italy region from 24 August 2016 to 18 January 2017 and recorded by ~200 accelerometric stations located at epicentral distances in the 10–130 km range. The acceleration records were retrieved from the Engineering Strong Motion database (Luzi *et al.*, 2016), which freely distributes strong-motion data from earthquakes that have occurred in the European–Mediterranean and the Middle East regions.

For each event, we selected unprocessed acceleration waveforms from all the available stations in the selected distance range. The stations belong to the Italian Strong Motion Network (Rete Accelerometrica Nazionale [RAN]), operated by the Italian Department of Civil Protection, and to the Italian National Seismic Network, operated by the INGV. The list of events with the associated source parameters and the number of stations that recorded these events is reported in Table 1. In Figure 1, the areal distribution of events and stations is shown. In the epicentral area, the station coverage is very dense, with an average interstation distance of about 10 km.

Network-Based EEWS

We used PRESTo as the network-based EEWS to evaluate the performances. PRESTo is a free and open-source platform (see Data and Resources; Iannaccone *et al.*, 2010; Satriano *et al.*, 2011). The system processes in real time the continuous accelerometric data streams from a seismic network and, after the event detection, it promptly provides probabilistic and evolutionary estimates of location and magnitude, as well as the ground-shaking prediction at target sites through GMPEs. Furthermore, during an event, PRESTo v.1.0 delivers messages to target sites containing all relevant earthquake parameters before the arrival of destructive waves, to enable automatic safety procedures, accomplishing the goal of an EEWS.

PRESTo v.1.0 implements the following components: (1) the phase detector and picker algorithm Filter Picker (Lomax *et al.*, 2012), which picks the *P*-wave first arrival; it is optimized for real-time seismic monitoring and EW; (2) the location algorithm RTLoc (Satriano *et al.*, 2008), which locates earthquakes exploiting both triggered and not-yet-triggered stations; it provides a fully probabilistic description of the hypocenter coordinates and origin time; (3) the algo-

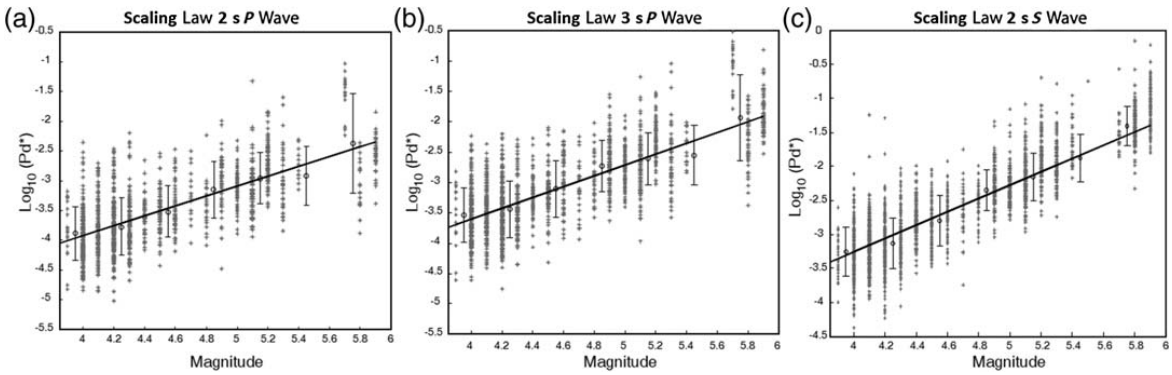

▲ **Figure 2.** Scaling relationships between the peak displacement measured on (a) 2 s and (b) 3 s of *P* wave and (c) 2 s of *S* wave and the final event magnitude. To compare all data in the same plot, the peak displacement values have been computed to the reference distance of 10 km and they are referred in the graphs to as Pd*.

rithm for estimating the magnitude RTMag (Lancieri and Zollo, 2008), which is based on a Bayesian approach and uses the peak displacement measured on the first seconds (2 and 3 s of *P* wave and 2 s of *S* wave) of the high-pass-filtered signal, with a cutoff frequency of 0.075 Hz; the final earthquake magnitude is obtained through empirical correlation laws based on early *P* and *S* peak displacement values; and (4) GMPEs for estimating the peak ground motion (i.e., peak ground velocity [PGV] and peak ground acceleration) at target sites and at seismic stations using the real-time evolutionary estimates of location and magnitude.

PRESTo v.1.0 is currently running in real time, collecting and analyzing data from ISNet since 2009 (Iannaccone *et al.*, 2010). Real-time testing is also underway in South Korea on the Korean Institute for Geoscience and Mineral Resources (KIGAM) network, in Romania on the Romanian Seismic Network (RoNet; National Institute of Research and Development for Earth Physics), in the Marmara region (Turkey) on the Kandilli Observatory and Earthquake Research Institute (KOERI) network, and in a transnational region including northeast Italy, Slovenia, and Austria at the Istituto Nazionale di Oceanografia e Geofisica Sperimentale center. The calibration of the empirical laws between peak displacement and earthquake magnitude (M_w) used in this study has been carried out using a dataset of about 5000 accelerometric records from the RAN related to the largest earthquakes ($M_w > 4$) that occurred in Italy during the period 1997–2013 and available through the ITalian ACcelerometric Archive 2.0 (Pacor *et al.*, 2011; see Data and Resources). The dataset includes recordings that span hypocentral distances from 10 to 300 km, and magnitudes M_w from 4.0 to 6.3, with most of the hypocentral distances smaller than 60 km. Furthermore, the dataset includes the mainshock and the largest aftershocks of the M_w 6.3 L'Aquila and the M_w 5.9 Emilia earthquakes, which occurred in April 2009 and May 2012, respectively. The results of the best-fit regression analysis for the *P* waves (i.e., 2 and 3 s) and *S* waves (i.e., 2 s) windows are as follows:

$$2\ \mathrm{s}(P_{\mathrm{wave}}):\ \log(\mathrm{Pd}_P) = -7.26(\pm 0.90) + 0.83(\pm 0.18)M_w - 1.57(\pm 0.05)\log(r/10);\quad \sigma = 0.51;\ R^2 = 0.96$$

$$3\ \mathrm{s}(P_{\mathrm{wave}}):\ \log(\mathrm{Pd}_P) = -7.17(\pm 0.83) + 0.89(\pm 0.17)M_w - 1.91(\pm 0.05)\log(r/10);\quad \sigma = 0.47;\ R^2 = 0.96$$

$$2\ \mathrm{s}(S_{\mathrm{wave}}):\ \log(\mathrm{Pd}_S) = -7.18(\pm 0.55) + 0.98(\pm 0.12)M_w - 1.19(\pm 0.03)\log(r/10);\quad \sigma = 0.36;\ R^2 = 0.98,$$

in which r is the hypocentral distance in kilometers, Pd_P and Pd_S are measured in meters, σ is the standard deviation on the $\log(\mathrm{Pd}_X)$ estimate, and R is the correlation coefficient. In Figure 2, we show the best-fit curves superimposed to the data; to compare observations collected at different hypocentral distances, the peak displacement is reduced to an equivalent distance of 10 km, according to the above relationships. Figure 2a, 2b, and 2c corresponds to the best-fit solutions for 2 and 3 s of *P* wave and 2 s of *S* wave, respectively.

Finally, the GMPEs are derived from strong-motion records of 131 earthquakes that occurred in Europe and in the Middle East with moment magnitudes ranging from M_w 5 to 7 (Akkar and Bommer, 2007).

Stand-Alone EEWS

SAVE v.1.0 (Caruso *et al.*, 2017) is used as the stand-alone EEWS for this analysis. It is a *P*-wave-based EEWS that measures in real time the peak displacement (Pd) and the predominant period (τ_c) over time windows of variable length (i.e., 1, 2, and 3 s) after the *P*-phase arrival (Wu and Kanamori, 2008). Thus, it provides the expected ground-shaking intensity at the monitored site, a local alert level (Colombelli, Amoroso, *et al.*,

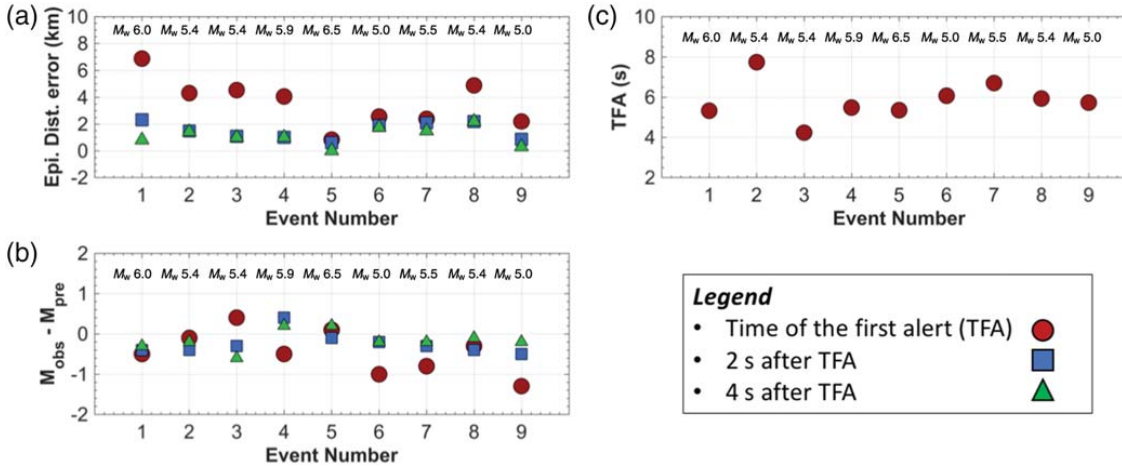

▲ **Figure 3.** (a) Epicentral location error at the time of the first alert (TFA), 2 and 4 s after the TFA. (b) Residuals between observed and predicted magnitude at TFA, 2 and 4 s plus TFA. The error for both location and magnitude is computed as the difference between the estimations provided by PRobabilistic and Evolutionary early warning SysTem (PRESTo) v.1.0 and the values given by the official INGV bulletin. (c) TFA in seconds. This value ranges between 4 and 8 s, with an average value of 6 s.

2012), and a qualitative classification of the earthquake magnitude and of the source–receiver distance. SAVE v.1.0 can operate either at a single station (i.e., a single sensor located at the target site) or with a small set of collocated seismic nodes. Independently of the number of sensors acquired by SAVE v.1.0, the algorithm checks the quality of detected picks and measures the EW parameters Pd and τ_c only if some criteria are fulfilled. Specifically, we require that the SNR, defined as $\mathrm{SNR} = 20\log_{10}(\mathrm{Pd}/\mathrm{PGD}_{\mathrm{noise}})$, is $\mathrm{SNR} > 14$, the following relationship $-0.9 < \log_{10}(\mathrm{Pv}/\mathrm{Pd}) < -0.2$ holds and the data are not clipped (Caruso *et al.*, 2017). In the formulas, $\mathrm{PGD}_{\mathrm{noise}}$ is the peak displacement measured in a 3 s time window before the arrival of the *P* wave and, Pd and Pv are peak displacement and velocity, respectively, recursively measured in time windows of 1, 2, and 3 s after the *P* pick. These conditions ensure that residual baselines in the displacement do not significantly affect the measure of the EW parameters.

The empirical scaling relationships between Pd, τ_c, PGV, M_w, and *R* used by SAVE v.1.0 also have been calibrated on the Italian RAN dataset (Caruso *et al.*, 2017). Similar to PRESTo v.1.0, SAVE v.1.0 delivers alert messages via the Internet whenever a detected event exceeds user-configurable thresholds of the output parameters (e.g., estimated intensity equal to VI or above). The warning message includes the EW parameters calculated by SAVE v.1.0 and their uncertainties. A new message is sent at each change of outputs or whenever a second has passed from the previous message.

RESULTS

Performance of the Network-Based EEWS

We investigated the performances of the regional EEWS by injecting in playback mode the waveforms related to the central Italy earthquakes in PRESTo v.1.0. Results of the analysis are shown in Figure 3. The performance of the system is assessed in terms of its capability to correctly provide the location, the magnitude, and the time of the first alert (TFA), this latter being defined as the instant from the event origin time when five stations have triggered and the PRESTo v.1.0 provided the first estimate of location and magnitude. The error associated with the EW estimates is considered as the difference between the results obtained by PRESTo v.1.0 and those provided by the official INGV bulletin (see Data and Resources). Furthermore, to investigate the stability of the EW estimates, we consider the estimations at TFA, and at this latter quantity plus 2 and 4 s.

Figure 3a and Table 2 show that the error in epicentral location at TFA ranges between 0.8 and 6.9 km, these values being obtained for the M_w 6.5 Norcia and the M_w 6.0 Amatrice earthquakes, respectively. The location error does not show any trend with magnitude and depth (i.e., differences in hypocentral depth among the events are within 2.5 km), suggesting that the observed errors are due to an inherent aleatory variability in the arrival time of the *P* wave at the closest stations. The number of stations for which arrival times were available at TFA varies between 5 and 15 (Table 2). Two seconds after the TFA, the epicentral errors are already very small (i.e., below 2.5 km and on average of about 1.5 km), and they remain almost constant when extending the time to 4 s after the first alert (Table 3). The number of stations included in the analysis 2 s after the TFA ranges between 14 and 30.

Figure 3b presents the results in terms of event magnitude. At the TFA, the magnitude tends, in general, to overestimate the reference values with an average difference of 0.4 magnitude units (mu). Specifically, the largest overestimations are obtained for two M_w 5.0 events (events 6 and 9 with +0.8 and +1.3 mu, respectively). These events show errors in hypocen-

Table 2
PRESTo v.1.0 Performance at the Time of the First Alert (TFA)

Event Number	M_w	Number of Triggered Stations	Δ Time after Origin Time (s)	Blind Zone (km)	Δ Epicentral Location (km)	Magnitude by PRESTo
1	6.0	7	5.3	17.4900	6.9	6.5
2	5.4	5	7.7	25.4100	4.3	5.5
3	5.4	7	4.2	13.8600	4.5	5.0
4	5.9	11	5.5	18.1500	4.0	6.4
5	6.5	15	5.4	17.8200	0.8	6.4
6	5.1	13	6.1	20.1300	2.6	6.1
7	5.5	13	6.7	22.1100	2.4	6.3
8	5.4	5	5.9	19.4700	4.9	5.7
9	5.0	15	5.7	18.8100	2.2	6.3

The symbol Δ represents the absolute value of the difference between the estimation of PRESTo and the bulletin reference values. PRESTo, PRobabilistic and Evolutionary early warning SysTem.

Table 3
PRESTo Performance at the Time of the First Alert (TFA) Plus 2 and 4 s

Event Number	M_w	Δ Epic. TFA + 2 s (km)	Δ Epic. TFA + 4 s (km)	M_w by PRESTo TFA + 2 s	M_w by PRESTo TFA + 4 s
1	6.0	2.3	0.8	6.4	6.3
2	5.4	1.5	1.4	5.8	5.6
3	5.4	1.1	1.0	5.7	6.0
4	5.9	1.0	1.0	5.5	5.7
5	6.5	0.6	0.0	6.6	6.3
6	5.1	1.9	1.7	5.3	5.3
7	5.5	2.1	1.5	5.8	5.7
8	5.4	2.2	2.2	5.8	5.5
9	5.0	0.8	0.3	5.5	5.2

The symbol Δ represents the absolute value of the difference between the estimation of PRESTo and the bulletin reference values.

tral location below 3 km. Therefore, we believe that the anomalous magnitude overestimations could be originated either by the *S*-wave contamination in the selected *P*-wave time window at the closest stations and/or by source effects, such as the radiation of large initial *P*-peak amplitudes generated by relatively high fault slip or stress release in the regions of the fault located nearby the nucleation area. The aftershocks of this seismic sequence presented a quite large variability in the dynamic properties (Picozzi *et al.*, 2017; i.e., apparent stress between 1 and 20 MPa). Large apparent stress (i.e., large rupture speed, large static stress drop, and large slip) might have led to 2 s *P*-wave displacement amplitudes anomalously larger with respect to those expected from the empirical relationships calibrated for Italy. Concerning the three largest events of the sequence, in the case of the M_w 6.0 Amatrice and M_w 5.9 Visso earthquakes, the EW estimates are 0.5 mu larger than the final magnitude, while in the case of the M_w 6.5 Norcia earthquake, the EW estimate agrees very well with the final value, with a difference of −0.1 mu. Two seconds later, the number of stations contributing to the magnitude estimate is greater than 10, and we generally observed an error reduction of 0.2 mu on average (Table 3). At this stage, stations closer to the epicenter contributed with the *S* wave, whereas farther stations provided 2 or 3 s of *P* wave for the magnitude estimate. Finally, 4 s after TFA, the error associated with the magnitude decreases to 0.1 mu (Table 3).

The TFA varies from 4.2 s (i.e., event 3) to 7.7 s (i.e., event 2), with an average value of 5.8 s (Fig. 3c). These values can be used to estimate the radius of the blind zone (BZ) assuming for the *S* wave a constant velocity of 3.3 km/s, which leads to BZs' radii between 14 and 25 km (19 km in average). These estimates are consistent with the results of Picozzi *et al.* (2015), who evaluated the BZ radius based on numerical simulations. Although the computation time is considered in the playbacks, it is here assumed that no latency is due to data telemetry, while a maximum of 1 s of delay is ascribed to data

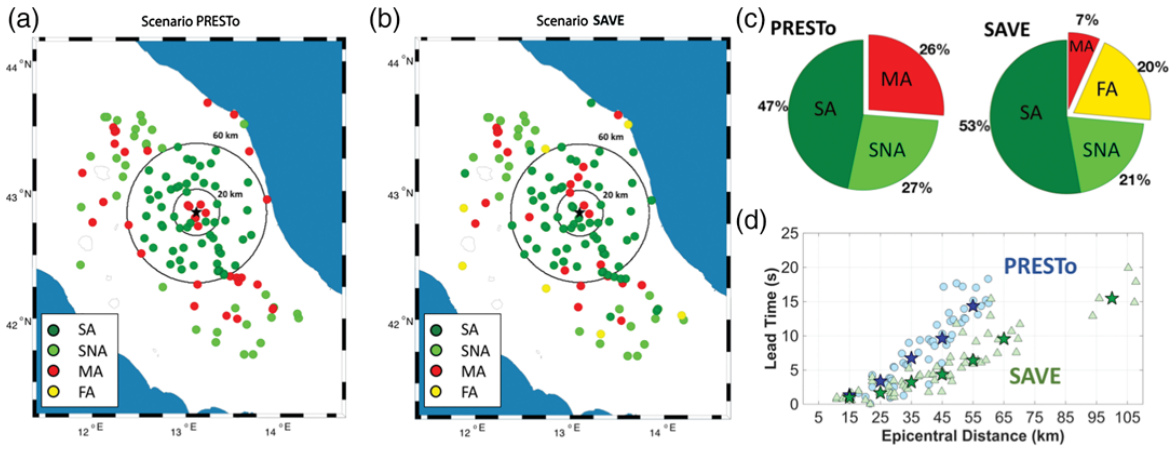

▲ **Figure 4.** Performances of the network-based (PRESTo v.1.0) and stand-alone (on-Site-Alert-leVEl [SAVE] v.1.0) earthquake early warning system (EEWS) for the M_w 6.5 Norcia earthquake. (a) Areal distribution of successful alerts (SA), successful no-alerts (SNA), missed alerts (MA), and false alerts (FA) by PRESTo v.1.0. Circles enclose stations within 20 and 60 km. (b) Areal distribution of SA, SNA, MA, and FA using SAVE v.1.0. (c) Pie charts illustrating the percentage of SA, SNA, MA, and FA for the two systems. (d) Lead time as a function of the distance for PRESTo v.1.0 (blue circles) and SAVE v.1.0 (green triangles). Stars indicate the median value for 10-km-wide distance bins.

packeting. Therefore, the derived values represent the lower bound for the BZ size. They are, however, useful estimates for guidance in assessing the performance of the EEWS given by the integration of PRESTo v.1.0 on the Italian seismic network. In real-time data acquisition mode, the BZ dimension would progressively increase with the increase of delay in data telemetry.

Furthermore, we also evaluated the capability of the system to provide reliable alerts at sites located at an increasing distance from the epicenter. From the user point of view, indeed, an EEWS should provide information about the incoming ground shaking, the possible overcoming of a damage threshold for the buildings, and how much lead time is available to secure people, structures, and industrial machineries against the potential earthquake damage.

To set the ground-motion level of interest, we considered the PGV corresponding to the lower bound of the macroseismic intensity degree VI in the Mercalli–Cancani–Sieberg (MCS) scale (Sieberg, 1930) (light damage and strong perceived shaking), and we exploited the relationships between PGV and MCS intensity recently calibrated for Italy (Faenza and Michelini, 2010) (lower bound of intensity VI corresponds to a PGV of 2.4 cm/s). For each event, we assumed all the available accelerometric stations within 200 km from the epicenter as potential target sites, and we compared the observed PGV with the PGV predicted by PRESTo v.1.0 at TFA (i.e., on the base of the first location and magnitude estimates and using the selected GMPE). An alert is considered a successful alert (SA) when both observed and predicted PGV values are larger than the threshold; we get a successful no-alert (SNA) when both values are below the selected threshold, a false alarm (FA) when the predicted PGV is above while the observed PGV is below the threshold, and finally, a missed alarm (MA) when the observed PGV is above the threshold but not the predicted PGV. It is worth noting that during the playback of all the records, PRESTo v.1.0 never missed the real-time detection of the events. Therefore, the users outside the BZ would have never experienced a missed event detection but eventually an underestimated prediction of the ground-motion severity. Similarly, the meaning of false alert is only caused by an overestimation of the ground shaking. Additionally, because our real-time location and magnitude estimates are consistent with those provided by the INGV bulletin, the performance of the regional EEWS is critically influenced by the prediction capability of the GMPEs.

Concerning the lead time, we computed it as the difference between the instant at which the ground velocity overcomes for the first time the threshold value of 2.4 cm/s and the TFA. It is worth noting that this definition of the lead time is related to the effective arrival of the ground shaking of interest for the EEWS; a more conservative definition, which is also used by other EEWS, is based on the theoretical arrival time of the *S* wave at the target site. Figure 4a shows the performance of PRESTo v.1.0 for the M_w 6.5 Norcia earthquake at TFA using 122 stations with a maximum epicentral distance of 130 km. At this time, four stations with an epicentral distance smaller than 13 km were already hit by a PGV larger than 2.4 cm/s and were thus classified as missed alerts. Between 13 and 16 km, two stations were successfully alerted and two were missed. Beyond 16 km and up to 60 km, where the instrumental intensities estimated by the INGV were between VI and IX (see Data and Resources), all the stations (i.e., 55) received a successful alert. Therefore, in the area experiencing a severe ground motion, the EEWS rated 90.5% of successful alerts

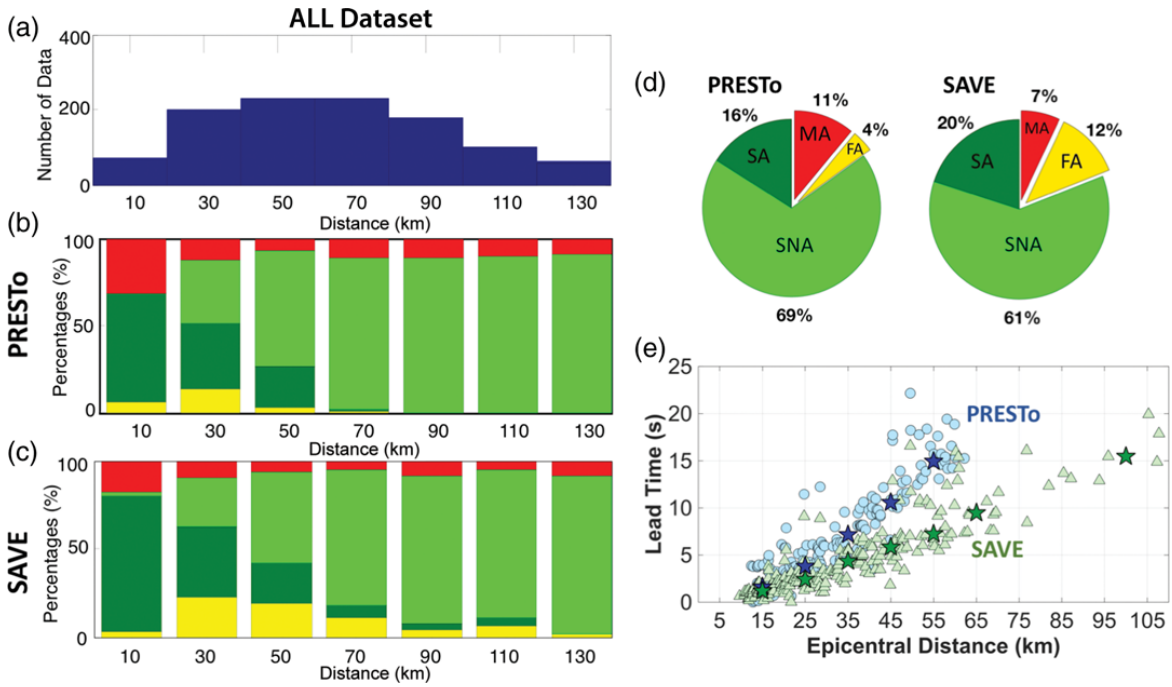

▲ **Figure 5.** Overall performances of the network-based (PRESTo v.1.0) and the stand-alone (SAVE v.1.0) EEWS. (a) Histogram of the number of available stations as a function of the distance; (b) rate of SA, SNA, MA, and FA using PRESTo v.1.0 as a function of the distance. (c) Rate of SA, SNA, MA, and FA using SAVE v.1.0 as a function of the distance. (d) Pie charts illustrating the percentage of SA, SNA, MA, and FA for the two systems. (e) Lead time as a function of the distance for PRESTo v.1.0 (blue circles) and SAVE v.1.0 (green triangles). Stars indicate the median value for different distance bins.

and 9.5% of missed alerts, the latter percentage representing the stations within the BZ. Then, for larger epicentral distances (i.e., between about 60 and 134 km), 33 stations were correctly alerted and classified as SNA, whereas 32 stations resulted as MA. For this external area, where the instrumental intensity was estimated between V and VI, almost 50% of the MA can be likely attributed to local site conditions which have led to small fluctuations of the observed PGV, or to large amplitude surface waves, in both cases resulting in jumps between intensity V and VI with respect to the intensities predicted by the GMPEs. A confirmation of our observations comes also from the macroseismic survey of the epicentral area (Arcoraci *et al.*, 2016), which is not based on the PGV and shows intensities equal or larger than VI limited to about 40 km from the epicenter. Therefore, our performance rule is probably strongly conservative, by assigning MA at large epicentral distances (i.e., beyond 60 km) if we consider that damages were not observed at villages nearby these stations. Globally, the performance of the system is: 47% of SA, 27% of SNA, and 26% MA, with a total rate of success of 74% (i.e., SA plus SNA; Fig. 4c).

Figure 4d shows the lead time computed for the stations with a predicted PGV larger than the selected threshold. We observe that within 20 km from the epicenter the lead time is very short (< 1 s). However, beyond 20 km it rapidly increases to values that would allow trained users to duck and cover: the mean lead-time ranges from 3.5 s between 20 and 30 km to 14.5 s between 50 and 60 km. If we had computed the lead time as the difference between the theoretical arrival time of the *S*-wave arrival time and the TFA, we would have obtained a decrease of the lead time of about 1 s at 45 km and 2 s at 60 km.

When the performance of PRESTo v.1.0 is evaluated over all the selected events, the number of tested station–event pairs raises to 1070, with about 70 pairs within 20 km from the epicenter and an average of about 200 pairs for all the other 20 km wide bins up to 80 km from the epicenter (Fig. 5a). The number of SA decreases with the epicentral distance (i.e., from about 62% between 0 and 20 km to about 22% between 40 and 60 km; Fig. 5b), but the difference is mainly compensated by the number of SNA. Considering SA plus SNA, the correct alerts oscillate between 74% in the 20–40 km range and 88% in the 80–100 km range.

Concerning the false and missed ground-motion predictions, we observe that most of the false detections occur between 30 and 50 km from the epicenter, with a rate of 13%. Instead, the largest portion of MA is concentrated within the 20 km from the epicenter (i.e., 32%), while it decreases to about 12% up to 140 km. The global performance as shown in Figure 5d confirms these results, with correct alerts (i.e., SA

plus SNA) in the 85% of cases, 11% of MA, and 4% of FA. Again, outside the BZ, most of FA and MA owe to the large uncertainty in the GMPEs. Similarly to the Norcia event, the median value of the available lead time (Fig. 5d) is about 3.5 s at 25 km, 7 s at 35 km, 10 s at 45 km, and more than 15 s above 55 km.

Performance of the Stand-Alone EEWS

The performance of the stand-alone EEWS was evaluated by running the software SAVE v.1.0 on the same strong-motion dataset used for the regional analysis. The performance is assessed through the capability of the system to correctly predict the expected ground motion at the sites to be secured. To be directly comparable with the results from the network-based system, we assume that the EEWS issues an alert when the predicted PGV > 2.4 cm/s. Then, we compared the predicted intensity with the observed one and used the same four classes as defined before (SA, SNA, MA, and FA) to assess the performances. Playing back the strong-motion data, SAVE v.1.0 also recognized all the events in the database; again, the notion of false and missed alerts is thus associated with a wrong estimation of the strong-motion severity.

Figure 4b shows the performance of the on-site system for the M_w 6.5 Norcia earthquake. Results are represented in a map to be directly comparable with the outcomes of the regional system, although predictions of the on-site system are evaluated independently station by station. Up to 60 km, almost all stations received an SA, except for two stations located within 15 km from the epicenter, where the ground velocity overcomes the threshold (2.4 cm/s) before issuing the alert, and for four stations located northward of the epicenter, along the fault strike direction. These stations might have experienced possible source effects, likely due to focal mechanism and directivity, or near-field dominated waveforms, which produced a deviation from the average Pd–PGV scaling. Our hypothesis is corroborated by the macroseismic survey (Arcoraci *et al.*, 2016), which provided higher damage levels for villages distributed along-strike direction than for villages in other directions.

Close to the isoseismal VI curve, several targets experienced both MA and FA, with a difference of one unit between the predicted and observed intensities. Most of these results can be attributed to fluctuations related to the discretized intensity scale and to site and source effects around the PGV threshold value of 2.4 cm/s. The final performance of the on-site system is 53% of SA, 21% of SNA, 20% of MA, and 6% of FA. Comparing the percentage of SA and SNA, the performance of the stand-alone system is comparable with that of the regional system.

In Figure 4d, the lead time for the stand-alone system is superimposed to the lead-time estimation for the network-based system for the M_w 6.5 Norcia earthquake. A positive lead time is still available for the closest stations within the first 20 km, albeit very short (< 2 s). Then, its median value increases from about 2 s between 20 and 30 km to about 7 s between 50 and 60 km. The overall values of the lead time for an on-site system are smaller than the ones for the regional system, the former growing with the difference between the *S*- and *P*-wave slowness, the latter increasing with *S*-wave slowness.

Figure 5c finally summarizes the performances for all the events in the sequence. Within 30 km from the epicenter, the system reported the 77% of SA/SNA. The larger portion of MA (i.e., 11%) is concentrated within 20 km from the epicenter, whereas most of FA (i.e., 20%) occurs between 20 and 60 km. The statistics over the entire range of distances confirms the high rate of SA/SNA (i.e., 81%), whereas MA and FA rates are 7% and 12%, respectively (Fig. 5d). The lead time increases from few seconds (< 2 s) in the near-source range (< 15 km), to 4 s at 35 km, and above 7 s beyond 55 km (Fig. 5e).

DISCUSSION

The offline application of stand-alone and network-based EEWS to the central Italy sequence enhanced several strong points related to the usability and robustness of earthquake EW in Italy; however, this analysis does not include latency due to data telemetry. The high density of the accelerometric network in the epicentral area enabled the rapid event detection and characterization with regional alerts issued 4–8 s after the event origin time. This corresponds to a BZ with a radius of 15–25 km centered at the epicenter. Outside the BZ, the network-based system predicts well the impending ground shaking by assessing the potential damage area with a rate of success around 90%. While the earthquake location and magnitude are accurately estimated by analyzing the early portion of the *P* wave at the stations close to the epicenter, differences between predicted and observed intensities and PGV mainly owe to the uncertainty in the GMPEs. Although the epistemic variability was already reduced using GMPEs calibrated for this specific area, further improvement can come from accounting for specific source and site effects.

The stand-alone system can provide event information within a still positive lead time in the BZ of the network-based system, although the available time is very short (< 2 s). Within this region, triggering security actions becomes challenging. The overall performance of the on-site system is slightly worse than that of the regional system (rate of success at about 80%). When looking at the alert maps of the Norcia earthquake (Fig. 4a,b), both systems correctly predict the expected ground-shaking intensity within 60 km from the epicenter, and the two maps also almost superimpose far away from the event epicenter. Stand-alone systems show a large rate of false alerts, while reducing the number of missed alerts at large distances from the source. At large distances, the PGV is associated with the arrival of surface waves, which are not taken into account by the adopted GMPEs, while their amplitude can be partially captured by analyzing the early evolution of the *P* wave at the same site.

Although both systems provide equivalent results in terms of rate of success of predicting the ground-shaking intensity, the lead-time distribution shows significant differences and

it increases faster for the network-based system, ranging from 5 to 15 s between 30 and 55 km from the event epicenter. The lead time almost halves for the on-site system in the same distance range, making the latter system less effective on average for this area. Considering the potential social benefit of an EEWS, it is worth noting that, taking into consideration the ring between 30 and 55 km from the epicenter, 5–15 s of available lead time could have been utilized for implementing seismic risk and exposure mitigation actions in 168 municipalities affecting about 700,000 inhabitants. The beneficial effects of an EEWS in this area are even more evident if we consider that the potential end users experienced a six-month-long seismic sequence.

Improvement of site models can reduce epistemic variability in the ground-shaking prediction of regional systems, accounting for velocity, attenuation, and nonlinear rheology in the shallow layers beneath the station, and offsets in the ground-motion parameters at the site with respect to the selected GMPEs (e.g., Abrahamson and Bommer, 2005). Although site effects are intrinsically accounted for in the on-site systems, local discrepancies at specific sites need to be further investigated because the site response to the *P* wave could not linearly change with the response to the *S* wave.

The real-time evaluation of source parameters such as fault geometry, size, directivity, and focal mechanism requires the development of new methodologies, for the evolutionary inversion of the extended source properties. Some techniques were already proposed to improve the source description while the earthquake is still ongoing (Yamada and Heaton, 2008; Böse *et al.*, 2012; Colombelli *et al.*, 2013). Stand-alone systems account for some of the source parameters, such as reduced Joyner–Boore distance due to rupture finiteness. They also track the source directivity through the *P* wave, although it is less enhanced than for *S* wave, because it depends on the ratio between the earthquake rupture and the propagation wave velocities. Finally, the effect of the focal mechanism is not accounted for in the on-site systems, because at the same site larger *P*-wave amplitudes are not always followed by larger *S*-wave amplitudes. In this specific case, the M_w 6.5 Norcia event grew along a 40-km-wide normal fault, with significant slip release in the hypocentral area (a concentrated asperity with slip larger than 2 m), a pretty fast rupture moving to the surface (rupture speed of 2.7 km/s) and large coseismic slip at the surface (Chiaraluce *et al.*, 2017). These features can be the source of some missed alerts in the near-source domain, especially in the footwall of the fault.

A complementary data-driven approach for EEWS to improve ground-shaking prediction is to integrate on-site and regional EEWS in real time to produce an evolutionary ground-shaking map. Such a system should initially combine GMPE-based regional estimates of ground-motion parameters with on-site predictions to define the areal distribution of the ground-motion severity. Then, the maps should be continuously updated as the effective ground motion starts to be collected at the stations close to the epicenter. Integration of network-based and stand-alone systems started to be developed through the definition of the potential damage zone (Colombelli, Amoroso, *et al.*, 2012) and the software QUAKEUP (Zollo *et al.*, 2017), although several issues remain open, such as the separation of *P*- and *S*-wave contributions in the data.

Finally, all results presented here do not account for the delays due to the actual dataloggers and telemetry currently deployed in the seismic networks. Since July 2015, PRESTo v.1.0 is running at the Near Fault Observatory TABOO, located above the Alto Tiberina fault, about 60 km north of the region interested by the sequence. This experimentation was promoted in the framework of the European Plate Observing System - Implementation Phase (EPOS-IP) project. In a parallel installation, PRESTo v.1.0 also run on a part of the INGV national network located in the central Italy, whose data are streamed in real time to the control center of Ancona. For this system, an event is declared if six picks occur within 3 s. The system also worked during the initial part of the sequence, before the M_w 6.5 Norcia earthquake. It provided an alert during the Amatrice earthquake 11.4 s after the first *P* pick and 14.3 s after the origin time. The first estimated location was very close to the one released by the INGV bulletin (error in the epicentral location <2 km), while the magnitude was underestimated by 0.2 mu, the system provided an initial M_w 5.8. The final estimation from PRESTo v.1.0 was instead M_w 6.1. The large delay in the alert was due to the latency in data packeting (2–3 s), in the data transmission (up to 20 s for some stations connected to the control center via satellite), and in the data quality (signal clipping).

Diverse results were obtained for the two 26 October 2016 Visso earthquakes. For the M_w 5.4 event, location and magnitude were close to the reference values from bulletin ones, providing the first alert 6.3 s after the initial *P* pick, and thus 9.0 s after the origin time. For the M_w 5.9 event, alert release was comparable with the previous event, but the magnitude was largely underestimated at the TFA. This was mainly due to the clipping of velocimeter sensors near the epicenter and to the underestimation of the hypocentral depth, which prevented the system from using larger *P*-wave windows due to a supposed *S*-wave contamination. The biased magnitudes required several seconds to be partially balanced by the information coming from the rest of the network. On the other hand, the use of velocimeters was justified in the testing phase needing as much station density as possible because the initial plan was to process smaller size earthquakes during the experimentation at the near-fault observatory.

CONCLUSIONS

In this study, we investigated the performances of the network-based and the stand-alone EW systems on the central Italy sequence, playing back accelerometric data into the systems as they were recorded in real time. We found that the ground-shaking intensity was well predicted by both systems. Within 60 km from the event epicenter, the success rate of both EEWSs ranges between 85% and 90% for the main event of the sequence and is ~80% when considering all the events with magnitude larger than M_w 5.0 in the whole epicentral distance

range (< 130 km). Some missed alerts correspond to sites located within the BZ for which the radius on average is 20 km. The size of the BZ is significantly smaller than the size of the region where damages were reported for the M_w 6.5 earthquake (radius of about 40 km). The lead time for the regional system increases from 5 s at 30 km to 15 s at 55 km, allowing to trigger automatic security actions. These values halve for the on-site system, making this latter less effective for the area.

With this study, we show that an operational EEWS in central Italy might effectively contribute to mitigate the seismic risk during an earthquake and enhance postevent resiliency, provided that the delay due to telemetry and data packeting is significantly reduced.

DATA AND RESOURCES

Accelerograms used in this study were collected from the Italian Accelerometric Archive (ITACA) 2.0 (Pacor *et al.*, 2011) at http://itaca.mi.ingv.it (last accessed August 2017). Analysis and plots were made using MATLAB (https://it.mathworks.com/, last accessed August 2017). The Istituto Nazionale di Geofisica e Vulcanologia [INGV] catalog is available at http://cnt.rm.ingv.it (last accessed August 2017). PRESTo is a free and open-source platform, available at www.prestoews.org (last accessed October 2017). For the instrumental intensities estimated by the INGV, see http://shakemap.rm.ingv.it/shake/8863681/intensity.html (last accessed July 2017). For INGV network, see http://cnt.rm.ingv.it/instruments/network/IV (last accessed September 2017); for Engineering Strong Motion (ESM) database, see http://esm.mi.ingv.it/ (last accessed July 2017).

ACKNOWLEDGMENTS

The authors are grateful to Associate Editor Brendan Crowell and two anonymous reviewers that helped in improving the article. Real-time testing of the regional earthquake early warning system (EEWS) at the Near-Fault Observatory TABOO was organized in the framework of the EPOS-IP project. EPOS-IP has received funding from the European Union's HORIZON 2020 with Project ID 676564.

REFERENCES

Abrahamson, N. A., and J. J. Bommer (2005). Probability and uncertainty in seismic hazard analysis, *Earthq. Spectra* **21,** no. 2, 603–607.

Akkar, S., and J. J. Bommer (2007). Empirical prediction equations for peak ground velocity derived from strong-motion records from Europe and the Middle East, *Bull. Seismol. Soc. Am.* **97,** no. 2, 511–530.

Allen, R. M., and H. Kanamori (2003). The potential for earthquake early warning in southern California, *Science* **300,** 786–789, doi: 10.1126/science.1080912.

Arcoraci, L., F. Bernardini, R. Camassi, C. Castellano, S. Del Mese, E. Ercolani, A. Fodarella, L. Graziani, M. Locati, A. Maramai, *et al.* (2016). QUEST—Rilievo macrosismico per i terremoti nell'Italia central, *Aggiornamento dopo le scosse del 26 e 30 ottobre 2016. INGV Technical Report*, %%http://quest.ingv.it/images/rilievimacrosismici/QUEST_report%2018%20gennaio_17ErrCorr.pdf (last accessed July 2017) (in Italian).

Böse, M., T. H. Heaton, and E. Hauksson (2012). Real-time finite fault rupture detector (FinDer) for large earthquakes, *Geophys. J. Int.* **191,** no. 2, 803–812.

Caruso, A., S. Colombelli, L. Elia, M. Picozzi, and A. Zollo (2017). An on-site alert level early warning system for Italy, *J. Geophys. Res.* **122,** doi: 10.1002/2016JB013403.

Chiaraluce, L., R. Di Stefano, E. Tinti, L. Scognamiglio, M. Michele, E. Casarotti, M. Cattaneo, P. De Gori, C. Chiarabba, G. Monachesi, *et al.* (2017). The 2016 central Italy seismic sequence: A first look at the mainshocks, aftershocks, and source models, *Seismol. Res. Lett.* **88,** no. 3, doi: 10.1785/0220160221.

Colombelli, S., R. M. Allen, and A. Zollo (2013). Application of real-time GPS to earthquake early warning in subduction and strike-slip environments, *J. Geophys. Res.* **118,** no. 7, 3448–3461.

Colombelli, S., O. Amoroso, A. Zollo, and H. Kanamori (2012). Test of a threshold-based earthquake early warning using Japanese data, *Bull. Seismol. Soc. Am.* **102,** 1266–1275, doi: 10.1785/0120110149.

Colombelli, S., A. Caruso, A. Zollo, G. Festa, and H. Kanamori (2015). A P wave-based, on-site method for earthquake early warning, *Geophys. Res. Lett.* **42,** 1390–1398, doi: 10.1002/2014GL063002.

Colombelli, S., A. Zollo, G. Festa, and H. Kanamori (2012). Early magnitude and potential damage zone estimates for the great M_w 9 Tohoku-Oki earthquake, *Geophys. Res. Lett.* **39,** no. 22, L22306, doi: 10.1029/2012GL053923.

Colombelli, S., A. Zollo, G. Festa, and M. Picozzi (2014). Evidence for a difference in rupture initiation between small and large earthquakes, *Nature Commun.* **5,** 3958, doi: 10.1038/ncomms4958.

Emergeo W.G.Pucci, S., P. M. De Martini, R. Civico, R. Nappi, T. Ricci, F. Villani, C. A. Brunori, M. Caciagli, V. Sapia, *et al.* (2016). Coseismic effects of the 2016 Amatrice seismic sequence: First geological results, *Ann. Geophys.* **59,** doi: 10.4401/ag-7195.

Faenza, L., and A. Michelini (2010). Regression analysis of MCS intensity and ground motion parameters in Italy and its application in ShakeMap, *Geophys. J. Int.* **180,** 1138–1152, doi: 10.1111/j.1365-246X.2009.04467.x.

Festa, G., A. Zollo, and M. Lancieri (2008). Earthquake magnitude estimation from early radiated energy, *Geophys. Res. Lett.* **35,** L22307, doi: 10.1029/2008GL035576.

Iannaccone, G., A. Zollo, L. Elia, V. Convertito, C. Satriano, C. Martino, G. Festa, M. Lancieri, A. Bobbio, T. A. Stabile, *et al.* (2010). A prototype system for earthquake early-warning and alert management in southern Italy, *Bull. Earthq. Eng.* **8,** 1105–1129, doi: 10.1007/s10518-009-9131-8.

Iervolino, I., G. Baltzopoulos, and E. Chioccarelli (2016). Preliminary engineering analysis of the August 24th 2016, M_L 6.0 central Italy earthquake records, *Ann. Geophys.* **59,** doi: 10.4401/ag-7182.

Kanamori, H. (2005). Real-time seismology and earthquake damage mitigation, *Annu. Rev. Earth Planet. Sci.* **33,** 195–214, doi: 10.1146/annurev.earth.33.092203.122626.

Lancieri, M., and A. Zollo (2008). Bayesian approach to the real-time estimation of magnitude from the early P and S wave displacement peaks, *J. Geophys. Res.* **113,** no. B12302, doi: 10.1029/2007JB005386.

Liu, C., Y. Zheng, Z. Xie, and X. Xiong (2017). Rupture features of the 2016 M_w 6.2 Norcia earthquake and its possible relationship with strong seismic hazards, *Geophys. Res. Lett.* **44,** 1320–1328, doi: 10.1002/2016GL071958.

Livio, F. A., A. M. Michetti, E. Vittori, L. Gregory, L. Wedmore, L. Piccardi, E. Tondi, G. Roberts, and Central Italy Earthquake W. G., A. M. Blumetti, *et al.* (2016). Surface faulting during the August 24, 2016, central Italy earthquake (M_w 6.0): Preliminary results, *Ann. Geophys.* **59,** doi: 10.4401/ag-7197.

Lomax, A., C. Satriano, and M. Vassallo (2012). Automatic picker developments and optimization: FilterPicker—A robust, broadband picker for real-time seismic monitoring and earthquake early warning, *Seismol. Res Lett.* **83,** no. 3, 531–540, doi: 10.1785/gssrl.83.3.531.

Luzi, L., R. Puglia, E. Russo, M. D'Amico, C. Felicetta, F. Pacor, G. Lanzano, U. Çeken, J. Clinton, G. Costa, *et al.* (2016). The engineering

strong-motion database: A platform to access pan-European accelerometric data, *Seismol. Res. Lett.* **87,** no. 4, 987–997, doi: 10.1785/0220150278.

Pacor, F., R. Paolucci, G. Ameri, M. Massa, and R. Puglia (2011). Italian strong motion records in ITACA: Overview and record processing, *Bull. Earthq. Eng.* **9,** no. 6, 1741–1759, doi: 10.1007/s10518-011-9295-x.

Picozzi, M., D. Bindi, P. Brondi, D. Di Giacomo, S. Parolai, and A. Zollo (2017). Rapid determination of *P*-wave-based energy magnitude: Insights on source parameter scaling of the 2016 central Italy earthquake sequence, *Geophys. Res. Lett.* **44,** doi: 10.1002/2017GL073228.

Picozzi, M., A. Zollo, P. Brondi, S. Colombelli, L. Elia, and C. Martino (2015). Exploring the feasibility of a nationwide earthquake early warning system in Italy, *J. Geophys. Res.* **120,** 2446–2465, doi: 10.1002/2014JB011669.

Pucci, S., P. M. De Martini, R. Civico, F. Villani, R. Nappi, T. Ricci, R. Azzaro, C. A. Brunori, M. Caciagli, F. R. Cinti, *et al.* (2017). Coseismic ruptures of the 24 August 2016, M_w 6.0 Amatrice earthquake (central Italy), *Geophys. Res. Lett.* **44,** no. 5, 2138–2147, doi: 10.1002/2016GL071859.

Satriano, C., L. Elia, C. Martino, M. Lancieri, A. Zollo, and G. Iannaccone (2011). PRESTo, the earthquake early warning system for southern Italy: Concepts, capabilities and future perspectives, *Soil Dynam. Earthq. Eng.* **31,** no. 2, 137–153, doi: 10.1016/j.soildyn.2010.06.008.

Satriano, C., A. Lomax, and A. Zollo (2008). Real-time evolutionary earthquake location for seismic early warning, *Bull. Seismol. Soc. Am.* **98,** no. 3, 1482–1494, doi: 10.1785/0120060159.

Satriano, C., Y. M. Wu, A. Zollo, and H. Kanamori (2010). Earthquake early warning: Concepts, methods and physical grounds, *Soil Dynam. Earthq. Eng.* **31,** no. 2, 106–108, doi: 10.1016/j.soildyn.2010.07.007.

Sieberg, A. (1930). Geologie der Erdbeben, *Handbuch der Geophysik* **2,** no. 4, 550–555 (in German).

Tinti, E., L. Scognamiglio, A. Michelini, and M. Cocco (2016). Slip heterogeneity and directivity of the M_L 6.0, 2016, Amatrice earthquake estimated with rapid finite-fault inversion, *Geophys. Res. Lett.* **43,** 10,745–10,752, doi: 10.1002/2016GL071263.

Wu, Y. M., and H. Kanamori (2008). Development of an earthquake early warning system using real-time strong motion signals, *Sensors* **8,** no. 1, 1–9.

Yamada, M., and T. H. Heaton (2008). Real-time estimation of fault rupture extent using envelopes of acceleration, *Bull. Seismol. Soc. Am.* **98,** no. 2, 607–619.

Zollo, A., O. Amoroso, M. Lancieri, Y. M. Wu, and H. Kanamori (2010). A threshold-based earthquake early warning using dense accelerometer networks, *Geophys. J. Int.* **183,** 963–974, doi: 10.1111/j.1365-246X.2010.04765.x.

Zollo, A., S. Colombelli, A. Caruso, L. Elia, P. Brondi, A. Emolo, G. Festa, C. Martino, and M. Picozzi (2017). QuakeUp: An advanced tool for a network-based earthquake early warning system, *Geophys. Res. Abstr.* **19,** Abstract EGU 2017–14033.

Zollo, A., M. Lancieri, and S. B. Nielsen (2006). Earthquake magnitude estimation from peak amplitudes of very early seismic signals on strong motion, *Geophys. Res. Lett.* **33,** L23312, doi: 10.1029/2006GL027795.

Gaetano Festa
Matteo Picozzi
Alessandro Caruso
Simona Colombelli
Luca Elia
Mariano Supino
Aldo Zollo
Dipartimento di Fisica Ettore Pancini
Università di Napoli Federico II
Complesso Univ. Monte S. Angelo, via Cinthia
80126 Naples, Italy
gaetano.festa@unina.it

Marco Cattaneo
Simone Marzorati
Istituto Nazionale di Geofisica e Vulcanologia
Centro Pastorale "Stella Maris"
Via di Colle Ameno, 5
60126 Torette di Ancona, Italy

Lauro Chiaraluce
Istituto Nazionale di Geofisica e Vulcanologia
Via di Vigna Murata, 605
00143 Rome, Italy

Claudio Martino
Istituto Nazionale di Geofisica e Vulcanologia
Via Diocleziano, 328
80125 Naples, Italy

Published Online 22 November 2017

9. Conclusions

I developed a probabilistic method to characterize the source parameters of an earthquake and the anelastic attenuation of the propagation medium.
My work is based on the probabilistic framework developed by Tarantola (2005), and specifically on the notion of conjunction of states of information that has been introduced in Chapter 3. I model the observed far field displacement spectrum assuming a circular rupture model (Brune, 1970) for the source and a Green function characterized by a frequency-independent Q-factor for the propagation. The forward operator is therefore defined on a set of 4 parameters: three parameters for the source – the seismic moment M_0 , the corner frequency f_c and the high-frequency decay exponent γ – and one parameter – the Q-factor – for the propagation. These parameters are strongly correlated among each other. I estimate the joint probability density function (PDF) over the 4-D parameter space to extract the correlation matrix of the parameters; this allows to obtain estimates and uncertainties from the PDF, taking into account the correlations.
Since I model the observations with a non-linear operator, a global exploration of the model space is required in order to find the best solution to describe the data.
The global optimization technique used here, relies on the building of a Markov chain in the parameter space and on the combination of a deterministic minimization with a random exploration of the space (Basin-Hopping method).
In order to validate the developed methodology, I performed synthetic tests on spectra with different signal to noise ratios, defined on different frequency domains (Section 3.7). The method proved its efficacy with all the synthetic spectra. As expected, the resolution of the estimates depends both on the S/N

and the frequency bandwidth available for the inversion; at least 0.1 decades on the left and 0.4 decades on the right of the f_c are required in the frequency domain to obtain reliable estimations for the inversion. Moreover, I showed that the uncertainty on the quality factor estimate depends on the value of Q itself.

The method has been applied to three different datasets :

- The Central Italy 2016/2017 sequence (Chapter 4)
- The LFEs observed in the Nankai region (Japan) during the period 2012-2016 (Chapter 5)
- The micro-seismicity of the Northern Ibaraki region (Japan) during the period 2016-2017 (Chapter 6)

From the study of the seismicity during the Central Italy 2016/2017 sequence, we observed on average that the standard scaling $M_0 \propto \frac{1}{f_c^3}$ holds (Aki, 1967) with an average static stress drop $\Delta\sigma = 2.1 \pm 0.3$ MPa (Section 4.3).

To analyze the stress drop retrieved in this study, we compared our findings with scaling relationships of the two major seismic sequences, that have interested the Central Italy region (Umbria-Marche 1997-1998, L'Aquila 2009) in the last two decades. Different studies for these events show a stress drop fully consistent with our results : Bindi et al. (2004) found an average stress drop of 2 ± 1 MPa for the Umbria-Marche sequence; For L'Aquila sequence, Pacor et al. (2015) retrieved a stress drop variability that spans two orders of magnitude $[0.1 - 25]$ MPa, with an average value of 2.6 MPa.

The Q distribution had a mean value of 230, and a standard deviation of 50; this can be interpreted as a mean value for the S-wave anelastic attenuation

factor of the whole explored region. It is consistent - with a confidence level of 2 σ - with the estimate of Bindi et al. (2004) who found an average S wave anelastic attenuation factor of 318 for the Central Italy region.

In the second application, we estimated the source parameters for 11076 LFEs. We found the typical behavior of the slow earthquakes, observing corner frequencies that are much lower than what expected for ordinary earthquakes sharing the same seismic moment. Furthermore, the retrieved order of magnitude of the stress drop (KPa) is well in the range of what reported in literature (Ide, 2014).

We specifically analyzed the scaling among corner frequency and seismic moment (Section 5.3). When considering all the events and looking at their average behavior, we found a scaling of -3.5 ± 0.5 , which is compatible with to the standard one (-3) within uncertainties. The robustness of this result arises from the probabilistic method used to estimate the source parameters for single station, combined with the quality selection criteria used for the automatic processing of the data (Section 5.2.1). Additionally, we explored a broad magnitude interval (two decades) and the scaling relies on a very large number of events per magnitude bin.

Finally, we studied the micro-seismicity ($M_j = 0.0 - 4.5$) in the Northern Ibaraki area (976 events). A very low anelastic attenuation effect was observed ($Q = 1000 - 2000$), as expected from literature (Takahashi, 2012) and the geological map by GSJ. We proved that, for the explored area (20 x 20 Km^2), the best choice was to fix Q=1500 (Section 6.3.1).

We compared the common assumption of omega-square model ($\gamma = 2$) with a generalized Brune's model (Section 6.3.2). The latter provided a normal distribution for γ estimates with a mean value of to 3.6. We proved that the omega-square assumption led to a worse modeling than the generalized

Brune's model (Section 2.4.1). Furthermore, we found that the $\gamma = 2$ model produces a bias in the modelization of the anelastic attenuation: low Q-values ($Q = 100 - 500$) were estimated for all the events.

We analyzed the scaling law among corner frequency and seismic moment (Section 6.3.3). We found two different behaviors in the explored seismic moment interval $(10^{10.5} - 10^{14.5})$ N m. Self-similarity does not hold in the low region of the seismic moment range $(10^{10.5} - 10^{13.5})$ N m, where we observed a constant corner frequency. On the contrary, standard self-similarity holds in the high seismic moment range $(10^{13.5} - 10^{14.5})$ N m, with an estimated constant static stress drop equal to 5.9 MPa.

Robustness of this result arises from the resolution in the frequency domain, related to the high sampling rate of the data ($f_{SAMP} = 1000$ Hz), yielding a maximum estimable corner frequency beyond 300 Hz. We performed a cluster analysis, from which we were able to observe a directivity effect on the corner frequency estimates (Section 6.3.5). The estimations can be interpreted in terms of bilateral ruptures, propagating along an almost N-S fault plane whose orientation is coherent with the focal mechanisms provided by the NIED.

The developed methodology could allow to better investigate several features of the seismic source, and of the propagation medium.

The joint and marginal PDFs of the source parameters, evaluated station by station as the solution of the inverse problem, and combined as shown in Section 3.6 to obtain the event's solution, could be combined in a different way such that the whole information available from the PDF is used, instead of using only the mean and the variance of the marginal PDF; one possibility

could be represented by the *conflaction* operation defined by Hill and Miller (2011).

Moreover, the single station solutions could be used to analyze the directivity effect on the source parameters estimates. An example is already shown in Section 6.3.5; a systematic analysis of this kind of effect could lead to a modified forward operator that could take into account the direction of propagation of the seismic wave.

Finally, the information about the Q-factor could be used to obtain a robust characterization of the propagation medium; the PDF of the quality factor could be coupled with the information coming from a probabilistic location of the earthquake (e.g. Myers et al., 2007), leading to a new, probabilistic approach for Q tomography.

Bibliography

Abercrombie, R. E. (1995). Earthquake source scaling relationships from− 1 to 5 ML using seismograms recorded at 2.5-km depth. Journal of Geophysical Research: Solid Earth, 100(B12), 24015-24036.

Aki, K. (1967). Scaling law of seismic spectrum. Journal of Geophysical Research, 72(4), 1217-1231.

Aki, K., & Richards, P. G. (1980). Quantative seismology: Theory and methods. New York, 801.

Anderson, J. G., & Hough, S. E. (1984). A model for the shape of the Fourier amplitude spectrum of acceleration at high frequencies. Bulletin of the Seismological Society of America, 74(5), 1969-1993.

Balas, E., Ceria, S., & Cornuéjols, G. (1993). A lift-and-project cutting plane algorithm for mixed 0–1 programs. Mathematical programming, 58(1-3), 295-324.

Bindi, D., Castro, R. R., Franceschina, G., Luzi, L., & Pacor, F. (2004). The 1997–1998 Umbria-Marche sequence (central Italy): Source, path, and site effects estimated from strong motion data recorded in the epicentral area. Journal of Geophysical Research: Solid Earth, 109(B4).

Boore, D. M., & Boatwright, J. (1984). Average body-wave radiation coefficients. Bulletin of the Seismological Society of America, 74(5), 1615-1621.

Bostock, M. G., Thomas, A. M., Savard, G., Chuang, L., & Rubin, A. M. (2015). Magnitudes and moment-duration scaling of low-frequency earthquakes beneath southern Vancouver Island. Journal of Geophysical Research: Solid Earth, 120(9), 6329-6350.

Brown, J. R., Beroza, G. C., & Shelly, D. R. (2008). An autocorrelation method to detect low frequency earthquakes within tremor. Geophysical Research Letters, 35(16).

Brune, J. N. (1970). Tectonic stress and the spectra of seismic shear waves from earthquakes. Journal of geophysical research, 75(26), 4997-5009.

Cauchy, A. (1847). Méthode générale pour la résolution des systemes d'équations simultanées. Comp. Rend. Sci. Paris, 25(1847), 536-538.

Chiarabba, C., Piccinini, D., & De Gori, P. (2009). Velocity and attenuation tomography of the Umbria Marche 1997 fault system: Evidence of a fluid-governed seismic sequence. Tectonophysics, 476(1-2), 73-84.

Chiaraluce, L., Di Stefano, R., Tinti, E., Scognamiglio, L., Michele, M., Casarotti, E., ... & Lombardi, A. (2017). The 2016 central Italy seismic sequence: A first look at the mainshocks, aftershocks, and source models. Seismological Research Letters, 88(3), 757-771.

Cocco, M., Tinti, E., & Cirella, A. (2016). On the scale dependence of earthquake stress drop. Journal of Seismology, 20(4), 1151-1170.

Cooley, J. W., & Tukey, J. W. (1965). An algorithm for the machine calculation of complex Fourier series. Mathematics of computation, 19(90), 297-301.

Cotton, F., Archuleta, R., & Causse, M. (2013). What is sigma of the stress drop?. Seismological Research Letters, 84(1), 42-48.

Del Gaudio, S., Causse, M., & Festa, G. (2015). Broad-band strong motion simulations coupling k-square kinematic source models with empirical Green's functions: the 2009 L'Aquila earthquake. Geophysical Journal International, 203(1), 720-736.

Dragert, H., Wang, K., & James, T. S. (2001). A silent slip event on the deeper Cascadia subduction interface. Science, 292(5521), 1525-1528.

Fletcher, J., Boatwright, J., Haar, L., Hanks, T., & McGarr, A. (1984). Source parameters for aftershocks of the Oroville, California, earthquake. Bulletin of the Seismological Society of America, 74(4), 1101-1123.

Fletcher, R., & Xu, C. (1987). Hybrid methods for nonlinear least squares. IMA Journal of Numerical Analysis, 7(3), 371-389.

Frank, W. B., Shapiro, N. M., Husker, A. L., Kostoglodov, V., Romanenko, A., & Campillo, M. (2014). Using systematically characterized low-frequency earthquakes as a fault probe in Guerrero, Mexico. Journal of Geophysical Research: Solid Earth, 119(10), 7686-7700.

Gauss, C. F. (1809). Theoria motus corporum coelestium in sectionibus conicis solem ambientium (Vol. 7). Perthes et Besser.

Goldberg, D. E., & Holland, J. H. (1988). Genetic algorithms and machine learning. Machine learning, 3(2), 95-99.

Gomory, R. (1960). An algorithm for the mixed integer problem (No. RAND-P-1885). RAND CORP SANTA MONICA CA.

Gomory, R. (1963). An algorithm for integer solutions to linear programs. Recent advances in mathematical programming, 64, 260-302.

Hanks, T. C., & Kanamori, H. (1979). A moment magnitude scale. Journal of Geophysical Research: Solid Earth, 84(B5), 2348-2350.

Haskell, N. A. (1964). Total energy and energy spectral density of elastic wave radiation from propagating faults. Bulletin of the Seismological Society of America, 54(6A), 1811-1841.

Hill, T. P., & Miller, J. (2011). How to combine independent data sets for the same quantity. Chaos: An Interdisciplinary Journal of Nonlinear Science, 21(3), 033102.

Hunter., J. D. (2007) Matplotlib: A 2D Graphics Environment. Computing in Science & Engineering, 9, 90-95.

Ide, S., & Beroza, G. C. (2001). Does apparent stress vary with earthquake size?. Geophysical Research Letters, 28(17), 3349-3352.

Ide, S., Beroza, G. C., Prejean, S. G., & Ellsworth, W. L. (2003). Apparent break in earthquake scaling due to path and site effects on deep borehole recordings. Journal of Geophysical Research: Solid Earth, 108(B5).

Ide, S., Beroza, G. C., Shelly, D. R., & Uchide, T. (2007). A scaling law for slow earthquakes. Nature, 447(7140), 76.

Ide, S. (2014). Modeling fast and slow earthquakes at various scales. Proceedings of the Japan Academy, Series B, 90(8), 259-277.

Imanishi, K., & Uchide, T. (2017). Non-self-similar source property for microforeshocks of the 2014 Mw 6.2 Northern Nagano, central Japan, earthquake. Geophysical Research Letters, 44(11), 5401-5410.

ISIDe working group (2016) version 1.0. Istituto Nazionale di Geofisica e Vulcanologia, Observatories & Research Facilities for European Seismology. DOI: 10.13127/ISIDe.

Ito, Y., Obara, K., Shiomi, K., Sekine, S., & Hirose, H. (2007). Slow earthquakes coincident with episodic tremors and slow slip events. Science, 315(5811), 503-506.

Kahn, H., & Harris, T. E. (1951). Estimation of particle transmission by random sampling. National Bureau of Standards applied mathematics series, 12, 27-30.

Kanamori, H., & Cipar, J. J. (1974). Focal process of the great Chilean earthquake May 22, 1960. Physics of the Earth and Planetary Interiors, 9(2), 128-136.

Kolmogorov, A. N. (1933). Foundations of probability.

Keilis-Borok, V. I. (1959). On the estimation of the displacement in an earthquake source and of source dimensions. Ann. Geofis., 12, 205-214.

Kirkpatrick, S., Gelatt, C. D., & Vecchi, M. P. (1983). Optimization by simulated annealing. science, 220(4598), 671-680.

Knopoff, L. (1964). Q. Reviews of Geophysics, 2(4), 625–660.

Kubo, A., Fukuyama, E., Kawai, H. & Nonomura, K. 2002. NIED seismic moment tensor catalogue for regional earthquakes around Japan: quality test and application, Tectonophysics, 356(1-3), 23–48.

Land, A. H., & Doig, A. G. (1960). An automatic method of solving discrete programming problems. Econometrica: Journal of the Econometric Society, 497-520.

Lebedev, A. V., Bredikhin, V. V., Soustova, I. A., Sutin, A. M., & Kusunose, K. (2003). Resonant acoustic spectroscopy of microfracture in a Westerly granite sample. Journal of Geophysical Research: Solid Earth, 108(B10).

Levenberg, K. (1944). A method for the solution of certain non-linear problems in least squares. Quarterly of applied mathematics, 2(2), 164-168.

Linde, A. T., Gladwin, M. T., Johnston, M. J., Gwyther, R. L., & Bilham, R. G. (1996). A slow earthquake sequence on the San Andreas fault. Nature, 383(6595), 65.

Liu, C., Zheng, Y., Xie, Z., & Xiong, X. (2017). Rupture features of the 2016 Mw 6.2 Norcia earthquake and its possible relationship with strong seismic hazards. Geophys. Res. Lett., 44(3), 1320-1328.

Lomax, A., Virieux, J., Volant, P., & Berge-Thierry, C. (2000). Probabilistic earthquake location in 3D and layered models. In Advances in seismic event location (pp. 101-134). Springer, Dordrecht.

Luzi L, Puglia R, Russo E & ORFEUS WG5 (2016). Engineering Strong Motion Database, version 1.0. Istituto Nazionale di Geofisica e Vulcanologia, Observatories & Research Facilities for European Seismology. DOI: 10.13127/ESM

Madariaga, R. (1976). Dynamics of an expanding circular fault. Bulletin of the Seismological Society of America, 66(3), 639-666.

Marquardt, D. W. (1963). An algorithm for least-squares estimation of nonlinear parameters. Journal of the society for Industrial and Applied Mathematics, 11(2), 431-441.

Megies, T., Beyreuther, M., Barsch, R., Krischer, L., & Wassermann, J. (2011). ObsPy–What can it do for data centers and observatories?. Annals of Geophysics, 54(1), 47-58.

Minson, S. E., Simons, M., & Beck, J. L. (2013). Bayesian inversion for finite fault earthquake source models I—Theory and algorithm. Geophysical Journal International, 194(3), 1701-1726.

Myers, S. C., Johannesson, G., & Hanley, W. (2007). A Bayesian hierarchical method for multiple-event seismic location. Geophysical Journal International, 171(3), 1049-1063.

Nielsen, S., Spagnuolo, E., Violay, M., Smith, S., Di Toro, G., & Bistacchi, A. (2016). G: Fracture energy, friction and dissipation in earthquakes. Journal of seismology, 20(4), 1187-1205.

Nishide, N., Hashimoto, T., Funasaki, J., Nakazawa, H., Oka, M., Ueno, H., ... & Takashima, T. (2000). Nationwide activity of low-frequency earthquakes in the lower crust in Japan. In Abstr. Jpn. Earth and Planet. Sci. Joint Meeting, sk-p002.

Nocedal, J., & Wright, S. J. (2006). Conjugate gradient methods. Numerical optimization, 101-134.

Obara, K. (2002). Nonvolcanic deep tremor associated with subduction in southwest Japan. Science, 296(5573), 1679-1681.

Obara, K., Kasahara, K., Hori, S., & Okada, Y. (2005). A densely distributed high-sensitivity seismograph network in japan: Hi-net by national research institute for earth science and disasterprevention. Review of scientific instruments, 76(2), 021301.

Oliphant, T. E. (2007). Python for Scientific Computing. Computing in Science & Engineering, 9, 10-20.

Oye, V., Bungum, H., & Roth, M. (2005). Source parameters and scaling relations for mining-related seismicity within the Pyhasalmi ore mine, Finland. Bulletin of the Seismological Society of America, 95(3), 1011-1026.

Pacor, F., Spallarossa, D., Oth, A., Luzi, L., Puglia, R., Cantore, L., ... & Bindi, D. (2015). Spectral models for ground motion prediction in the L'Aquila region (central Italy): evidence for stress-drop dependence on magnitude and depth. Geophysical Journal International, 204(2), 697-718.

Piatanesi, A., Cirella, A., Spudich, P., & Cocco, M. (2007). A global search inversion for earthquake kinematic rupture history: Application to the 2000 western Tottori, Japan earthquake. Journal of Geophysical Research: Solid Earth, 112(B7).

Poiata, N., Satriano, C., Vilotte, J. P., Bernard, P., & Obara, K. (2016). Multiband array detection and location of seismic sources recorded by dense seismic networks. Geophysical Journal International, 205(3), 1548-1573.

Prieto, G. A., Thomson, D. J., Vernon, F. L., Shearer, P. M., & Parker, R. L. (2007). Confidence intervals for earthquake source parameters. Geophysical Journal International, 168(3), 1227-1234.

Quenouille, M. H. (1949, July). Approximate tests of correlation in time-series 3. In Mathematical Proceedings of the Cambridge Philosophical Society (Vol. 45, No. 3, pp. 483-484). Cambridge University Press.

Sato, T., & Hirasawa, T. (1973). Body wave spectra from propagating shear cracks. Journal of Physics of the Earth, 21(4), 415-431.

Scholz, C. H. (1994). A reappraisal of large earthquake scaling. Bulletin of the Seismological Society of America, 84(1), 215-218.

Shaw, B. E. (2009). Constant stress drop from small to great earthquakes in magnitude-area scaling. Bulletin of the Seismological Society of America, 99(2A), 871-875.

Song, S. G., & Somerville, P. (2010). Physics-based earthquake source characterization and modeling with geostatistics. Bulletin of the Seismological Society of America, 100(2), 482-496.

Takahashi, T. (2012). Three-dimensional attenuation structure of intrinsic absorption and wide-angle scattering of S waves in northeastern Japan. Geophysical Journal International, 189(3), 1667-1680.

Taylor, J. (1997). Introduction to error analysis, the study of uncertainties in physical measurements.

Tarantola, A. (2005). Inverse problem theory and methods for model parameter estimation (Vol. 89). Siam.

Tinti, E., Scognamiglio, L., Michelini, A., & Cocco, M. (2016). Slip heterogeneity and directivity of the ML 6.0, 2016, Amatrice earthquake estimated with rapid finite-fault inversion. Geophysical Research Letters, 43(20).

Trifunac, M. D., & Brady, A. G. (1975). A study on the duration of strong earthquake ground motion. Bulletin of the Seismological Society of America, 65(3), 581-626.

Tukey, J. (1958). Bias and confidence in not quite large samples. Ann. Math. Statist., 29, 614.

Turing, A. M. (1950). Computing Machinery and Intelligence. Mind, 59(236), 433-460.

Uchide, T., & Imanishi, K. (2018). Underestimation of microearthquake size by the magnitude scale of the Japan Meteorological Agency: Influence on earthquake statistics. Journal of Geophysical Research: Solid Earth, 123(1), 606-620.

Van Rossum G., (1995). Python tutorial, Technical Report CS-R9526, Centrum voor Wiskunde en Informatica (CWI), Amsterdam.

Wales, D., & Doye, J. P. (1997). Global optimization by basin-hopping and the lowest energy structures of Lennard-Jones clusters containing up to 110 atoms. The Journal of Physical Chemistry A, 101(28), 5111-5116.

Wales, D. (2003). Energy landscapes: Applications to clusters, biomolecules and glasses. Cambridge University Press.

Zener, C. (1948). Elasticity and anelasticity of metals. University of Chicago press.

Zollo, A., Orefice, A., & Convertito, V. (2014). Source parameter scaling and radiation efficiency of microearthquakes along the Irpinia fault zone in southern Apennines, Italy. Journal of Geophysical Research: Solid Earth, 119(4), 3256-3275.

Appendix A

In the time domain, the displacement u is the sum of the signal $s(t)$ and the noise $n(t)$:

$$u(t) = s(t) + n(t) \tag{A1}$$

Here we prove that, for small $\frac{|\tilde{n}|}{|\tilde{s}|}$, the displacement amplitude spectrum can be written as :

$$\log(\tilde{u}) \approx \log(\tilde{s}) + \frac{\tilde{n}}{\tilde{s}}\cos(\varphi_S - \varphi_N) \tag{A2}$$

where $\tilde{s}$ and $\tilde{n}$ are the amplitude spectra and φ_S and φ_N the phase spectra of the signal and the noise, respectively; they are all functions of the frequency.

Applying the Fourier transform to the equation (A1), we have

$$\tilde{u}(f) = \tilde{s}(f) + \tilde{n}(f) \tag{A3}$$

It follows that :

$$\begin{aligned} |\tilde{u}| &= \sqrt{(\tilde{s}+\tilde{n})(\overline{\tilde{s}}+\overline{\tilde{n}})} = \sqrt{|\tilde{s}|^2 + 2\,\mathrm{Re}(\tilde{s}\overline{\tilde{n}}) + |\tilde{n}|^2} = |\tilde{s}|\sqrt{1 + 2\frac{\mathrm{Re}(\tilde{s}\overline{\tilde{n}})}{|\tilde{s}|^2} + \frac{|\tilde{n}|^2}{|\tilde{s}|^2}} \\ &\approx |\tilde{s}|\sqrt{1 + 2\frac{\mathrm{Re}(\tilde{s}\overline{\tilde{n}})}{|\tilde{s}|^2}} \approx |\tilde{s}|\left(1 + \frac{\mathrm{Re}(\tilde{s}\overline{\tilde{n}})}{|\tilde{s}|^2}\right) = |\tilde{s}| + \frac{\mathrm{Re}(\tilde{s}\overline{\tilde{n}})}{|\tilde{s}|} \\ &= |\tilde{s}| + |\tilde{n}|\cos(\varphi_S - \varphi_N) \end{aligned} \tag{A4}$$

where we neglected the term $\frac{|\tilde{n}|^2}{|\tilde{s}|^2}$, and we approximate $\sqrt{1+x} \approx 1 + \frac{x}{2}$ for small x. The logarithm of (A4) gives the equation (A2) :

$$\log|\tilde{u}| = \log|\tilde{s}| + \log\left(1 + \frac{|\tilde{n}|}{|\tilde{s}|}\cos(\varphi_S - \varphi_N)\right) \approx \log|\tilde{s}| + \frac{|\tilde{n}|}{|\tilde{s}|}\cos(\varphi_S - \varphi_N) \tag{A5}$$

where $\log(1+x) \approx x$ for small x □.

Acknowledgements

Gaetano Festa is my *magister* since several years. He decided to share with me his wide and extensive knowledge; this is a huge privilege, for me. During these years, he always led me along the direction of a rigorous, courageous and intriguing research.

Aldo Zollo welcomed me into his research group; he trusted me, entrusting me with responsibilities and strongly supporting me during my Ph.D..

Jean-Pierre Vilotte gave me the opportunity to study with him at the IPGP, in Paris. He let me and my research project to grow enormously.

Takahiko Uchide allowed me to work at the AIST, in Tsukuba. Thanks to him, I discovered an amazing new culture, and an incredibly rigorous and broad knowledge of the Physics of the Earth.

Finally, during the time I spent abroad I had the chance to deeply discuss about my research with Nikolai Shapiro and Satoshi Ide. They strongly encouraged me to publish my findings; this was a great honor for me.

To all these scientists goes my sincere gratitude.

Ringraziamenti

Il percorso è stato molto lungo. Con questa tesi termina, almeno formalmente, il mio essere studente.
Negli anni, ho incontrato persone e luoghi che desidero ringraziare.

Maria Luisa. Tu sei di gran lunga la persona più bella che potessi incontrare.

Mia madre, Anna. Ti voglio bene almeno quanto tu ne vuoi a me.
Mio padre, Antonio. Tra le tante cose, forse senza quella storia del "trovato" questa passione non sarebbe mai nata.
Nunzia. Nonostante le doppie domande, e le doppie risposte mancate; sarai per sempre la mia ancora.
Pipo. Siamo uno l'opposto dell'altro, e forse consiste proprio in questo la nostra immensa forza.
Guglielmo. Per quella semifinale di Atene 2004, i giornali di Diego, ed il Napoli insieme.
Zia Teresa. Per avermi "visto nascere", per la pizza piena e le tagliatelle. Per l'amore.
Francesco. Per Natale, Procida, i bagni al tramonto, il Giappone mancato ed il Giappone che c'è stato.
Zio Ciro. Per avermi mostrato cosa significa passione, generosità, Procida e bontà.

Claudia. Forse, senza di te non avrei mai conosciuto la Geofisica; sicuramente, non avrei conosciuto per la prima volta la felicità.
Аня. С тобой, Вильнюс-Берлин это был возврат.
Elodie. Pour le beurre salé, Albi et la robe rouge.

I compagni dell'ex-OPG. Per avermi fatto vedere il disinteresse di cui tanto avevo sentito parlare.
La ex II D. Dopo tanti anni, siamo stupendi.
Giovanna e Silvia. Perché la scienza è iniziata con voi.
Jhonatan. Per i passaggi in elicottero che verranno e per quelli che ci sono già stati.

Cristiana. Per essere diventata l'amica che non avrei mai creduto, e mai sperato. Per quella sera.

Gaetano, il mio maestro. Perché Best Supervisor Ever non è solo una foto scattata su una montagna irpina.
Lorenzo, perché il primo tesista non si scorda mai.
Il mio collega Emmanuele. Il miglior Fisico teorico del dipartimento, che mi chiama collega.
Marco, Ciro, Maria Cristina, Giuseppe, Valeria, Mauro, Giulia, Alessia, Pedro. Se sono qui è perché abbiamo combattuto insieme dal primo anno.
Enzo Esposito. Perché il tuo corso è un'incredibile leggenda.
Paolo. Per aver rimandato per la prima volta la tua laurea solo perché ero in Giappone.
La vecchia pigreca, la nuova pigreca. Per il caffè, il tripong, il ranking e la follia.
Il mio laboratorio, il RISSC-Lab. Per avermi accolto, ascoltato e sopportato.
Maria, Petuzzo, Faz, Azam, Silvia, Mauro, Peppe, Casimiro e Alberto. Per aver portato Napoli a Torino, ed il Nord a Napoli.
Marinà e Flò. Per la Bretagna, i caffè napoletani, i biscotti e le pause.
Claudio. Per i consigli e la gentilezza.
Bart. A close friend in a very far, and new, world.

Ringraziamenti

I miei compagni di biblioteca a Napoli, a Torino e poi ancora a Napoli. Tra tutti Giovanni, nonostante i Distinti.

Josephìne, Pedo, il Koreano, Vitellone, il Macellaio, il fencing team. Non sarà Napoli 2019, non sarà Tokyo 2020, ma il 2024 senza alcun dubbio sarà nostro.
La scherma, anche detta Alessandra. Per avermi dato molto più di quanto io potrò mai darti.

Vilnius, Минск, Москва. Per le vostre biblioteche.
Ленинград. Per avermi mostrato la bellezza.
Maurizio Sarri. Per avermi mostrato la bellezza.

New Orleans. Per avermi lanciato con un'incredibile rincorsa.
Kyoto. Per il Fushimi Inari.

Quel caffè che non ho preso, virando verso il piano inclinato.
Non ti ho mai cercata; eppure, all'improvviso, ti ho incontrata.